TOWARD THE REALIZATION OF MEMBRANELESS FLOW BATTERIES AND SOLID OXIDE ELECTROLYZERS AS PRACTICAL FORMS OF GRID-SCALE ENERGY STORAGE TECHNOLOGIES

By

Korey Cook

A DISSERTATION

Submitted to
Michigan State University
in partial fulfillment of the requirements
for the degree of

Mechanical Engineering – Doctor of Philosophy

2021

ABSTRACT

TOWARD THE REALIZATION OF MEMBRANELESS FLOW BATTERIES AND SOLID OXIDE ELECTROLYZERS AS PRACTICAL FORMS OF GRID-SCALE ENERGY STORAGE TECHNOLOGIES

By

Korey Cook

Grid-scale energy storage is becoming a crucial component of the energy infrastructure as energy generation is rapidly evolving and involves intermittent renewable systems. A variety of thermal, mechanical, electrical, chemical, and electrochemical storage technologies are being considered. In this thesis, two important electrochemical systems are studied: redox flow batteries (RFBs) and solid oxide electrolyzer cells (SOECs). The new RFB involves novel linked chemicals that could enable a symmetric flow battery that utilizes a low-cost microporous separator rather than an expensive ion-selective membrane. Using new linked compounds addresses several issues with RFBs, namely capacity fade caused by crossover, as well as maintenance issues (rebalancing), and their high cost. Additive manufacturing was used to initially manufacture a flow cell which could demonstrate a linked compound, 4-phenothiazine 5,5-dioxide covalently linked via a propyl chain to 4-acetylpyridinum. The intention was to show that it could be cycled in a flow cell using inexpensive parts and materials. Viscosity, solubility, and other preliminary measurements were taken to aid in the selection of organic solvents and charge balancing electrolyte. Static, constant current, cyclic charge-discharge experiments were also performed in a commercial flow cell test fixture for the same compound. Electrochemical performance and stability were studied using solutions with identical concentrations of active species in two different organic solvents. The results showed that the specific linked system being studied could operate in a static cell without a membrane; however, it suffered from chemical decomposition. A variety of other compounds are possible which means the chemical stability can be improved. Experiments with flow were conducted to evaluate the impact that charging voltage, flow rate, and electrolyte recirculation have on electrochemical performance. A difference in the rate of the charging kinetics was observed. To improve coulombic efficiency, the

charging flow rate was reduced while maintaining a faster discharging flow rate. An ideal charging voltage was observed. Electrochemical impedance spectroscopy was used to quantify and compare the internal losses associated with the cell separator and ion-selective membrane. As expected, the microporous separator displays significantly lower resistivity.

A second important electrochemical system, solid oxide electrolyzers, was studied in this thesis. High temperature SOECs are an appealing hydrogen gas (H_2) producing technology because they do not require an expensive catalyst; however, they suffer from premature electrode-electrolyte delamination. A multiphase, axisymmetric, microscale model was developed to identify the primary delamination mechanism. It was hypothesized that competition between two-phase and three-phase boundaries strains the lattice structure, leading to delamination. At high operating voltages, the reactions at the three-phase boundary dominated the two-phase reactions. This was thought to be driving delamination. The model was validated using experimental data that measured the overpotential and current density. The material composition of the electrode was altered by adding an additional thin, highly electronically conductive layer to enhance transport. This was studied both computationally and experimentally. The results from both experiments and computations indicated that the lattice oxygen at the surface was more evenly distributed. Using a bilayer electrode enhanced transport through the two-phase boundaries, reducing lattice structure expansion at the three-phase boundaries which could prevent delamination.

ACKNOWLEDGEMENTS

I would first like to thank my parents Rob and Debi, sisters Kacey and Kelsey, my wife Haley, and our dog Ellie for their unwavering support. I would not be where I am today without each of them and am so thankful that I have them. These have been some of the most challenging, yet fulfilling, years of my life and I'm glad they were by my side. I would also like to thank my primary advisors Dr. Thomas Guarr and Professor André Bénard who supported me while I attended graduate school at Michigan State University (MSU). I would also like to thank my committee members including Dr. Scott Calabrese Barton, Dr. Farhad Jaberi, and Dr. James Klausner. I received support from and was welcomed into the lab space at the MSU Engineering Research Complex by Dr. Harold Schock and Tom Stuecken M.Sc.Eng. I also appreciate the support I received from two undergraduate students, Riley Lawson and Ethan Lau. Additional support from Ethan Lau, Riley Lawson, Shane Mann M.Sc.Chem., Elizabeth Hoekstra, Bridget O'Connell, Kassia Symstad, Michael Giurini, Laura Ives M.Sc.Eng., and Jessica Scott M. Sc. Chem is gratefully acknowledged. Financial support for portions of work from $MSUBI$, from a Departoment of Energy (DOE) SBIR grant to Jolt Energy Storage Technologies, LLC, the MSU Mechanical Engineering Department, and the Graduate Office Fellowship was crucial to my success.

As funding sources changed towards the end of my time at MSU, I began working remotely as a post-doctoral researcher investigating transport phenomena within a Solid Oxide Electrolyzer Cell. This project was carried out under the guidance of Xinfang Jin at the University of Massachusetts-Lowell, in partnership with Dr. Kevin Huang of the University of South Carolina, also with Dr. Zhiwen Ma and Dr. Jacob Wrubel of the $DOE's$ National Renewable Energy Laboratory ($NREL$). I am excited that I have the opportunity to continue pursuing my passions while transitioning to work full time at $NREL$ with researchers including Dr. Zhwien Ma, Dr. Xingchao Wang, and Patrick Davenport M.Sc.Eng.. I would not be who I am, nor would I be able to start my career at one of the most innovative energy laboratories in the world without the support and guidance received from all the institutions and individuals mentioned above.

TABLE OF CONTENTS

LIST OF TABLES vii

LIST OF FIGURES ix

KEY TO SYMBOLS xiv

CHAPTER 1 GRID-SCALE ENERGY STORAGE TECHNOLOGIES, RESEARCH OBJECTIVES, AND METHODS 1
1.1 Grid-Scale Energy Storage Technologies of Interest 4
1.1.1 Redox Flow Batteries 4
1.1.2 Hydrogen Generated using a Solid Oxide Electrolyzer Cell 5
1.2 Research Objectives, Studies Performed, and Structure of Dissertation 6

CHAPTER 2 DEVELOPMENT OF A MEMBRANELESS ORGANIC REDOX FLOW BATTERY 10
2.1 Introduction 10
2.2 Membraneless Redox Flow Battery Literature Review 11
2.3 Covalently Linked Redox Couple 13
2.4 Techno-Economic Analysis 16
2.5 Computational Fluid Dynamics Analysis 18
2.6 Rapid Prototyping of Experimental Flow Cells 21
2.7 Electrochemical Experimental Results 26
2.8 Conclusion 28

CHAPTER 3 DEMONSTRATION OF A LINKED ANOLYTE-CATHOLYTE SYSTEM FOR NONAQUEOUS ORGANIC REDOX FLOW BATTERIES . . . 30
3.1 Introduction 30
3.2 Experimental 33
3.3 Results and Discussion 36
3.3.1 Static Cycling and Cyclic Voltammetry 36
3.3.2 Flow Cycling and Operating Parameter Analysis 38
3.4 Conclusions 42

CHAPTER 4 IDENTIFYING AND QUANTIFYING LOSSES IN A MEMBRANELESS, NONAQUEOUS, ORGANIC REDOX FLOW BATTERY USING ELECTROCHEMICAL IMPEDANCE SPECTROSCOPY 43
4.1 Introduction 43
4.2 Redox Flow Battery Components' Impact on Internal Losses 45
4.2.1 Chemistry Considerations 47
4.2.2 System Design and Manufacturing Considerations 48
4.2.2.1 Flow Field Geometry 49
4.2.2.2 Reaction Chamber 51

4.2.2.3 Porous Electrode . . . 52
4.2.2.4 Current Collector . . . 53
4.2.2.5 Membrane . . . 54
4.3 Experimental . . . 55
4.3.1 Results and Discussion . . . 56
4.3.2 EIS Equivalent Circuit . . . 57
4.4 Conclusions . . . 59

CHAPTER 5 INTERRELATIONSHIP BETWEEN EXTENDED TRANSPORT PATHWAYS OF MIXED CONDUCTING ELECTRODES AND DELAMINATION IN SOLID OXIDE ELECTROLYZER CELLS . . . 61
5.1 Introduction . . . 61
5.2 Microscale Model Theory . . . 63
5.3 Experimental Validation and Model Parameters . . . 68
5.4 Results . . . 71
5.4.1 Transport Pathway Competition . . . 71
5.4.2 Surface Oxygen Site Coverage . . . 73
5.4.3 Lattice Oxygen Stoichiometry Profile . . . 75
5.4.4 Overall Electrochemical Performance . . . 76
5.5 Discussion . . . 77
5.6 Conclusions . . . 80

CHAPTER 6 CONCLUSIONS . . . 81
6.1 Conclusions Drawn from Flow Battery and Electrolyzer Studies . . . 81
6.1.1 Redox Flow Battery . . . 81
6.1.2 Solid Oxide Electrolyzer Cell . . . 82
6.2 Recommendations for Future Work . . . 82
6.2.1 Novel Linked Redox Couple Performance Improvement and Development of a Stack Model for Commercial Scale System . . . 82
6.2.2 Incorporation of Thermomechanical Stress Analysis and the Use of Advanced Imaging Techniques to Generate Complex 3D Electrode Geometries 84

APPENDIX . . . 86

BIBLIOGRAPHY . . . 91

LIST OF TABLES

Table 1.1: 2020 levelized cost of energy for various forms of renewable and nonrenewable generation technologies. 2

Table 2.1: Common RFB chemistry proposed in literature compared with the novel linked redox couple. 10

Table 2.2: Estimated parameters included in the techno-economic analysis, performed to compare the impact that incorporation of an ion-selective membrane or a microporous separator has on the capital cost of an RFB. 17

Table 2.3: Mesh refinement results comparing flow fields. 21

Table 2.4: Flow distribution efficiency of two reaction chamber designs that incorporate Y-splits to evenly distribute solution into the reaction chamber. 24

Table 3.1: Symmetric flow cell cycling results comparing average current, capacity while charging, and coulombic efficiency while varying charging potential and flow rate. 41

Table 4.1: Components associated with ohmic resistance within an RFB. 46

Table 4.2: Components associated with charge-transfer resistance within an RFB. 46

Table 4.3: Components associated with mass-transfer resistance within an RFB. 46

Table 5.1: Charge carriers, dependent variables, and governing equations describing the transport phenomena within each layer shown in Figure 5.1. 64

Table 5.2: Boundary conditions used to describe 2PBs and 3PBs within an SOEC consisting of a solid-state,multilayer electrolyte-electrode structure shown in Figure 5.1. 65

Table 5.3: Elementary reactions shown in Figure 5.3. 67

Table 5.4: Source term expressions derived to describe oxygen desorption and oxygen evolution reactions in the SOEC's multilayer electrodes shown in Figure 5.3. . . 67

Table 5.5: Reaction kinetic parameters included while developing the model from literature, some were adjusted using experimental data (denoted by *). 69

Table A.1: Solubility of various supporting electrolyte and active species in Acetonitrile (ACN) and Propylene Carbonate (PC). Note that immeasurable values are denoted by –. 90

Table A.2: Kinematic viscosity of PC/$TEABF_4$ and ACN/$TEABF_4$ electrolytes at various temperatures (entries in centistokes, cSt). Note that immeasurable values are denoted by –. 90

LIST OF FIGURES

Figure 1.1: A diagram of an RFB showing the storage reservoirs, membrane, active material in charged and neutral oxidation states (C, C^+, A, A^-), charge balancing electrolyte (+, −), current collectors, porous electrodes, an exploded view of a three-dimensional model (upper right), and the oxidation and reduction reactions. This RFB is depicted as discharging when flowing from left to right an charging when flowing right to left. 4

Figure 1.2: Diagram showing each layer of the SOEC and the species involved which includes the primary charge carrier oxygen ions (O^X), oxygen vacancies ($V^{\cdot\cdot}$), electrons (e'), and electron holes ($h^{\cdot}$). e' and $h^{\cdot}$ move opposite of one another and are only present in the LSCF and GDC layers while O^X and $V^{\cdot\cdot}$ are present in each layer. Several types of two and three-phase boundaries exist including continuous charge transport, electrode/gas, and multi electrode/gas interface. 5

Figure 2.1: (a)Asymmetric redox flow batteries use an ion-selective membrane to maintain separation between the anolyte A and catholyte C species.The arrows are shown to represent the membrane rejecting active species from crossing over.(b) Symmetric redox flow battery using a stable radical as both the anolyte A and catholyte C. The arrows represent the non-selectivity of a microporous separator. (c) Symmetric redox flow battery using a mixed solution on both sides of the cell containing both the A and C. (d) Symmetric redox flow battery using a covalently linked anolyte-catholyte $A - L - C$ bipolar molecule. 12

Figure 2.2: Compound 1 (left) is an example of a model $C - L - A$, compound 2 (right) is a prepared $C - L - A - L - C$ system using an extended bis-pyridinium acceptor covalently linked to phenothiazine 5,5-dioxide donor groups. 15

Figure 2.3: Cyclic voltammograms of compounds 1, in red, and 2, in blue. Both voltammograms were produced using a 0.2 M $TEABF_4$ solution of propylene carbonate, a Pt disc working electrode, a Pt/Ti wire anode, and a Ag wire as a pseudo-reference electrode at a scan rate of 100 and 50 mV/s for 1 and 2 respectively. 15

Figure 2.4: CAD model of flow cell Geometry 1(a), the geometry of the fluid within the cell(b), and the resulting pressure contour(c). 19

Figure 2.5: (a)CAD model of the flow within Geometry 2. The same design approach was used with the exception that it is skinnier and 40% smaller than Geometry 1 shown in Figure 2.4. (b) The geometry of the fluid within the cell. (c) Pressure contours and streamlines for Geometry 2 showing a slightly larger pressure drop but there still seems to be uniform flow. 20

Figure 2.6: (a)Conventional (b)parallel (c)serpentine and (d)interdigitated flow channel designs are shown. The fluid moves from the top inlet to the bottom outlet. . . . 22

Figure 2.7: A 3D model was developed to successfully fabricate and test an interdigitated flow field: an exploded view showing an RFB cell and its corresponding components(a), an interdigitated flow field(b), and the operational prototype cell(c). 25

Figure 2.8: 3D printed cell with its associated components(a) and a fully assembled cell(b). 26

Figure 2.9: Initial test station with reservoirs, plumbing, a peristaltic pump, and a 3D printed flow cell. 27

Figure 2.10: Measured current (mA) during a constant voltage charge-discharge cycle with a 3D printed cell and microporous separator. 27

Figure 2.11: Measured charge (coulombs) during a constant voltage charge-discharge cycle with a 3D printed cell and microporous separator. 28

Figure 3.1: Molecular structure of the covalently linked redox couple *PDO-L-AP*. It was chosen for demonstration purposes because of it was inexpensive and had a relatively simple synthesis procedure. 31

Figure 3.2: *PDO-L-AP* in each of its three oxidation states during charging and discharging of the flow battery. Cyclic voltammetry of *PDO-L-AP* performed in propylene carbonate/0.2M $TEABF_4$ using a Pt disc working electrode, a Pt/Ti wire anode, and an Ag wire as a pseudo reference electrode, at a scan rate of 100 mV/s. 34

Figure 3.3: Flow cell experimental setup showing the dual syringe pumps, potentiostat, gas-tight glass syringes, and flow cell. 35

Figure 3.4: Cyclic charge-discharge experiments over 200 cycles using a current of 50 mA over the first 100 cycles, followed by 20 mA from cycle 101 to cycle 201. . 37

Figure 3.5: Cyclic charge-discharge experiments over 200 cycles while using a current of 20 mA over the first 100 cycles, followed by 10 mA from cycle 101 to cycle 201. 37

Figure 3.6: Results from single recirculated constant 2.4 V charge-discharge cycle with equivalent flow rates. When the pumps change directions the solution momentarily stalls causing a rapid decrease in current. 38

Figure 3.7: Single recirculated constant 2.4 V charge-discharge cycle with a charging flow rate (5 mL/min) that is half the value used while discharging (10 mL/min). 39

Figure 3.8: Single recirculated constant 2.45 V charge-charge cycle with equivalent flow rates. 40

Figure 3.9: Single recirculated constant 2.5 V charge-discharge cycle with equivalent flow rates. 40

Figure 4.1: Diagram of an RFB that includes the current collector, porous electrode, membrane (separator for proposed linked chemistry), pumps, and the tanks. Several types of losses exist within an RFB and can be associated with different components including ohmic, mass-transfer, and charge-transfer losses. 44

Figure 4.2: Resulting bode plot fit with a theoretical equivalent circuit model. The dots are the experiment points measuring impedance at various frequencies and the solid line is the equivalent circuit model's fit. 56

Figure 4.3: Resulting nyquist plot fit with a theoretical equivalent circuit model. The dots are the experiment points measuring impedance at various frequencies and the solid line is the equivalent circuit model's fit. 57

Figure 4.4: Experimental parameters and lumped cell resistance comparing an ion-selective membrane (Nafion 117) and a simple microporous separator (Celgard 2400). . . 57

Figure 4.5: Equivalent circuit developed to evaluate RFBs using EIS. 58

Figure 5.1: An SOEC's oxygen electrode and electrolyte layers shown with the boundary conditions and governing equations. These describe the flux J of each of the species in the electrode and electrolyte layers. The model domain includes a small section of YSZ and GDC layers a single particle of LSCF particle having Width (W) and length (l) of 20 μm. 64

Figure 5.2: Diagram of idealized model domain which represents the complex electrode structure with cylindrical geometry. 66

Figure 5.3: Diagram of transport pathways and equations and diagram of Helmholtz Model used to demonstrate the separation of charge at an electrode-electrolyte interface. Note that (s_{ad}) represents adsorption sites on the surface of the electrode. 67

Figure 5.4: Comparison of oxygen electrode overpotential as a function of current density in both the single and bilayer configurations. 70

Figure 5.5: Operating voltage vs. current ratio with different oxygen desorption (a) and oxygen evolution (b) reaction kinetics for single LSCF layer configuration. . . . 71

Figure 5.6: Operating voltage vs. current ratio with different oxygen desorption (a) and oxygen evolution (b) reaction kinetics for LSCF/SCT bilayer layer configuration. 72

Figure 5.7: Operating voltage vs. surface coverage with different oxygen desorption (a) and oxygen evolution (b) reaction kinetics for single LSCF layer configuration. . 73

Figure 5.8: Operating voltage vs. surface coverage with different oxygen desorption (a) and oxygen evolution (b) reaction kinetics for LSCF/SCT bilayer layer configuration. 74

Figure 5.9: Lattice oxygen stoichiometry profile as a function voltage for both the single and bilayer configurations. 74

Figure 5.10: Operating voltage vs. lattice oxygen stoichiometry with different oxygen desorption (a) and oxygen evolution (b) reaction kinetics for single LSCF layer configuration. 75

Figure 5.11: Operating voltage vs. lattice oxygen stoichiometry with different oxygen desorption (a) and oxygen evolution (b) reaction kinetics for LSCF/SCT bilayer layer configuration. 75

Figure 5.12: Total current density vs. operating voltage with different oxygen desorption (a) oxygen evolution (b) reaction kinetics for single LSCF layer configuration. . 76

Figure 5.13: Total current density vs. operating voltage with different oxygen desorption (a) oxygen evolution (b) reaction kinetics for LSCF/SCT bilayer layer configuration. 77

Figure 5.14: Performance comparison among single SCT layer, LSCF/SCT bilayer, and LSCF single layer configuration: (a) current ratio vs voltage (b) lattice oxygen stoichiometry vs voltage (c) voltage-current curve. 77

Figure 5.15: Comparison of lattice oxygen stoichiometry and current density under different operating voltage for single LSCF layer and LSCF/SCT bilayer design. . . . 78

Figure 6.1: Open circuit potential of 1 e^- and 2 e^- novel redox couples developed at MSUBI. 83

Figure 6.2: Various e^- donating, accepting, and linking species. Different combinations are under development leading to improvement in performance and practicality. 84

Figure 6.3: Detailed images of the microstructure of the electrode can be integrated into the model domain as complex, high fidelity geometries. This improves the accuracy of the model by gaining the ability to accurately represent the tortuous electrode structure. 85

Figure A.1: Image of the molecular structure of Link-2B. 87

Figure A.2: Monitoring persistence of oxidized Link-2B using optical spectroscopy. 87

Figure A.3: The persistence of the reduced form of Link-2B as a function of time, as measured by UV-visible spectroscopy. No degradation was observed over 3 days. 88

KEY TO SYMBOLS

$^{\circ}C$	Degrees celsius
\$	Dollars
$1D, 2D, 3D$	One, two, and three dimensional
$2PB$	Two-phase boundary
$3PB$	Three-phase boundary
A	Amps
A_c	Cross-sectional area (m^2)
ABO_3	Perovskite crystal structure chemical formula
ACN	Acetonitrile
Ag	Silver
C	Coulombs
c_{add}	Additional system costs (\$)
c_{bop}	Balance of plant costs (\$)
$c_{m,i}$	Cost per unit mass of the electrode ($\frac{\$}{kg^2}$)
c_a	Cost per unit area($\frac{\$}{m^2}$)
c_i	Concentration of species i (M)
C_{kWh}	Cost per kWh of system ($\frac{\$}{kWh^2}$)
c_{sys}	System costs (\$)
CA	Chronoamperometry
CCD	Cyclic charge-discharge
CF_3KO_3S	Potassium trifluoromethanesulfonate
$C-L-A$	Catholyte-linker-anolyte
cm	Centimeter
$CPE_{E,F}$	Constant phase element
CV	Cyclic voltammetry

D	Diameter (m)
D_i	Molecular diffusivity of species i ($\frac{m^2}{s}$)
δ	Lattice oxygen stoichiometry
DOE	Department of Energy
e^-, e'	Electron (traditional/kroger vink notation)
E_{eq}	Equilibrium potential (V)
E_d	Discharged energy (kWh)
EIS	Electrochemical impedance spectroscopy
F	Faraday's constant 96485($\frac{C}{mol}$)
$f_{x,y}$	Body force (N)
Fc	Ferrocene
g	Gravity ($\frac{N}{m^2}$)
GDC	Gadolinium-doped ceria
GWh	Gigawatt-hour
$h^{\cdot}$	Electron holes
H_2	Hydrogen gas
H_2SO_4	Sulfuric acid
i	Current density($\frac{A}{m^2}$)
i_o	Exchange current density ($\frac{A}{m^2}$)
J	Joule
J_i	Molar flux of species i ($\frac{mol}{m^2 s}$)
K	Kelvin
k_i	Rate of reaction i ($\frac{M}{s}$)
K_i	Ionic conductivity of species i ($\frac{s^3 A^2}{kg^1 m^3}$)
KBF_4	Potassium tetrafluoroborate
kg	Kilogram
KOH	Potassium hydroxide

KPF_6	Potassium hexafluorophosphate
kWh	Kilowatt-hour
l	Length (m)
L	Liter
L_{EIS}	Inductance ($\frac{kgm^2}{s^2A^2}$)
$LCOE$	Levelized cost of energy ($\frac{\$}{kWh}$)
$LDES$	Long duration energy storage
$LiPF_6$	Lithium hexafluorophosphate
$LSCF$	Lanthanum strontium cobalt ferrite
m	Meter
M	Molarity ($\frac{mol}{L}$)
m_i	Mass of electrode (kg)
mA	Milliamp
mAh	Milliamp-hour
$MIEC$	Mixed ionic and electronic conducting
min	Minute
mol	Moles
MSU	Michigan state university
$MSUBI$	Michigan state university bioeconomy institute
MV	Methyl-viologen
$mvrms$	Milli-volt root mean square alternating current signal
MW	Megawatt
N	Newton ($\frac{kgm}{s^2}$)
N_i	Flux term relative i (stationary) ($\frac{mol}{m^2s}$)
$NaBF_4$	Sodium tetrafluoroborate
$NaCl$	Sodium chloride
$NaClO_4$	Sodium perchlorate

Ni	Nickel
nm	Nanometer
$NREL$	National renewable energy laboratory
$O_{2(g)}$	Oxygen gas
O^X	Oxide ions O^X (kroger vink notation)
p	Pressure (Pa,psi)
P_o	Total cost of system ($)
Pa	Pascal
PbO_2	Lead dioxide
PC	Propylene carbonate
$PDO-L-AP$	4-phenothiazine 5,5-dioxide– propyl chain–4-acetylpyridinum
psi	Pound-force per square inch
Pt	Platinum
R	Gas constant 8.314 ($\frac{J}{(}molK$)
R_{CT}	Charge-transfer resistance (Ω)
R_{HF}	Lumped cell resistance (Ω)
R_{MT}	Mass-transfer resistance (Ω)
R_{oh}	Ohmic resistance (Ω)
R_E	Electrode resistance (Ω)
r_i	Reaction source term for species i ($\frac{kg}{m^3 s}$)
RFB	Redox flow battery
s	Seconds
S	Siemens
s_{ad}	Oxygen adsorption site on the surface of a MIEC
SCT	Strontium cobalt oxide
$SIMPLE$	semi implicit method for pressure-linked equations

$SIMS$	Secondary ion mass spectrometry imaging
$SOEC$	Solid oxide electrolyzer cells
T	Temperature (K, $^{\circ}C$)
t_d	Discharge time (hours)
$TEABF_4$	Tetraethylammonium tetrafluoroborate
Ti	Titanium
TWh	Terawatt-hour
u_i	Mobility of species i ($\frac{m^2}{Vs}$)
$u_{x,y,z}$	Velocity in x, y, or z direction ($\frac{m}{s}$)
UML	University of massachusetts-lowell
USC	University of south carolina
$V^{\cdot\cdot}$	Oxygen vacancy
V	Volts
V_{cell}	Operating potential (V)
W	Width
x_i	Molar fraction of species i
YSZ	Yttrium-stabilized zirconia
z_i	Charge number of species i
$\alpha_{a,c}$	Charge transfer coefficient(Anodic,Cathodic)
ξ	Porosity
Δ	Differential operator
η_s	Surface overpotential (V)
μ_{Re}	Dynamic viscosity (Pa s)
μ_i	Chemical potential of species i ($\frac{J}{mol}$)
μm	Micrometer
∇	Vector differential operator
ν	Kinematic viscosity ($\frac{m^2}{s}$)

ϕ	Potential (V)
ω	Resistance (ohms)
Ω	Warburg element
ρ	Density ($\frac{kg}{m^3}$)
σ_i	Electrical conductivity of species i ($(\frac{S}{m})$)
θ	Lattice oxygen site coverage

CHAPTER 1

GRID-SCALE ENERGY STORAGE TECHNOLOGIES, RESEARCH OBJECTIVES, AND METHODS

Grid-scale energy storage technology research is becoming more important as the implementation of renewable energy sources becomes more prominent. Many forms of power generation such as: wind, solar, and tidal energy can't be relied on for base generation due to their tendency to be intermittent. Grid-scale long duration energy storage allows excess energy produced during operation to be stored. It can then be used when energy generation capacity cannot match demand. Integration of energy storage technology for grid scale implementation has benefits for the electric-grid that include:

- stabilizing the grid to prevent blackouts during peak demand;
- allowing current generation technologies such as coal or natural gas power plants to operate more efficiently by reducing fluctuations in production;
- providing consistent pricing;
- taking advantage of low-cost renewable resources;
- allowing emergency preparedness, which is vital when no transmission or generation or is possible;
- enabling the development of smart-grids;
- and reducing carbon emissions.

Table 1.1 lists energy generation technologies with their associated Levelized Cost of Energy (LCOE) for various generation technologies(1). A report analyzing the cost of energy generation and storage technologies is released annually by Lazard Ltd. It is used by utilities and munici-

palities when planning the construction of power plants. Renewable resources, fossil fuel burning technologies, and nuclear generation systems were evaluated.

The most inexpensive form of traditional energy generation technology (gas, nuclear, and coal) is combined cycle natural gas with a LCOE as low as 0.04 $\$/kWh$. These power plants operate by the principles of the Brayton (combustion turbines) and Rankine cycles (steam turbines). Over the past decade the LCOE for renewable energy generation technologies sources, including wind and solar, has dropped dramatically. According to Lazard's annual report, the unsubsidized LCOE for new wind and utility scale thin film photovoltaics was a mere 0.03 $\$/kWh$(1).

Table 1.1: 2020 levelized cost of energy for various forms of renewable and nonrenewable generation technologies.

Levelized Cost of Energy Comparison—Unsubsidized Analysis	($\$/kWh$)
Natural Gas (Peaking)	0.15
Nuclear	0.13
Coal	0.07
Natural Gas (Combined-Cycle)	0.04
Solar Photovoltaics (Thin Film Utility-Scale)	0.03
Wind	0.03

Renewable sources suffer from their tendency to be intermittent and have peak generation capacity at times when the demand is low. Development of Long Duration Energy Storage (LDES) enable the widespread adoption of inexpensive renewable energy sources. Analysis suggests that if much more than 20% of the United States' energy is produced by renewable resources, the grid could become destabilized(2). The rise in efficiency of renewable energy systems (and rapid decrease in cost), varying fossil fuel prices, as well as environmental concerns, is creating a rise in installation of renewable energy systems. The electric-grid operates by generating enough energy to fill the demand at any given time. A key to unlocking the potential of renewable energy systems is low cost, efficient, easily deployable, grid storage. The Department of Energy (DOE) has promoted the development of grid storage technology to enable extensive integration of intermittent renewable energy resources into the national electric-grid(3).

Transitioning away from burning fossil fuels for energy generation is seen as critical to avoid the

worst effects of climate change. Analysis has shown suggested that achieving net-zero emissions by 2050 is required to limit global temperature rise to $1.5^{\circ}C$(4). This is seen as a necessary limit to avoid the worst impacts of climate change. The Biden administration sees this as the greatest challenge facing the United States and the world(5). The federal government has set milestones and encouraged the development of technologies necessary to produce clean energy and build a more resilient grid. A study published by Princeton University provides granular guidance on what getting to net-zero really requires and on actions needed to translate pledges to reach net-zero emissions into tangible progress(6). This will require the installation of many Terawatts of renewable power sources of over the next 30 years. LDES will be coupled with these generation resources meaning development of grid-scale energy storage technologies is critical for the coming transition away from burning fossil fuels.

Various storage technologies exist or are being developed including li-ion batteries, flow batteries, pumped hydro, compressed air, fly-wheels, advanced heat exchangers, and electrolyzers. Each of these technologies stores energy in one form or another. Electrochemical, chemical, mechanical, thermal, electrical or thermal energy is stored and then released as usable electrical energy. This thesis will describe the two technologies which are the focus of this study: Redox Flow Batteries (RFBs) and Solid Oxide Electrolyzer Cells (SOECs). RFBs operate similarly to a combination of electrolyzer while charging and a fuel cell while discharging. Contrary to typical battery technologies where the reactants are part of a solid electrode, the reactants within an RFB are dissolved into an electrolyte solution which is circulated through an electrochemical cell(7). SOECs operate as fuel cell in reverse, using electrical energy to produce hydrogen by splitting water molecules through electrolysis(8). The H_2 can be stored and used in fuel cells in a recombination reaction to release usable electrical energy and form water molecules.

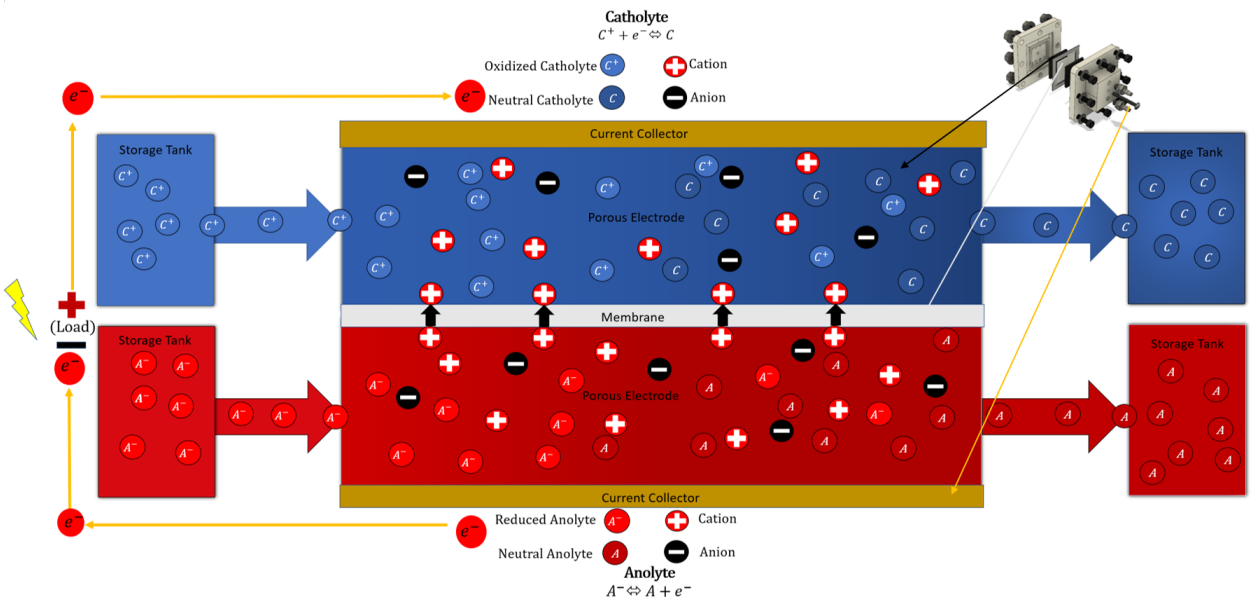

Figure 1.1: A diagram of an RFB showing the storage reservoirs, membrane, active material in charged and neutral oxidation states (C, C^+, A, A^-), charge balancing electrolyte ($+$, $-$), current collectors, porous electrodes, an exploded view of a three-dimensional model (upper right), and the oxidation and reduction reactions. This RFB is depicted as discharging when flowing from left to right an charging when flowing right to left.

1.1 Grid-Scale Energy Storage Technologies of Interest

1.1.1 Redox Flow Batteries

RFBs are ideal candidates for low cost, highly scalable, energy storage media in part because they incur modest long-term maintenance and operational costs. A key feature of RFBs is that the electrolyte solution, containing electroactive compounds, is stored independently of the power producing electrochemical cells. One of the greatest advantages of flow batteries is that the power extraction system is sized independently of its energy storage capacity. This separation of power production and energy storage allows for easy scale-up operations required for increased electrical storage or production, e.g. energy storage for electric grids. This characteristic allows the ease of capacity scale up and opens the possibility for battery repairs without complete disassembly. As shown in Figure 1.1 the active material is stored separately from the active battery flow cell. By pumping the liquid through the flow cell, which contains a porous electrode and separation device,

the active species can be charged and discharged.

1.1.2 Hydrogen Generated using a Solid Oxide Electrolyzer Cell

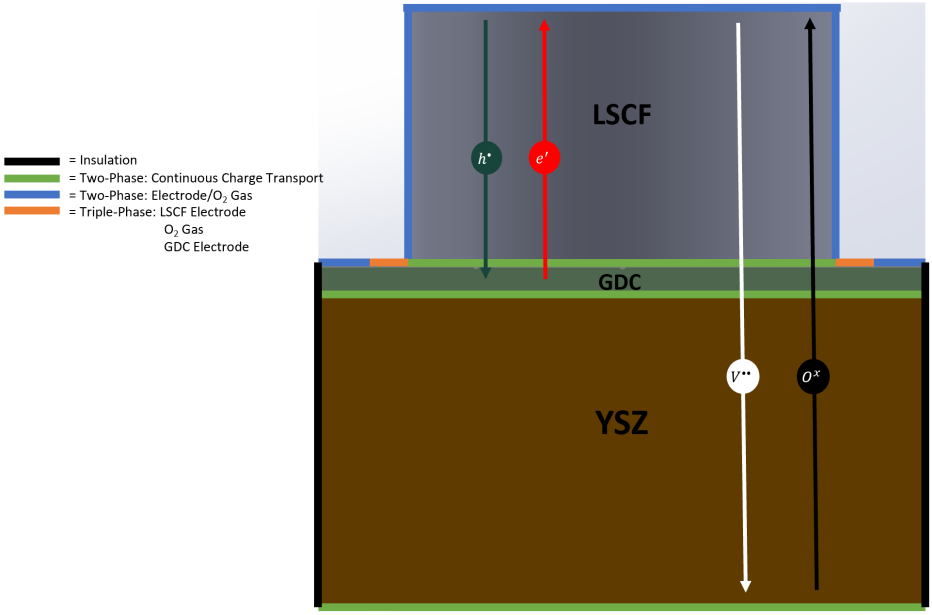

Figure 1.2: Diagram showing each layer of the SOEC and the species involved which includes the primary charge carrier oxygen ions (O^X), oxygen vacancies ($V^{\cdot\cdot}$), electrons (e'), and electron holes ($h^{\cdot}$). e' and $h^{\cdot}$ move opposite of one another and are only present in the LSCF and GDC layers while O^X and $V^{\cdot\cdot}$ are present in each layer. Several types of two and three-phase boundaries exist including continuous charge transport, electrode/gas, and multi electrode/gas interface.

SOECs are an appealing electrolysis technology because they do not require an expensive catalyst, such as platinum(9). They operate at high temperatures ranging between $100°C$ and $850°C$ to increase the rate of the reaction, which leads to greater efficiencies(10). Figure 1.2 depicts an SOEC consisting of a solid-state electrolyte consisting of Yttrium-Stabilized Zirconia (YSZ), a Mixed Ionic and Electronic Conducting (MIEC) buffer layer of Gadolinium-Doped Ceria (GDC), and a Lanthanum Strontium Cobalt Ferrite (LSCF) MIEC electrode. The charged species transport in each layer is shown and the types of boundaries are shown in Figure 1.2. YSZ is a pure ionic conductor, with oxygen vacancies being the only mobile species; GDC is a mixed oxygen vacancy (high) and electron (low) conductor, and the transference number depends on the gas

composition and temperature; LSCF is also a mixed conductor, but with much higher electron hole conductivity than that of oxygen vacancy. The dopant is immobile and maintains charge neutrality together with other active species.

SOECs suffer from premature delamination of the electrode from the electrolyte, but the primary mechanism responsible for this is not well understood(8; 11; 12; 13). It has been hypothesized that competition between the two/three-phase boundaries (2PBs and 3PBs) leads to unbalanced lattice structure expansion which results in delamination.

1.2 Research Objectives, Studies Performed, and Structure of Dissertation

Chapters 1-5 are focused on the development of a unique flow battery that could address several issues which plague typical RFBs. These include high cost and crossover induced capacity fade that requires expensive rebalancing. A covalently linked redox couple is studied and is referred to as *PDO-L-AP* or D_2A_2. The novel redox couple allows the use of a microporous separator which decreases cost and eliminates the need for expensive rebalancing when crossover does occur. Chapter 6 details a series of studies aimed at understanding, redesigning, and preventing electrode/electrolyte delamination in SOECs. This is to extend their usable lifespan which improves their economic viability.

Initial spectroelectrochemical analysis, summarized in A.1, of novel linked-redox couples was performed at the Michigan State University Bioeconomy Institute($MSUBI$). Once complete, it was necessary to study the performance of the novel redox chemistry in a flow cell. An inexpensive flow cell, test station, and experimental method was developed to gauge the practicality of the proposed redox couple. Additive manufacturing (commonly referred to as 3D printing) techniques were employed for rapid prototyping of a RFB cell. Readily available parts were acquired to build a inexpensive test station that was used to demonstrate the linked chemistry in a 3D printed cell. Chapter 1 summarizes initial experiments and modeling which were carried out to address several questions:

- Can the novel redox couple be charged and discharged in a flow cell without the use of an

ion-selective membrane?

- Can a relatively inexpensive benchtop 3D printer be used for rapid prototyping of flow cells?
- Does the proposed chemistry and the use of a microporous separator impact the cost enough to make RFBs more economically appealing?

These queries were addressed through computational and experimental methods. Charging and discharging of the prototype RFB was conducted after a complete test station and experimental method were developed. Computational fluid dynamics was used to model the flow of solution within the cell to ensure uniform distribution of active species throughout the reaction chamber and to assess pressure drop across the flow field. Two potential flow cell geometries were compared. The use of a simple microporous separator was studied as a means to further reduce cost. To analyze the financial impact this would have, a techno-economic analysis was performed.

For an experimental redox couple to be commercially viable, experiments that included charging and discharging for many cycles would be required. Chapter 3 describes stability and electrochemical performance studies using the novel linked redox couple, a commercial flow battery test fixture, and a simple microporous separator. These studies were performed to answer questions including:

- Can the proposed redox couple remain stable when cycled over hundreds of cycles?
- How does the solvent effect overall performance?
- When flow is introduced, how can active material conversion be maximized?
- How do charging potential and flow rate effect current, capacity, and coulombic efficiency?

Preliminary viscosity and solubility measurements were conducted to aid in the selection of a nonaqueous solvent and supporting electrolyte salt these are summarized in the Appendix in Table A.2 and Table A.1. Static cyclic charge-discharge experiments were performed, with solutions of identical concentrations of active material and charge balancing electrolyte in two different organic solvents. Flow studies were performed to investigate operational parameters' impact on overall

performance. A two-electron system (Link-2B) was explored explored late in this project, but testing was limited to repetitive bulk electrolysis and zero-flow RFB runs due to limited material availability. Still, it was shown that Link-2B exhibited rapid electrode kinetics and excellent stability in the charged state and will be the focus of future work.

Many factors impact the performance of an RFB. Chapter 4 describes the employment of electrochemical impedance spectroscopy to evaluate internal losses stemming from the membrane within the cell. Losses associated with an ion-selective membrane are compared to those from a simple microporous separator. While performing literature review, running experiments, and analyzing data, several questions came to mind:

- What impact do individual components of an RFB have on internal losses and overall performance?
- How can this be measured?
- What methods exist to analyze and understand the data associated with these measurements?
- It was hypothesized that a microporous separator will be less resistive than an ion-selective membrane. If this is true, how much less?

Categorizing losses that exist within RFBs is discussed. Impedance measurements are taken. Data analysis using equivalent circuit models is used to compare an ion-selective membrane and microporous separator, which are the primary focus of this study. Using the procedure and analysis techniques described, further impedance studies can be performed to continuously improve the performance.

Chapter 5 summarizes the development of a microscale model to investigate SOECs. The primary goal was to determine the most significant delamination mechanism that leads to a shortened lifespan. To improve performance and the viability SOECs as a grid-scale energy storage technology, several questions were answered in this chapter:

- How are charged species transported within the solid-state electrolyte and multilayer electrode?
- Are the reactions that take place purely chemical or electrochemical in nature?
- What will the model domain encompass and how should each interface be treated?
- How can the proposed model be periodically validated to ensure accuracy?
- What can be done to prevent delamination?
- What can be done in future work to further improve the reliability of the model?

Literature review, model theory and development, and incremental experimental validation methods were used to investigate these questions. Future studies will address generally overlooked, localized, and possibly crucial transport phenomena. High-fidelity geometries, which can be reconstructed from 3D images taken using advance synchrotron-based techniques, will be incorporated into the model to further improve its accuracy. This will aid in properly describing transport phenomena and physics within an SOEC. Delamination prevention techniques can be developed to improve the viability of SOECs as a grid-scale energy storage technology.

CHAPTER 2

DEVELOPMENT OF A MEMBRANELESS ORGANIC REDOX FLOW BATTERY

2.1 Introduction

This chapter summarizes early design and testing of a symmetric RFB that does not require an ion-selective membrane. The experiments described used a 3D printed flow cell and inexpensive test station. A brief review of literature review and techno-economic analysis were performed to investigate the advantages that a membraneless RFB has over its ion-selective counterpart. The covalently linked redox couples are briefly described. They will be the focus of future studies when more active material can be synthesized. Computational Fluid Dynamics (CFD) was used to investigate flow distribution within the reaction chamber and compare two potential cell geometries by evaluating pressure drop across the cell. Initial cycling experiments using a 3D printed cell are summarized and the results are presented using a mixed solution containing both ferrocene and methyl-viologen. This catholyte-anolyte mixture can also operate without an ion-selective membrane, making it a suitable candidate while developing a testing procedure and system.

Table 2.1: Common RFB chemistry proposed in literature compared with the novel linked redox couple.

RFB Chemistry	**Cell Voltage (V)**	**Ion-Selective Membrane**
All Vanadium	1.26	Yes
Bromide-Polysulfide	1.355	Yes
Zinc-Cerium	2.04	Yes
Soluble Lead-Acid	1.62	No
Iron-Chromium	1.18	Yes
Liquid Bromine-Hydrogen	1.07	No
$C-L-A$ (Proposed)	>2	No

2.2 Membraneless Redox Flow Battery Literature Review

RFBs were first developed in the 1980s(14). Several RFB chemistry concepts and system designs have been proposed to meet the need for low cost, efficient, reliable, easily deployable grid storage. Table 2.1 lists various RFB anolyte and catholyte compounds proposed in past work accompanied by their cell voltage(14; 15; 16; 17; 18; 19; 20). These systems all require an ion-selective membrane, except for the soluble lead-acid chemistry. In the soluble lead-acid RFB, a membrane is not required because only one active species is present, Pb^{2+}. The electrode reactions cause the precipitation of soluble species into solid Pb and PbO_2 during the charge cycle and re-dissolution during the discharge cycle. Unfortunately, hydrogen evolution is observed during the charge cycle at high state-of-charge, which reduced the storage capacity of the system and can lead to an explosion(14).

The zinc-cerium and soluble lead-acid flow batteries are known as "hybrid" redox flow batteries because of the depositing of metal at the electrode. To be defined as a hybrid RFB, one or more of the electroactive components must be deposited as a solid layer. Zinc-cerium RFBs have been under development since 1990s and have a much higher cell voltage compared to the other systems in Table 2.1, but no commercially available system is available due to cost constraints.

Initial RFB systems consisting of hybrid iron-chromium species, were hindered by prohibitive membrane cost and low operational cell voltage(14; 21; 22; 23; 24; 25; 26). Bromide-polysulfide RFBs are relatively cost effective but include a membrane and can potentially release a highly toxic bromine vapor. Another RFB chemistry that does not require a membrane is the liquid bromine-hydrogen system. The compounds are pumped through a channel using laminar flow. The chemical reactions that take place, combined with the laminar flow, allows the system to operate without an ion-selective membrane. The drawback of this system is its relatively low cell voltage. A lower cell voltage leads to a lower power capacity of the system. This would also require a larger system and more of the chemical compounds to store the same amount of energy as systems with a higher cell voltage. Organic RFBs have only recently emerged and have enabled systems to overcome the economic constraints as well as allowing for the development of higher energy

density chemistry(14).

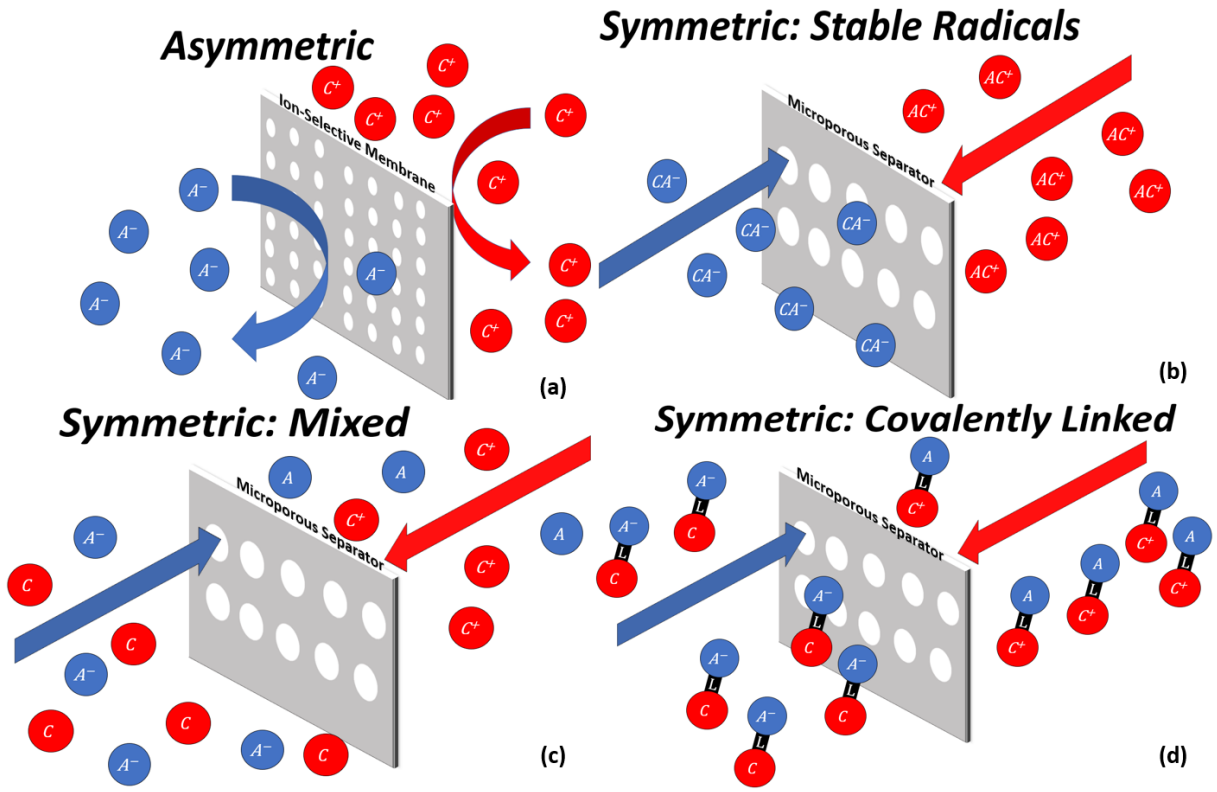

Figure 2.1: (a)Asymmetric redox flow batteries use an ion-selective membrane to maintain separation between the anolyte A and catholyte C species.The arrows are shown to represent the membrane rejecting active species from crossing over.(b) Symmetric redox flow battery using a stable radical as both the anolyte A and catholyte C. The arrows represent the non-selectivity of a microporous separator. (c) Symmetric redox flow battery using a mixed solution on both sides of the cell containing both the A and C. (d) Symmetric redox flow battery using a covalently linked anolyte-catholyte $A-L-C$ bipolar molecule.

Typical RFBs operate using an ion-selective membrane to separate the anolyte and catholyte containing solutions. These are referred to as asymmetric RFBs with an example shown in Figure 2.1(a)(27). An asymmetric flow battery consists of a completely separated anolyte and catholyte solution separated by an ion-selective membrane. This strategy attempts maintain a balanced system by hindering crossover, but crossover still occurs. Ion-selective membranes are also expensive and periodic rebalancing is required from inevitable crossover.

To address crossover induced capacity fade, bipolar redox-active molecules, in different oxidation states, can be used as both the anolyte and catholyte(28). Three strategies exist while

developing bipolar redox-active molecules including: synthesis of stable radicals which can be used in both reduction and oxidation reactions, physically mixing electroactive species to form an equimolar mixture, and covalently mixing electron donating and accepting pairs. Figure 2.1(b) shows a diagram of a symmetric RFB with a stable radical prone to both positive and negative reactions used as both the anolyte and catholyte. This allows the use of a microporous separator, but still suffers from fairly high rates of crossover. Figure 2.1(c) shows a diagram of a symmetric RFB using a mixed anolyte-catholyte solution on both sides of the cell(27). This method has been proposed to decrease the cost and also allow for simple remixing to correct for crossover caused by osmotic pressure differences(29). Covalently linking an anolyte-catholyte redox couple reduces the impact of crossover. A diagram of this configuration is shown in Figure 2.1(d). The primary benefits that it has over other symmetric RFBs is that energy density is improved by reducing the footprint that the individual active species have and iterative molecular improvement is possible.

2.3 Covalently Linked Redox Couple

A covalently linked redox couple is under consideration and can be coupled with an organic solvent (nonaqueous). The primary advantage of a nonaqueous solvent system over an aqueous one is the prospect of higher operating voltages. In the absence of fortuitous kinetic effects, the operating voltage of an aqueous RFB system is functionally capped at a maximum of 1.2 V due to the electrolysis of water, while nonaqueous systems can achieve voltages well over 2 V with favorable system conditions(30; 31; 32). Figures 2.2 and 2.3 shows the molecular structure of the proposed compounds and the results from electrochemical experiments.

One critical challenge in the development of practical nonaqueous RFBs is the prevention of crossover (cross-contamination of the catholyte and anolyte materials). This is paramount to the survival and longevity of the system and is usually accomplished by incorporating an ion-selective membrane such as Nafion. However, such membranes are costly to install and maintain, possess a limited life span due to contamination, and can negatively impact system efficiency(30; 33; 34).

The RFB materials described herein resolve this issue by covalently linking the catholyte and

anolyte groups to yield $C-L-A$ systems (where C is an electron donor, A is an electron acceptor, and L denotes a linker). This provides three stable oxidation states in the same compound. The oxidized form $C^{+}-L-A$ serves as the catholyte, while the reduced form $C-L-A^{-}$ functions as the anolyte. The resultant half reactions produce the identical product ($C-L-A$) at each electrode, making crossover completely irrelevant, which allows simple, inexpensive porous separators to be utilized rather than ion-exchange membranes. To ensure market viability, redox active materials must possess robust electrochemical stability, high solubility, and low molecular weight (per electron transferred). Ideally, these materials should also undergo oxidation/reduction at potentials that will maximize cell voltage and can be easily manufactured at low cost(32; 35).

Modified carbazoles, phenothiazines, and phenothiazine 5,5-dioxides have been prepared as electron donating groups. This trifecta has been found to exhibit excellent solubility while simultaneously demonstrating high oxidation potentials in nonaqueous solvents. Conversely, extended viologen systems have been examined as electron accepting anolyte materials that undergo highly reversible electrochemical reduction at low potentials. Linking of these materials provides an additional benefit by allowing for the independent optimization of relevant donor and acceptor properties such as redox properties, solubility, and synthetic route(36; 37; 38).

Compound 1 is an example of a $C-L-A$ active material that was prepared by attaching a substituted carbazole unit to 4-acetylpyridine via a propyl linker. This concept has also been extended to multielectron systems, and several $C-L-A-L-C$ compounds have been prepared. In these systems, C is a one-electron acceptor (Catholyte) while A is a two-electron donor (Anolyte). Compound 2 represents one such example that was recently prepared in our laboratory, and is capable of a net two-electron operation at over 2.3 V. Cyclic voltammetry of compound 1 reveals two reversible couples at approximately -0.60 V and 1.27 V vs. Fc/Fc^{+}. The first of these represents a one-electron reduction of the 4-acetylpyridine moiety, consistent with previously reported data from Sanford's group(36; 38). The second couple is a one-electron reduction of the carbazole moiety(35). Similarly, Figure 2.3 shows two reversible couples for compound 2, a reduction at approximately -0.89 V and an oxidation at approximately 1.43 Vs. Fc/Fc^{+}. In

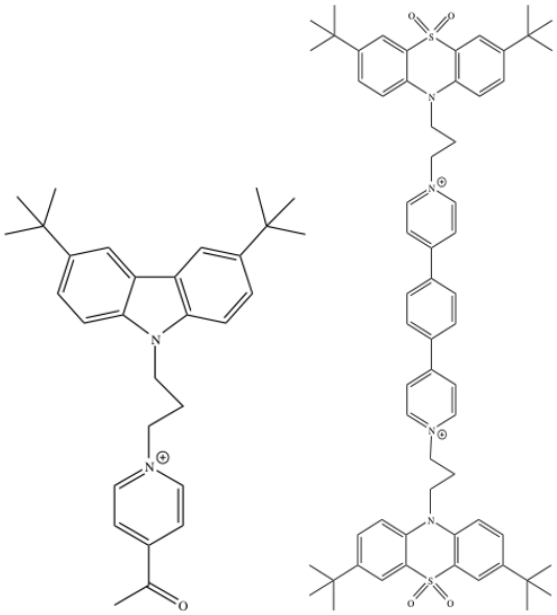

Figure 2.2: Compound 1 (left) is an example of a model $C-L-A$, compound 2 (right) is a prepared $C-L-A-L-C$ system using an extended bis-pyridinium acceptor covalently linked to phenothiazine 5,5-dioxide donor groups.

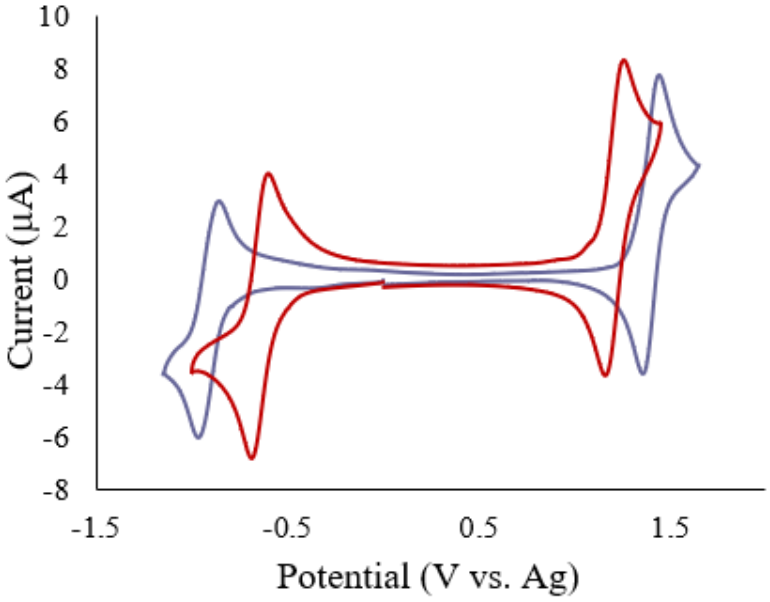

Figure 2.3: Cyclic voltammograms of compounds 1, in red, and 2, in blue. Both voltammograms were produced using a 0.2 M $TEABF_4$ solution of propylene carbonate, a Pt disc working electrode, a Pt/Ti wire anode, and a Ag wire as a pseudo-reference electrode at a scan rate of 100 and 50 mV/s for 1 and 2 respectively.

this case, the first couple corresponds to a net two-electron reduction of the phenylene-bridged bis-pyridinium acceptor, while the second, also a net two-electron process, is attributed to the superimposed oxidation of both phentahiazine-5.5-dioxide units(35). Due to a lack of funding and resources electrochemical testing was performed with a symmetric RFB containing a mixed anolyte-catholyte solution. The linked redox couple will be the focus of future studies.

2.4 Techno-Economic Analysis

To gauge the financial viability of a symmetric RFB, a techno-economic analysis was performed. Primarily comparing the impact of the membrane or separator on the capital cost. The DOE initially has set the target cost of RFBs to be under $250/kWh for 2015 and under $150/kWh as a longer-term objective(14). Darling et al. proposed that the cost of an RFB system, P_o, could be calculated using Equation 2.1(39). Where c_{add} are additional costs of the system, c_{bop} are the balance of plants cost, c_a is the cost per unit area of each cell, A is the area of the membrane, c_{sys} includes system costs (pump, plumbing, infrastructure, materials, and other costs), E_d is the discharged energy (kWh), t_d is the discharge time (h), $c_{m,i}$ is the cost per unit mass of the electrode, and m_i is the mass of the electrode. Using Equation 2.1, we can derive the cost per kilowatt-hour of the system using:

$$P_o = c_a A + (c_{add} + C_{bop}) E_d t_d^{-1} + \sum_i c_{m,i} \tag{2.1}$$

$$P_o = c_a A + (c_{sys}) E_d t_d^{-1} + \sum_i c_{m,i} m_i \tag{2.2}$$

$$C_{kWh} = P_o / E_d \tag{2.3}$$

From Equations 2.2 and 2.3, the total cost (P_o) and capital cost (C_{kWh}) of a 1-kW, 5-kWh cell was estimated based off the cost of current prototypes. With the number of stacks equal to 1000, estimates for the scaled cost of 1-MW system were obtained. A 1-MW system using microporous separators was estimated to have a cost $144/kWh. Meanwhile, the cost of a 1-MW system with an ion-selective membrane was estimated at $155/kWh.

Table 2.2: Estimated parameters included in the techno-economic analysis, performed to compare the impact that incorporation of an ion-selective membrane or a microporous separator has on the capital cost of an RFB.

Symbol	Description	Value
A	Area of electrode (m^2)	5
c_a	Cost of reactor ($\frac{\$}{m^2}$)	28/38
c_{add}	Cost of reactor ($\frac{\$}{kW}$) (microporous/ion-selective)	75
c_{bop}	Balance of plant costs($\frac{\$}{kW}$)	145
$c_{m,i}$	Cost per unit mass of species i($\frac{\$}{kg}$)	50
E_d	Energy discharged(kWh)	100
m_i	Mass of species i(kg)	144
t_d	Discharge time(h)	100

The capital costs were estimated using data available at the time this analysis was performe, which are summarized in 2.2. Using a microporous separator demonstrates additional cost savings of over $10/kWh. In calculating this cost, the electrochemical efficiency of the system was assumed to be 100%. The system of interest was analyzed assuming the cell was manufactured using 3D printing. This leads to the cell material being the largest single contributor to overall cost. The cost is expected to drop much further as processes such as injection molding could be used.

The separator between the two chambers is another key component of the RFB cell. One of the types of separators is a microporous one, which allows for liquids to cross between the two sides of the cell(2). The microporous separator tends to have a higher rate of chemical crossover, which in turn decreases the electrochemical efficiency in typical RFBs. As a result, most RFBs use an ion exchange membrane to separate the two chambers. An ion-selective membrane substantially increases the initial and long-term cost of the system. A fluorinated ion-selective membrane costs $1000/m^2 with a limited cycle life, while the inexpensive nano-porous separator costs only $10/m^2(39). The proposed chemistry would allow for the membrane in the reaction chamber to be replaced by a microporous separator, thereby lowering the cost of the cell. A separator is required to prevent an electrical short in the cell and to mediate electrolyte movement. It is noteworthy that the simple separator cost for a 1 MW system was only $537 while the ion-selective membrane was

$53,700 for the same surface area. The area (A) for the separator was calculated using the proposed energy density (E_{den}) and power requirement (Power) of the system, using:

$$A = Power/E_d \tag{2.4}$$

2.5 Computational Fluid Dynamics Analysis

To guide the design of RFB cells that could be 3D printed, a relatively simple CFD model was developed to evaluate different geometries. The commercial software ANSYS Fluent 18.2 was used to determine the pressure drop across two different RFB flow chamber geometries, often referred to as flow fields. Each geometry featured an inlet manifold, an outlet manifold, and a porous cell. The only difference between the two geometries was the cross-sectional area (A_c) of the cell. The goal of this study was to determine how the A_c influences the pressure drop and electrolyte distribution within the flow chamber. Figures 2.4 and 2.5 show the geometries used for computation. The two dimensional steady-state continuity and navier-stokes equations for incompressible flow shown as Equations 2.5, 2.6, and 2.7. These were solved to determine the pressure gradient across the cell geometries of interest. The parameters used include the fluid velocity ($u_{x,y}$), density (ρ), dynamic viscosity (ν), body force ($f_{x,y}$), and pressure (p).

$$\frac{\partial u_x}{\partial x} + \frac{\partial u_y}{\partial y} = 0 \tag{2.5}$$

$$u_x \frac{\partial u_x}{\partial x} + u_y \frac{\partial u_x}{\partial y} = -\frac{1}{\rho}\frac{\partial p}{\partial x} + \nu\left(\frac{\partial^2 u_x}{\partial x^2} + \frac{\partial^2 u_x}{\partial y^2}\right) + f_x \tag{2.6}$$

$$u_x \frac{\partial u_y}{\partial x} + u_y \frac{\partial u_y}{\partial y} = -\frac{1}{\rho}\frac{\partial p}{\partial y} + \nu\left(\frac{\partial^2 u_y}{\partial x^2} + \frac{\partial^2 u_y}{\partial y^2}\right) + f_y \tag{2.7}$$

The Reynolds Number throughout the system was below the threshold for turbulent internal flow (Re < 2300). The working fluid for this study was propylene-carbonate, which was assumed to be incompressible with constant properties. Since the reaction chamber was required to be

completely porous, the chamber of both flow fields was modeled as an incompressible carbon felt. The carbon felt used in physical tests had a permeability of 1.6 x 10^{-10} m^2 and porosity of 90%. Since effects of viscosity were considered in this study, a "no-slip" condition was applied to the walls of each flow field, along with the standard roughness model. The inlet velocity was constant, and the outlet pressure was equal to the reference system pressure. Both studies assumed the same inlet flow rate and cell length. The cross-sectional area of Geometry 1 was approximately 40% larger than Geometry 2, so Geometry 1 was expected to have a better flow efficiency.

The geometries were irregular, so a patch-conforming method was used to generate an unstructured mesh that could better capture the irregularities. A proximity and curvature scheme were used to allocate more nodes towards the edges and walls because the gradients are expected to be larger in those regions. Each mesh was generated with desirable quality and skewness factors and exported into ANSYS Fluent.

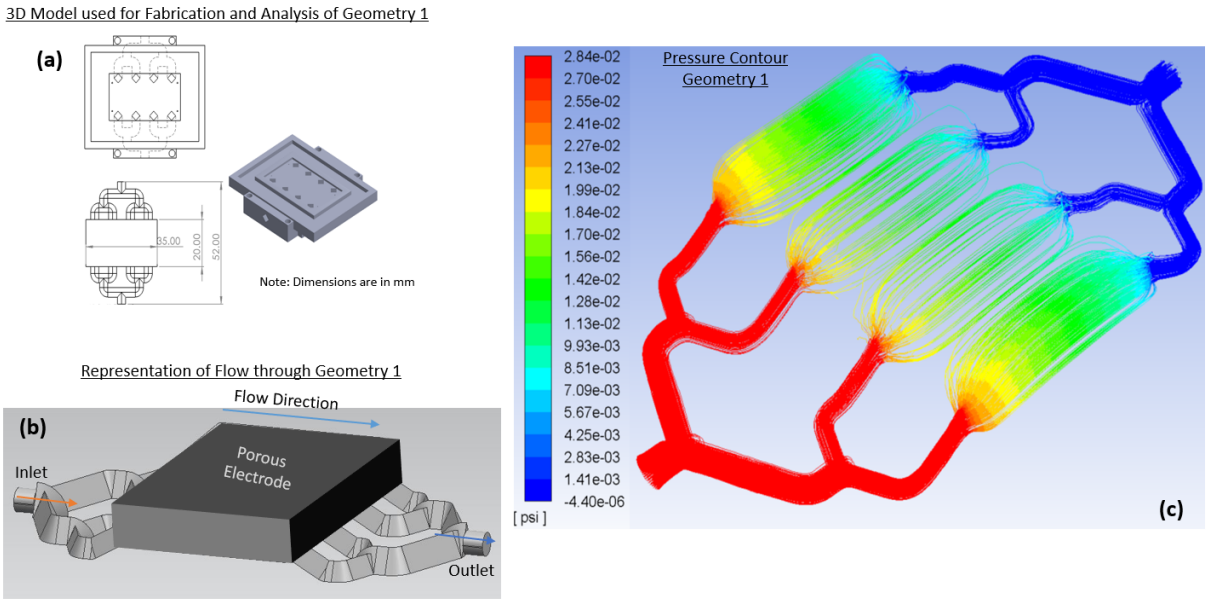

Figure 2.4: CAD model of flow cell Geometry 1(a), the geometry of the fluid within the cell(b), and the resulting pressure contour(c).

Due to the steady and incompressible assumptions for the flow field, the numerical solution was calculated using the pressure-based Semi Implicit Method for Pressure-Linked Equations (SIMPLE) algorithm. Without the pressure correction, the pressure field would not satisfy continuity,

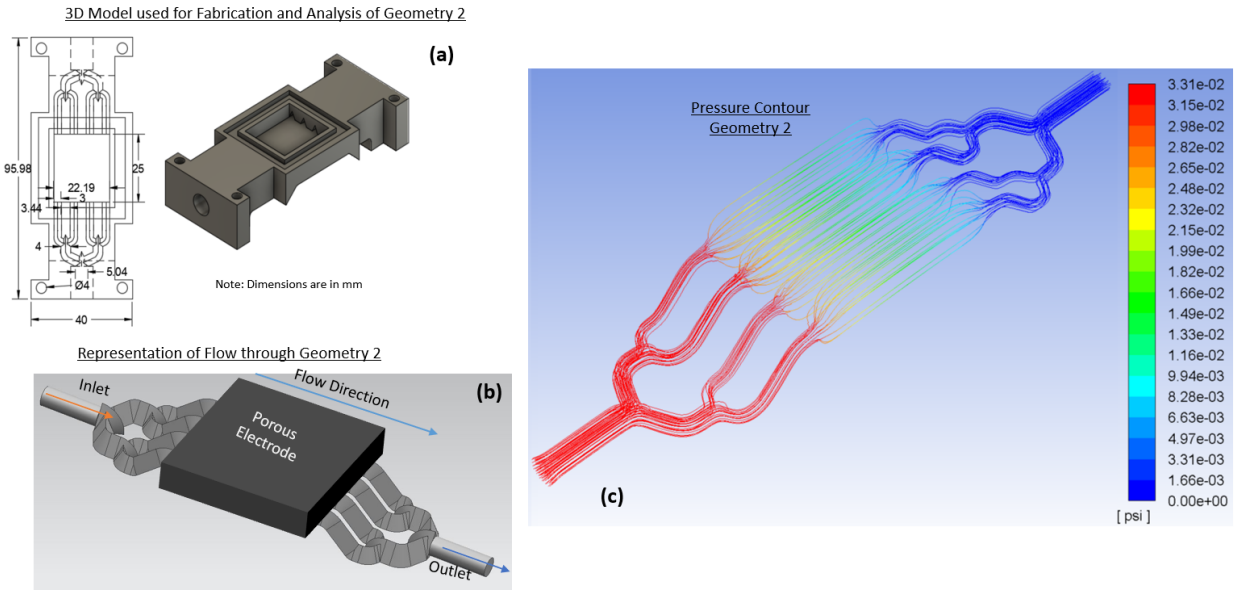

Figure 2.5: (a)CAD model of the flow within Geometry 2. The same design approach was used with the exception that it is skinnier and 40% smaller than Geometry 1 shown in Figure 2.4. (b) The geometry of the fluid within the cell. (c) Pressure contours and streamlines for Geometry 2 showing a slightly larger pressure drop but there still seems to be uniform flow.

producing non-physical results(40). To utilize this algorithm, the velocity and pressure fields are discretized across a staggered grid, limiting the non-physical solutions that would satisfy continuity and momentum equations when using a collocated grid for incompressible flow. The conservation of momentum and pressure correction equations were discretized using a second-order scheme, and the solution was calculated using double precision. A second order scheme is advantageous for minimizing truncation error during discretization. The residual convergence criteria were set at 10^{-3} and a monitor was set up to track the pressure drop, ensuring an adequate flow field solution. To make sure the accuracy of the results was not dependent on mesh fineness, a mesh refinement study was first conducted for both flow fields. The results and information of the mesh refinement study are displayed in Table 2.3.

Based on the results in Table 2.3, the lowest node quantity mesh achieved the desired accuracy while being independent of mesh fineness. Both simulations were used to generate streamline paths from the inlet to the outlet. Figures 2.4 and 2.5 show the effects on static pressure along streamlines.

Table 2.3: Mesh refinement results comparing flow fields.

Geometry	Nodes	Pressure Drop (psi)
1	254711	0.02822
	387282	0.02815
	566392	0.02810
2	265134	0.03312
	400987	0.03322
	569903	0.03320

Both flow fields were relatively smooth and irrotational, or laminar, matching the flow field characteristics of a similar study(40). Both geometries were successful in diffusing the electrolyte evenly through the cell. The largest pressure drop occurs across the cell, and Geometry 1 had 15% less pressure losses than Geometry 2. The increased flow performance of Geometry 1 coincided with the expected results that validated previous assumptions. Future designs will use the same principles to further optimize the flow efficiency.

Since the depth of Geometry 2 was twice that of Geometry 1, Geometry 2 had an increased ion path length. Electrochemical performance could be impacted by the residence time in the carbon felt. A higher residence time in the carbon felt coincides with a less efficient reaction(41). To quantify the electrochemical performance, the average residence time was calculated through each cell. A discrete number of massless particles were released at the inlet and tracked through the system until the exiting at the outlet. The Discrete Particle Model (DPM) module in ANSYS Fluent 18.2 was used to generate, track the particles, and calculate the average residence time in the cell. Particles in Geometry 1 spent 26% more time in the system than Geometry 2, indicating that it could have worse electrochemical performance. Geometry 1 did however have a lower pressure drop. Future computational fluid dynamics studies will explore the effects of different cell designs in which residence time is more of a factor.

2.6 Rapid Prototyping of Experimental Flow Cells

Design considerations for developing an efficient RFB include flow patterns in the reaction cell, electrode material, separator or membrane selection, pumping mechanics, and the ability to

manufacture the system. The flow field in the reaction cell should be designed to decrease energy losses and maximize charge transport.

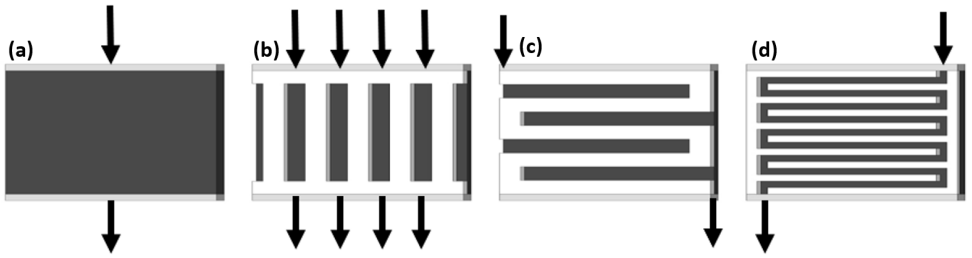

Figure 2.6: (a)Conventional (b)parallel (c)serpentine and (d)interdigitated flow channel designs are shown. The fluid moves from the top inlet to the bottom outlet.

Four main flow cell geometries are traditionally used: conventional, parallel, serpentine, and interdigitated. Figure 2.6 shows examples of these commonly discussed flow fields. Figure2.6(a) shows the conventional open design which features the electrolyte solution entering the reaction chamber completely filled with a porous electrode. Because the solution must move through the porous electrode, the conventional cell design suffers from a high pressure drop(41). Additionally, active species tend to suffer from uneven distribution across a conventional flow field. Whereas the conventional flow design forces the solution through the porous electrode for the entire chamber, the parallel (Figure2.6(b)), serpentine (Figure2.6(c)), and interdigitated (Figure2.6(d)) flow field designs feature the porous electrode elevated above a system of channels in the chamber. In the parallel design, the solution moves through multiple parallel channels from one side of the chamber to the other. As the solution moves, some of it circulates up into the porous electrode. While the pressure drop in this design is minimal, the parallel design suffers from poor electrolyte circulation within the chamber.

In the serpentine design the main channel snakes back and forth through the chamber. The electrolyte can flow through the channels or bypass the channel walls by going through the porous electrode. One of the main problems with the serpentine design is the large resonance time of the electrolyte solution in the porous electrode. Solution that bypasses the first wall tends to travel through the electrode until it reaches the exit, while fluid in the channel tends to remain in the

channel(41). As a result, the serpentine design also suffers from poor distribution.

Amongst the four designs, the interdigitated system fared the best in single-cell electrochemical testing. An interdigitated cell consists of dead-ended inlet channels interlocked with dead-ended outlet channels. For the solution to reach the outlet, it must cross over a channel wall and travel through the porous electrode. The interdigitated cell has a lower pressure drop than the serpentine cell and better distributes fresh electrolyte across the membrane(41). However, the interdigitated cell faces several challenges in multi-cell testing. Different permeabilities within each cell can cause the flow to be unevenly distributed across a stack of cells(2).

The porous electrode also contributes to the overall efficiency of the cell. In the selection of a porous electrode, there are four main factors to consider: active surface area, chemical stability, durability, and electrical conductivity(2). The active surface area of an electrode is inversely related to the electrode's permeability and porosity. While a greater surface area is generally favored from an electrochemical standpoint, this often conflicts with a decrease in permeability, an increase in the pressure drop, and an increase in pumping energy costs. The interaction of the solid with the electrolyte also influences the active surface area of an electrode. Electrodes with a poor wettability can cause air bubbles to form between the solution and the electrode, which would eliminate portions of the electrode surface area. Additionally, an electrode with a completely uniform porosity is most preferable, as that eliminates the formation of shunt currents in the cell. The electrical conductivity of the electrode is also important to consider, as any electrical resistance can lead to a decrease in the electrical efficiency of the cell. Currently, due to their high surface area, low cost, and electrical conductivity, carbon graphite felts are the most cost-feasible material for a porous electrode. In some tests, the carbon graphite felt is chemically treated to increase its surface conductivity.

The chamber depth of an RFB can also affect its efficiency. Decreasing the chamber depth decreases the average distance the ions must travel to the membrane. This in turn decreases the physical and electrochemical resistance of the system. A shorter path length, from inlet to outlet, also allows for more of the electrolyte solution to react, which increases the efficiency. In addition

to the physical cell design, the flow rate and concentration also affects the efficiency of the RFB cell. One area of concern for liquid RFBs is the development of shunt currents, in which the fluid deviates from its desired path. However, a greater flow rate must also be balanced with minimizing energy losses from pumping. According to Weber, an average velocity of 3.9 cm/s through the reaction chamber yields the greatest voltage(2). Tang et al. proposed that a variable flow rate could increase the efficiency of the RFB(42).

The first prototype cell featured an open space design concept. In this design, the main inlet and outlet channels were designed with two Y-splits to ensure proper flow distribution. This resulted in four inlets and outlets of the reaction chamber that have equal flow rates. Testing was conducted using running water to ensure proper flow distribution through the chamber. Results are shown in Table 2.4.

Table 2.4: Flow distribution efficiency of two reaction chamber designs that incorporate Y-splits to evenly distribute solution into the reaction chamber.

Flow Rate (mL/min)	**Design P5Y** Efficiency (%)	**Design P4-3** Efficiency (%)
10	98	97
7	95	88
5	93	87
3	98	89

With a successful inlet and outlet design, the reaction chamber, plumbing, storage tanks, seals and other components were determined to design a RFB system that could be inexpensively built with evenly distributed flow of solution through the cell. It is critical to maintain a completely inert environment within the entire system. This prevents the RFB compounds from reacting with oxygen or moisture in the air. A prototype experimental system was fabricated and tested using water as the solution, to check for leaks. The successful water tests led to an inexpensive combination of ferrocene and methyl-viologen to be ran through the system as a baseline model. Once the electrolyte entered the reaction chamber, it traveled through a graphite felt electrode until it reached the outlet. The main goal of the initial prototype was solely to prove the development of a 3D-printed cell system prototype was possible and to use it as a starting point for further

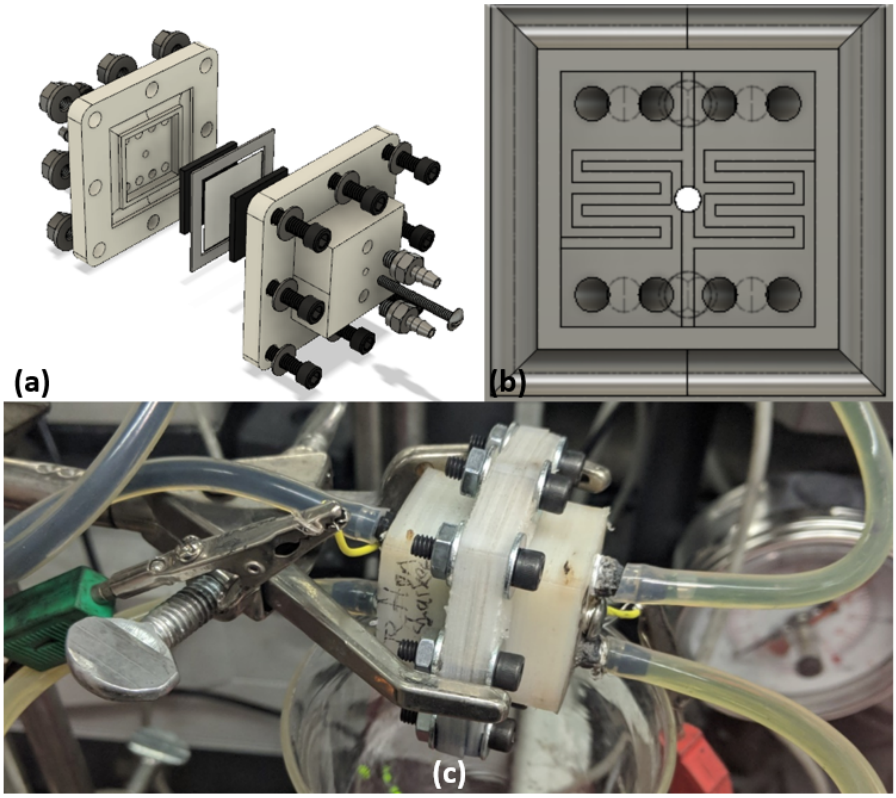

Figure 2.7: A 3D model was developed to successfully fabricate and test an interdigitated flow field: an exploded view showing an RFB cell and its corresponding components(a), an interdigitated flow field(b), and the operational prototype cell(c).

system development. The open space prototype (Geometry 1 and 2) had a large chamber depth which led to inefficiencies (due to the long path for the ions to travel). Additionally, stainless-steel electrodes were selected to prevent oxidation which resulted in poor conductivity. Any premature oxidation within the system would negatively influence the chemical reaction within the chamber. A potentiostat was connected to the graphite felt with the stainless-steel electrodes. Using 3D printing techniques, other cell architectures and flow field geometries could be studied relatively quickly. Figure 2.7 shows an example of this technique with a model being fabricated and tested quickly. The interdigitated flow field geometry will be studied in more detail in future work.

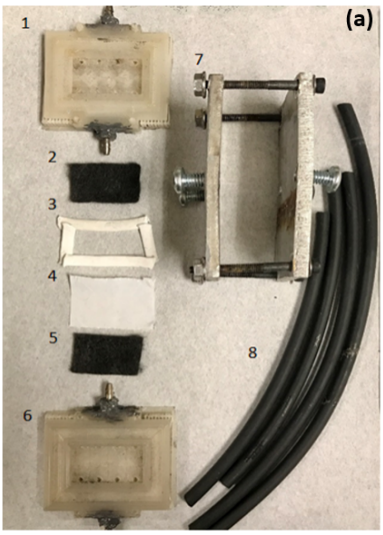

Item	Description
1,6	Nylon 3D Printed Reaction Chamber
2,5	Graphite Felt
3	PTFE Gasket
4	Microporous Simple Separator
7	Clamping Mechanism
8	Fluro elastomer Tubing

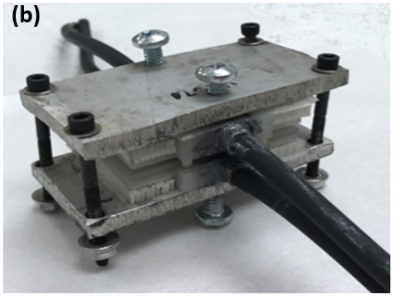

Figure 2.8: 3D printed cell with its associated components(a) and a fully assembled cell(b).

2.7 Electrochemical Experimental Results

Figure 2.8(a) shows the 3D printed flow disassembled and its internal components with the fully assembled cell is shown in Figure 2.9(b). Figure 2.8 shows an inexpensive test station prototype. A potential step is applied to the electrode and the resulting current is measured and recorded over a period. The method can be applied to both a single or double potential step. Figure 2.10 and Figure 2.11 show the results from a model solution of ferrocene and methyl-viologen being used to test charging and discharging capabilities, solution movement, and system design. A 1.2 V charging potential was applied while 50 mL of solution was cycled at a flow rate of 1 mL/min. The resulting current was measured. The initial drop in current over the first 200 seconds can be attributed to initial conditioning of the felt and membrane. The solution must fully saturate the internal components before a consistent reaction can occur.

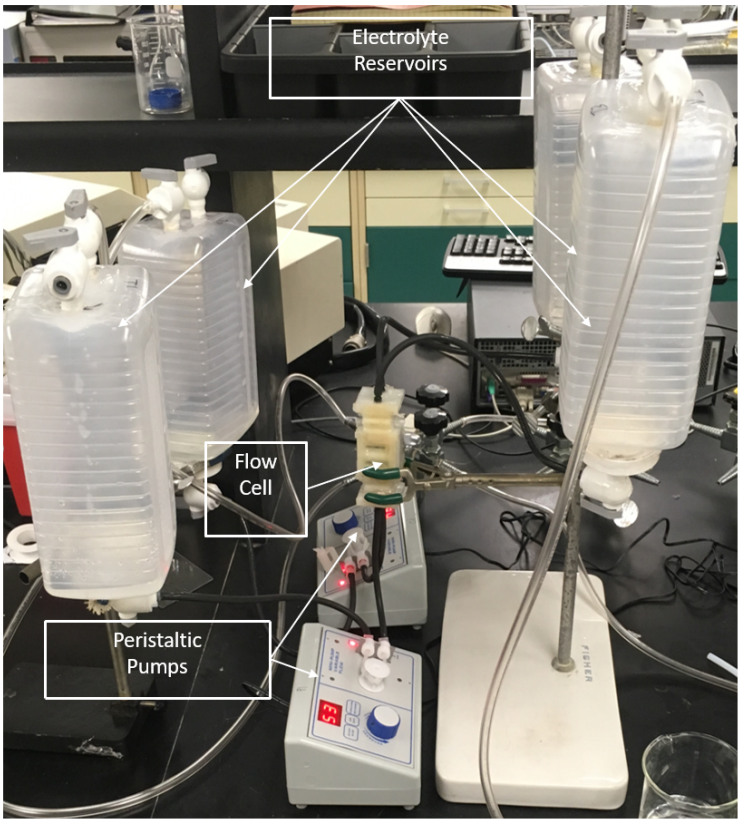

Figure 2.9: Initial test station with reservoirs, plumbing, a peristaltic pump, and a 3D printed flow cell.

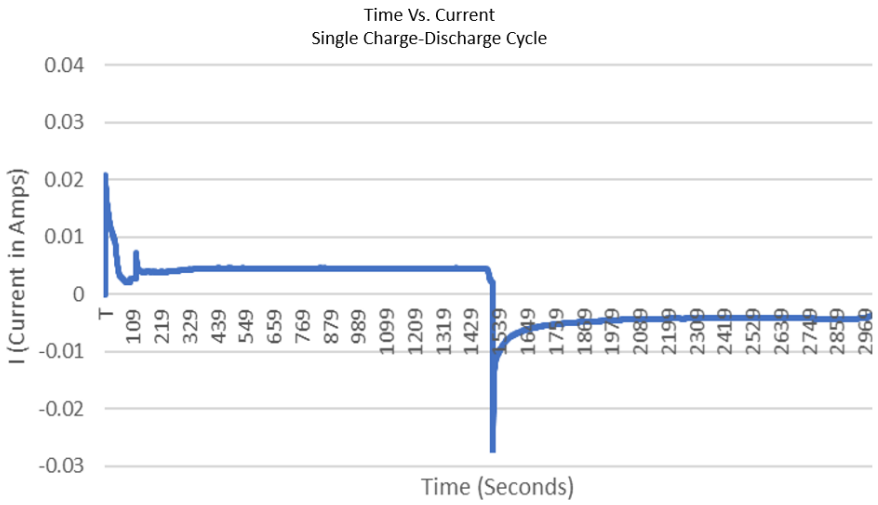

Figure 2.10: Measured current (mA) during a constant voltage charge-discharge cycle with a 3D printed cell and microporous separator.

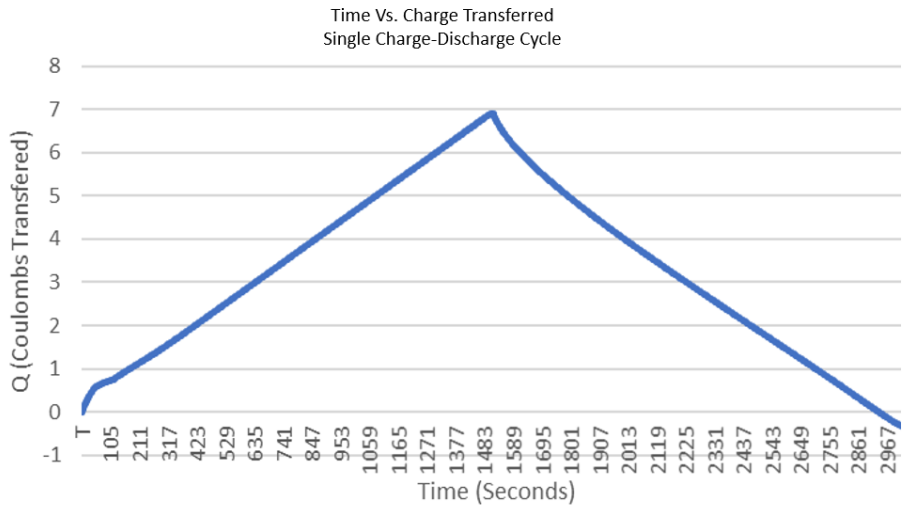

Figure 2.11: Measured charge (coulombs) during a constant voltage charge-discharge cycle with a 3D printed cell and microporous separator.

2.8 Conclusion

Design and testing of an early RFB that does not require an ion-selective membrane system is discussed in the above text. The proposed chemistry utilizes two-electron organic compounds that have the same half reaction products; which leads to increased current density compared to typical RFBs and the elimination of the expensive ion-selective membrane. The compounds discussed in this paper also have no known toxicity and are less expensive due to their linked, multi-electron structure. Several milestones were met including:

- an inexpensive flow cell was designed and manufactured using a benchtop 3D printer;
- an inexpensive test station was built;
- a techno-economic analysis was performed;
- CFD was used to ensure that the design of the flow chamber would provide a uniform distribution of active species;
- and cycling of a symmetric RFB was demonstrated using a microporous separator rather than an ion-selective membrane.

The novel redox couple was successfully cycled in this inexpensive system using a microporous separator rather than an ion-selective membrane. This acted as a proof of concept and encouraged future work developing symmetric RFBs as a viable form of grid-scale energy storage.

CHAPTER 3

DEMONSTRATION OF A LINKED ANOLYTE-CATHOLYTE SYSTEM FOR NONAQUEOUS ORGANIC REDOX FLOW BATTERIES

3.1 Introduction

Redox flow batteries are plagued with permanent capacity fade, associated in part with crossover of unwanted species. A possible solution consists of using a single molecule, in different redox states, as both the anolyte and catholyte. The redox couple shown in Figure 3.1 phenothiazine 5,5-dioxide system covalently linked via a propyl chain to 4-acetylpyridinum (called *PDO-L-AP* for brevity) displays an open circuit potential of 2.12V and was evaluated for demonstration purposes through static cycling experiments with a porous separator. Although the linked compound displays limited durability in the charged state, this study demonstrates the viability of a linked redox couple using a simple microporous separator rather than an ion-selective membrane. It was known that Acetylpyridinium anolytes have previously shown irreversible capacity loss when cycled(43).

RFBs are considered as potentially inexpensive, safe, easily deployable energy storage systems. In an RFB, a solution containing a charge-balancing electrolyte mixed with an electroactive redox couple is stored in reservoirs until pumps are used to flow the solution through an electrochemical cell where energy can be released(2; 7; 44; 45; 31). Contrary to secondary rechargeable cells, the active materials are entirely dissolved in solution and referred to as the anolyte and catholyte. The anolyte and catholyte solutions flow through porous electrodes in contact with current collectors. The flow constantly replenishes active species near the electrode surface, resulting in a continuous reaction. An ion-selective membrane is typically placed between the half-cells to eliminate any electrical shorts and to prevent crossover of unwanted species. Two of the most significant challenges while developing RFBs as a form of long-duration, grid-scale energy storage technology are their high cost and permanent capacity loss caused by crossover(7; 46; 47; 48; 27). Ion-selective membranes are crucial components that prevent crossover and act as a medium for the transport

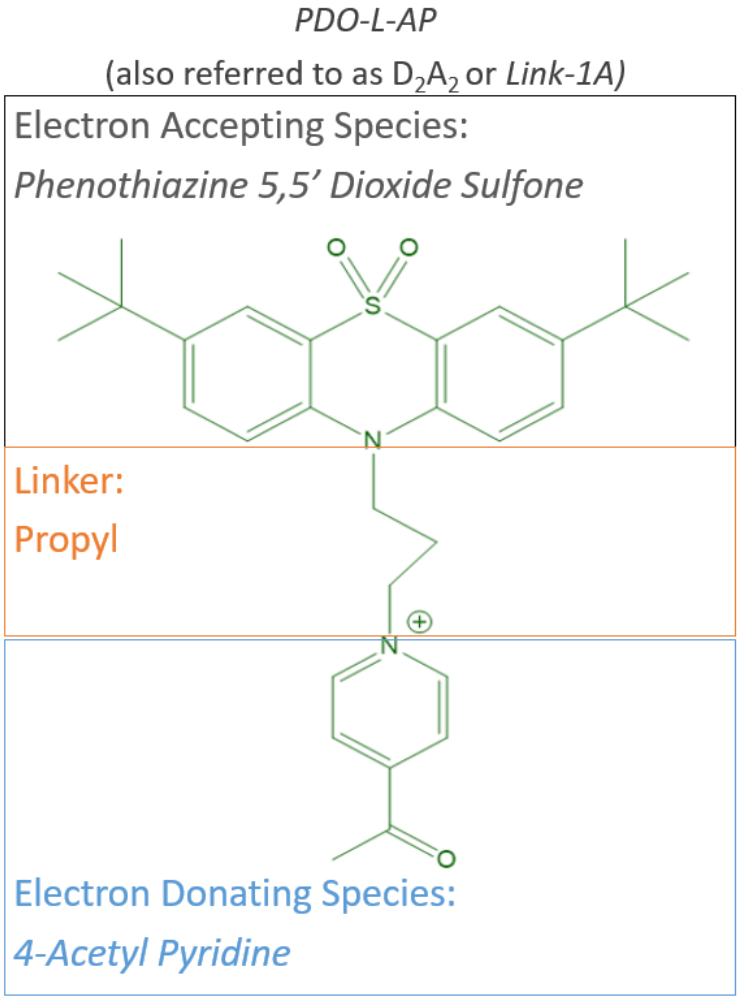

Figure 3.1: Molecular structure of the covalently linked redox couple *PDO-L-AP*. It was chosen for demonstration purposes because of it was inexpensive and had a relatively simple synthesis procedure.

of charge balancing ions. Membranes, however, are expensive, require routine maintenance, and do not completely prevent crossover. In a typical RFB, if unwanted species pass through the membrane, they cannot be recovered or used in future cycles without an expensive step of external rebalancing or electrolyte purification.

To address issues caused by crossover, the membrane technology or the chemical species can be modified. Developing novel membranes and separators can reduce the amount of crossover that occurs, but alterations may negatively affect the performance by increasing internal cell

resistance(49; 50; 51; 52; 53; 54; 55). Instead, a simple approach to modify the chemical species was used. It consists of linking the anolyte and catholyte together in a single molecule. This has been proposed as a means to minimize the threat of crossover-induced capacity fade(2; 27; 56; 28). In this way, the same compound in different oxidation states is used as both the anolyte and catholyte(57). This approach has the additional benefit of allowing replacement of the ion-selective membrane with an inexpensive microporous separator. The improved permeability to ionic flow likely reduces internal resistance(58).

In this study, *PDO-L-AP* is employed as a prototype linked molecule that can operate as both the anolyte and catholyte in an RFB. Although acetylpyridinium anolytes are known to undergo irreversible capacity loss during cycling, this easily synthesized system was chosen for this proof-of-concept investigation(43). Equations 3.1 and 3.2 show reversible electrochemical half-reactions involving the "linked" *PDO-L-AP* compound used in this study during battery discharge.

$$Linked\ Catholyte: PDO^{+} - L - AP + e^{-} <=> PDO - L - AP \tag{3.1}$$

$$Linked\ Anolyte: PDO - L - AP^{-} <=> PDO - L - AP + e^{-} \tag{3.2}$$

Note that the half-reactions at each electrode result in the same product labeled *PDO-L-AP*. Crossover may still occur, but will only cause a slight decrease in coulombic efficiency rather than permanent capacity loss, as the next charge cycle will result in a full restoration of capacity. Attempts at implementing this approach have produced numerous linked catholyte/anolyte active materials capable of a net one-electron ($1e^{-}$) operation, as well as several doubly linked systems capable of a net two-electron ($2e^{-}$) operation, wherein an anolyte moiety having a $2e^{-}$ redox couple is linked to two $1e^{-}$ catholyte moieties(57). A large variety of organic and inorganic compounds can be specifically tailored for the electrochemical demands of the intended RFB(27; 37; 59; 38; 60; 61; 62; 63; 64; 65; 36). In the current study, a series of electrochemical experiments were performed to evaluate chemical stability and to explore the effects of crossover-induced capacity fade of the *PDO-L-AP* compound. Synthesis of this compound is briefly discussed, followed by results of electrochemical experiments evaluating performance using both propylene carbonate

(PC) and acetonitrile (ACN) electrolyte solutions, finally experiments with flow are performed and results are analyzed.

3.2 Experimental

Previously reported results have shown that various carbazole, phenothiazine, and phenothiazine 5,5-dioxide derivatives can be prepared as electron donating groups which possess high oxidation potentials, robust electrochemical stability, and suitable solubilities in nonaqueous solvents(36). Furthermore, pyridinium and extended viologen derivatives have been evaluated as electron accepting anolyte materials capable of undergoing highly reversible reductions at low potentials. More specifically, the phenothiazine 5,5-dioxide system covalently linked via a propyl chain to 4-acetylpyridinum has been shown to undergo electrochemically reversible net one-electron reduction and oxidation reactions(36; 57). Figure 3.2 shows each of the oxidation states of *PDO-L-AP* that are produced while cycling the flow battery.

PDO-L-AP was investigated as a demonstrator of the linked approach using electrochemical techniques including Cyclic Voltammetry (CV), Chronoamperometry (CA), and Cyclic Charge-Discharge (CCD) experiments. PC was chosen as the solvent in this study for its safety and the relatively high solubility of the active species involved, while ACN was considered for its high ionic conductivity. Tetraethylammonium tetrafluoroborate ($TEABF_4$) was used as the charge balancing supporting electrolyte in both cases due to its relatively high solubility in both PC and ACN. These measurements are summarized in Table A.1. Stability, coulombic efficiency, and other performance benchmarks were analyzed while repeatedly charging and discharging of the cell using a constant current.

Cyclic charge-discharge experiments were performed to demonstrate reversibility, stability, and general performance of *PDO-L-AP* in an RFB. Two separate solutions were prepared containing 100 mM *PDO-L-AP* and 1.0 M $TEABF_4$ in both ACN and PC. Figure 3.3(a) shows the experimental setup within an inert environment provided by a VAC Omnilab glovebox containing high purity argon. This was necessary to remove contaminants, moisture, and oxygen. Electrochemical

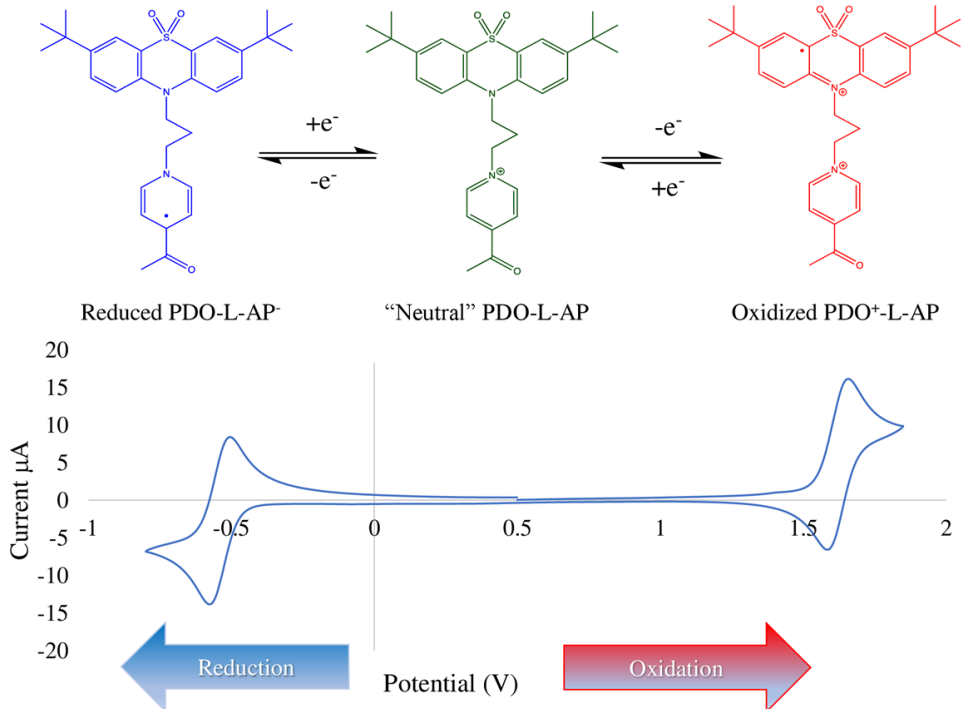

Figure 3.2: *PDO-L-AP* in each of its three oxidation states during charging and discharging of the flow battery. Cyclic voltammetry of *PDO-L-AP* performed in propylene carbonate/0.2M $TEABF_4$ using a Pt disc working electrode, a Pt/Ti wire anode, and an Ag wire as a pseudo reference electrode, at a scan rate of 100 mV/s.

experiments were controlled using a Gamry 3000 potentiostat in a two-electrode configuration. A New Era Pump Systems' NE-4000 2-channel syringe pump and gas tight glass syringes were used for symmetric cycling. A Scribner RFB test fixture with a $25cm^2$ serpentine flow field was used with an opened cell shown in Figure 3.3(b). Results from initial viscosity and solubility are shown in Appendix A.1.1 which aided in the selection solvent and charge balancing electrolyte.

Based on the size of the flow field, concentration of the active species, and estimated volume of solution contained within the porous graphite felt, a theoretical capacity can be calculated. For the static experiments performed in both ACN and PC an estimated capacity of roughly 19 milliamp hours (mAh) was expected. For the additional flow experiments, studying *PDO-L-AP* in PC, a larger volume of solution was used so the expected capacity was about 40 mAh. It should be noted that this would be attained only if 100% of the active material in the cell was converted in a single charge cycle, which is unlikely in this experiment. In order to ensure a complete fill, a minimal

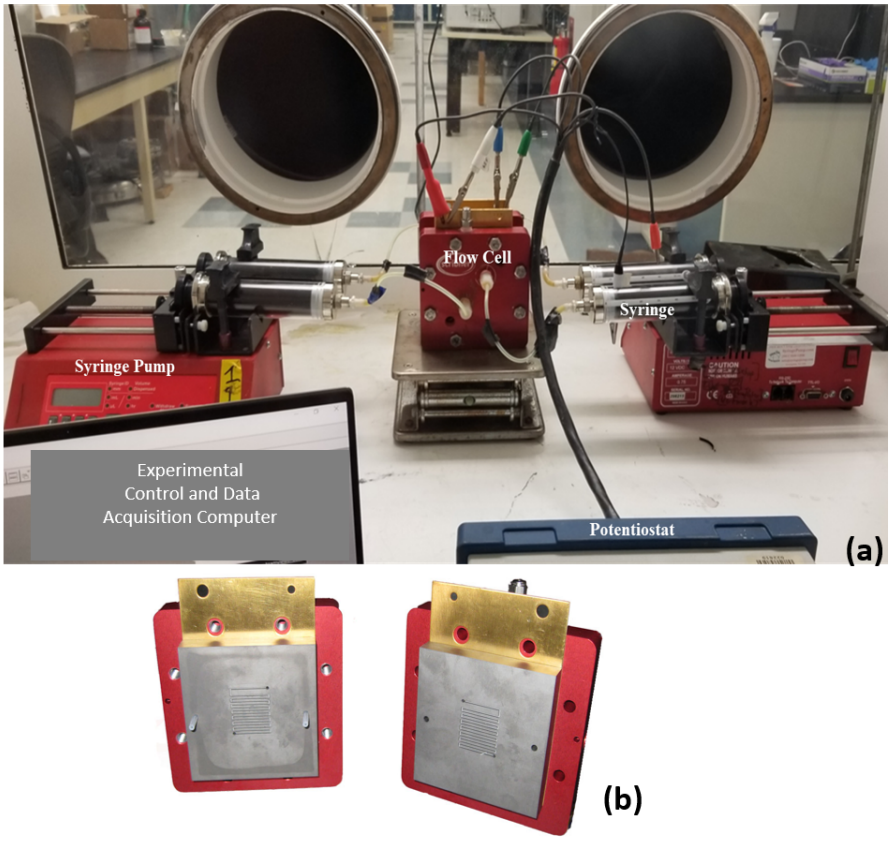

Figure 3.3: Flow cell experimental setup showing the dual syringe pumps, potentiostat, gas-tight glass syringes, and flow cell.

amount of solution was slowly added to remove gas trapped in the cell. Once the solution filled the cell and protruding plumbing, the tube was capped with the opposing syringe and locked into place.

Flow studies were performed to investigate how operating parameters alter the average current, charge capacity, and coulombic efficiency. Charging voltage and flow rate were varied and a single charge-discharge was performed to study the impact of each operating parameter. The syringe pumps were programmed to continuously cycle the solution many times back and forth to see if the conversion of active species could be improved(66; 67; 68). Earlier work saw conversion of less than 1% of the active material.

3.3 Results and Discussion

Cycling of *PDO-L-AP* on each side of the reaction chamber in a symmetric flow cell was conducted in static and flow conditions. Static experiments were performed to eliminate as many variables as possible. The results could act as a baseline to compare results from flow experiments. Flow experiments could be used to not only practically demonstrate the novel redox couple, but also to direct operational parameters in future experiments.

3.3.1 Static Cycling and Cyclic Voltammetry

Cyclic voltammetry of *PDO-L-AP* reveals a reversible one-electron reduction of the 4-acetylpyridnium moiety at -0.81 V and a reversible one-electron oxidation of the phenothiazine 5,5-dioxide constituent at 1.31 V. This suggests that an RFB with *PDO-L-AP* as the active species will display an open circuit cell potential of approximately 2.12 V, shown in Figure 3.2. An overpotential of 0.28 V was applied to overcome internal losses and activation barriers, resulting in a charging potential of 2.4 V. Initially both solutions were charged using CA. A constant voltage of 2.4 V was applied for 300 seconds while charging and 0 V while discharging. This was done to observe initial capacity and to determine a reasonable value for the charging and discharging current. For the ACN solution, an initial current of 2 A with final current of 93 mA were observed. Much lower currents were observed when testing the PC solution with an initial current of 87 mA and a final current of 24 mA. The values for charging and discharging with a constant current were chosen conservatively based on these results. Charging and discharging was thus conducted for 100 cycles at 50 mA and 20 mA for another 100 cycles in ACN. For PC, values of 20 mA and 10 mA were used.

Results from static charge-discharge cycling are shown in Figures 3.4 and 3.5. The ACN solution showed higher current in the CA experiments and a higher capacity in CCD experiments when compared to the experiments performed with the PC solution. This can be attributed to ACN being less viscous and having a higher ionic conductivity. A coulombic efficiency greater than

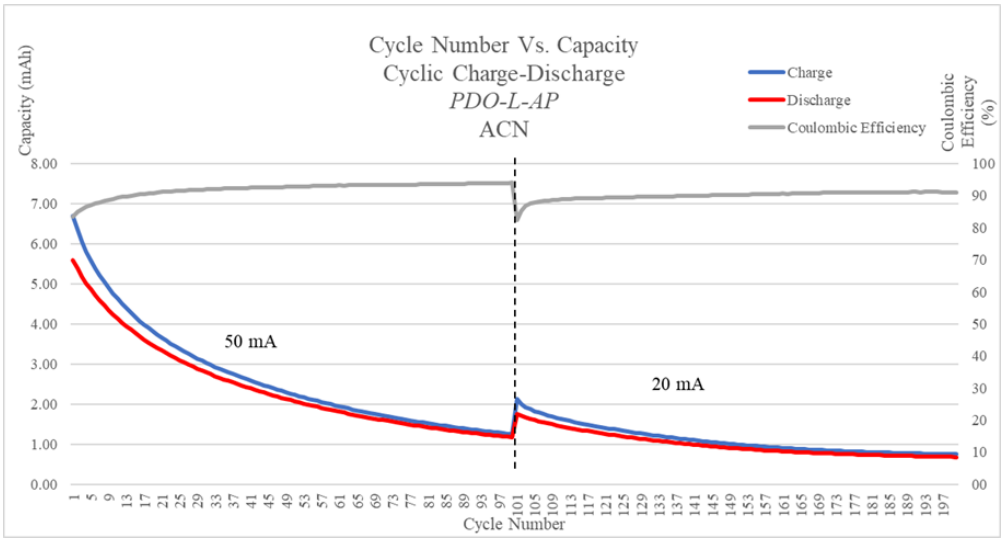

Figure 3.4: Cyclic charge-discharge experiments over 200 cycles using a current of 50 mA over the first 100 cycles, followed by 20 mA from cycle 101 to cycle 201.

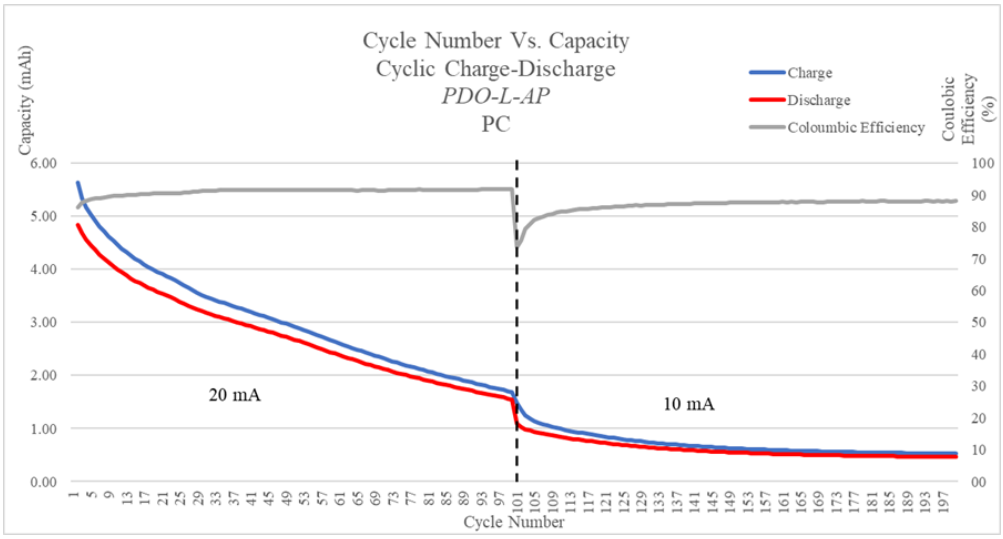

Figure 3.5: Cyclic charge-discharge experiments over 200 cycles while using a current of 20 mA over the first 100 cycles, followed by 10 mA from cycle 101 to cycle 201.

90% was maintained throughout both series of experiments. Poor coulombic efficiencies would be expected while using a microporous separator. This is because removing the selective membrane enables active species to crossover more easily due to its increased porosity. This demonstrates the viability of using a linked chemistry and a microporous separator in flow batteries. For both solutions, the capacity decayed by around 80% after 200 cycles. A final charge capacity of 1.3 mAh

was measured for the ACN solution and 1.7 mAh for the PC solution. Although initially at a higher capacity, the *PDO-L-AP* in ACN retained less capacity after 100 cycles than that of the *PDO-L-AP* in PC. This suggests that capacity fade is more rapid at higher charging currents. The permanent capacity fade is thought to be attributed to diffusion of charged species out of reaction chamber, reaction with impurities in the supporting electrolyte, and degradation of the active material itself (primarily the anolyte portion).

3.3.2 Flow Cycling and Operating Parameter Analysis

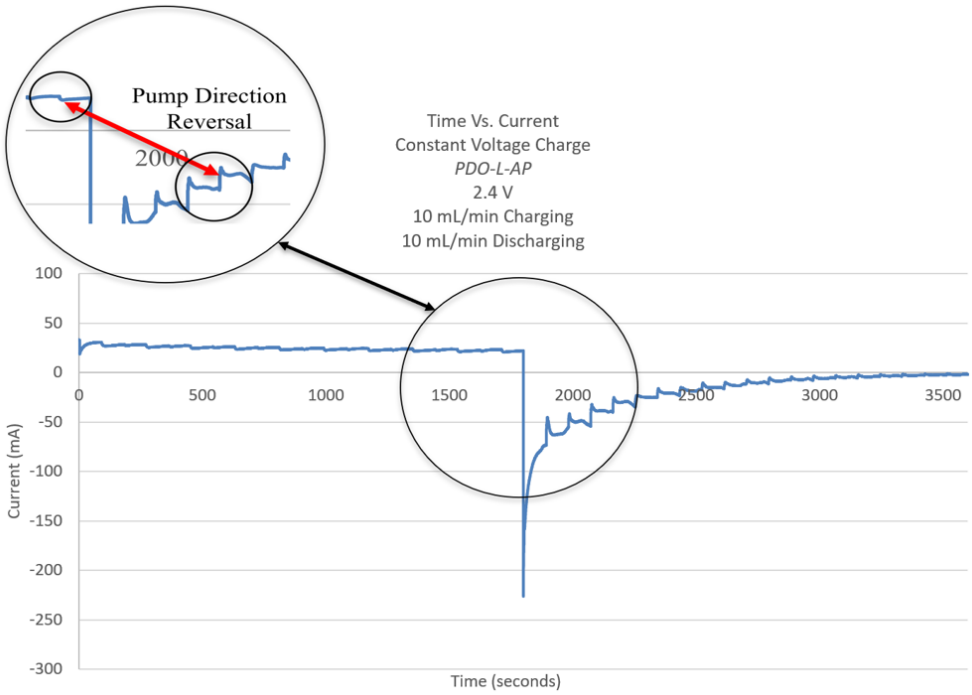

Figure 3.6: Results from single recirculated constant 2.4 V charge-discharge cycle with equivalent flow rates. When the pumps change directions the solution momentarily stalls causing a rapid decrease in current.

Flow analysis was performed using the syringe pumps to control solution flow and a potentiostat to apply a constant voltage while measuring current shown in Figure 3.3. Flow rate (mL/min) and operating voltage (V) were altered independently to gauge their impact on the average current measured (mA), charge capacity (mAh), and coulombic efficiency (%). The results from an

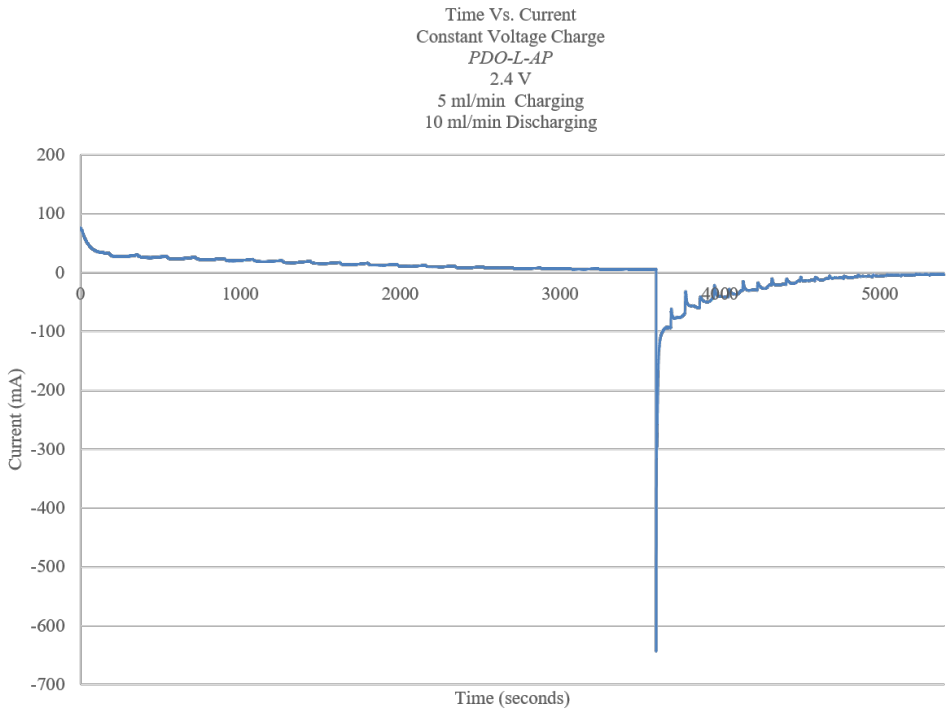

Figure 3.7: Single recirculated constant 2.4 V charge-discharge cycle with a charging flow rate (5 mL/min) that is half the value used while discharging (10 mL/min).

experiment with a charging voltage of 2.4 V with equivalent flow is shown in Figure 3.6. To study the differences in charging and discharging reaction kinetics, the pumping flow rate was set to 5 mL/min while charging and maintained at 10 mL/min while discharging. The results are shown in Figure 3.7. The charging voltage was increased to 2.45 V and 2.5 V while maintain equivalent flow rates of 10 mL/min, shown in Figures 3.8 and 3.9. This was to see if the current and capacity could be increased as the true overpotential was unclear.

Results are summarized in Table 3.1. Since the supply of active material for these experiments was limited, applying a constant current was seen as a risk when flowing. If there is a slight deviation in the supply of active species to the electrode surface, sudden jumps in the potential can occur. When this is measured by the potentiostat, the cycle can be prematurely ended. This risks the potentiostat measuring the voltage after the active species reach an unstable oxidation state and decompose. This is because the redox couple is only stable within a certain voltage range determined using cyclic voltammetry. This value does not include overpotential required to

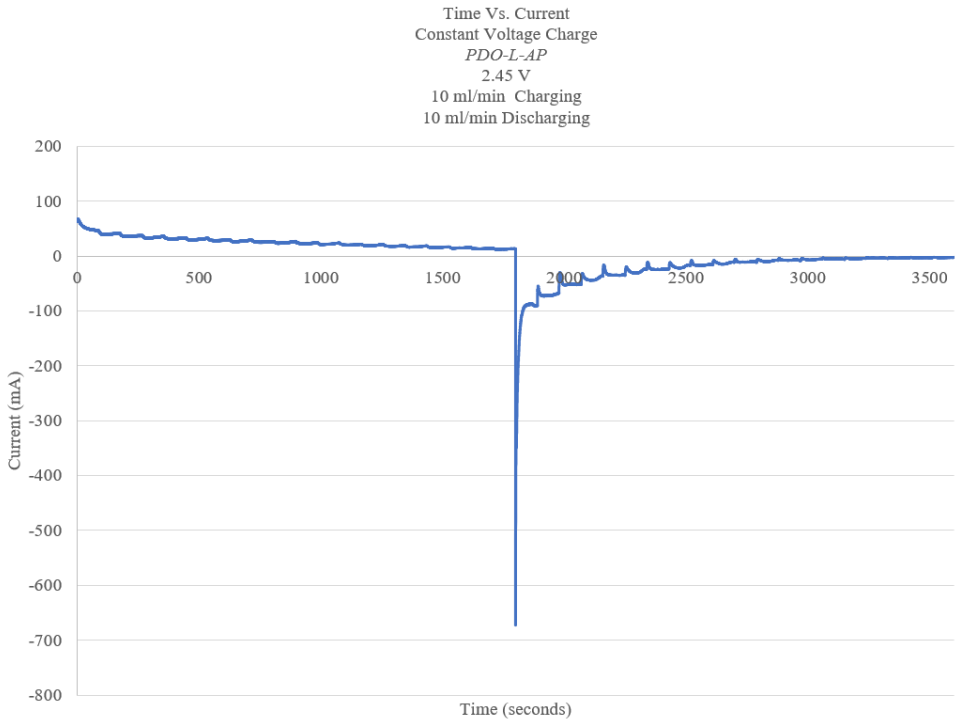

Figure 3.8: Single recirculated constant 2.45 V charge-charge cycle with equivalent flow rates.

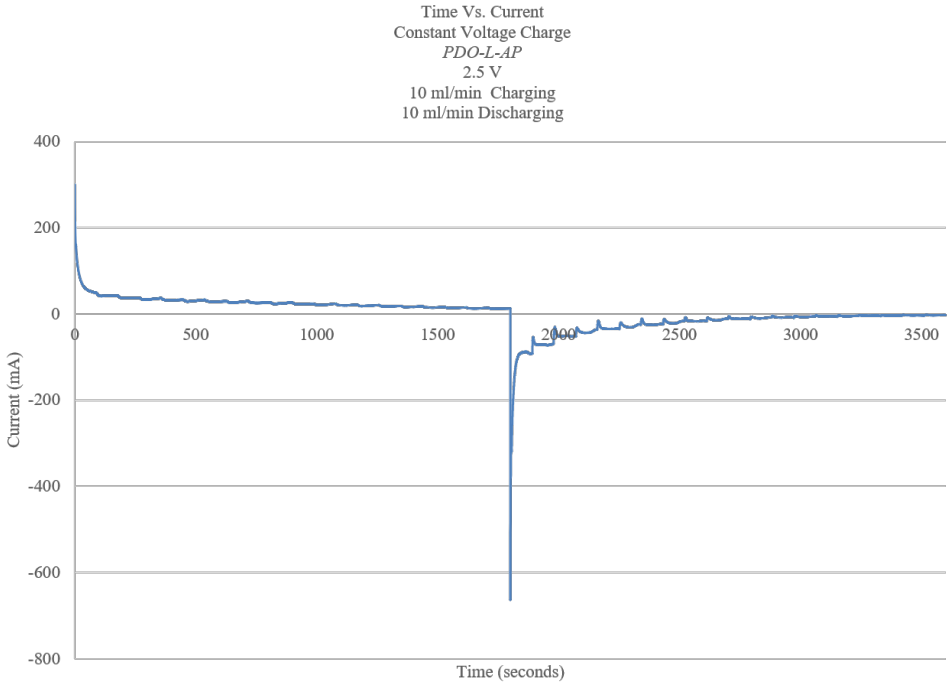

Figure 3.9: Single recirculated constant 2.5 V charge-discharge cycle with equivalent flow rates.

overcome activation barriers. This has to be estimated or quantitatively determined using advanced impedance techniques. The pumps were programmed to constantly recirculate solution regardless of whether the system was charging or discharging. When the pump switches directions, the solution momentarily stalls. The graphic in Figure 3.6 highlights rapid decreases in current during both charging and discharging as the syringe pump switches directions. This can be attributed to the active species being rapidly exhausted until the resulting flow returns fresh solution to the electrodes' surface. A more dynamic control system would be required to respond to instantaneous fluctuations in current and voltage that are caused by fluid dynamics within the cell.

The results shown in Figure 3.6 indicated that the charging kinetics were slower than discharging, which resulted in poor coulombic efficiency. To compensate for this imbalance, the charging flow rate was reduced to 5 mL/min while discharging flow rate was maintained at 10 mL/min. This improved the coulombic efficiency by 6% and the charging capacity by 2 mAh. The average current did decrease by 2 mA due to the slower flow rate. The charging potential was increased by 0.5 V, to 2.45 V. This increased the average current by 3 mA, but decreased the charge capacity by 1 mAh and the coulombic efficiency by 2%. Although 2.4 V seemed to be the ideal charging voltage, it was then increased to 2.5 V to further study and strain the stability of the linked redox couple. As hypothesized, the coulombic efficiency suffered and decreased to 87%. The average current and charge capacity did however increase slightly.

Table 3.1: Symmetric flow cell cycling results comparing average current, capacity while charging, and coulombic efficiency while varying charging potential and flow rate.

Charging Potential (V)	**Flow Rate** (mL/min)	**Average Current** (mA)	**Charging Capacity** (mAh)	**Coulombic Efficiency** (%)
2.4	10	23	12	88
2.4	C:5/DC:10	21	14	94
2.45	10	24	13	92
2.5	10	25	14	87

3.4 Conclusions

Permanent crossover-induced capacity fade decreases the operating capacity of typical RFBs. The phenothiazine 5,5-dioxide system covalently linked via a propyl chain to 4-acetylpyridinum, named *PDO-L-AP*, shows promise in demonstrating the use of a covalently linked anolyte-catholyte redox couple in an RFB. This strategy could be a viable approach to both eliminate the need for an ion-selective membrane and mitigate the impact of crossover in RFBs. The linked organic redox couple was observed to:

- demonstrate the viability of a symmetric flow cell with a microporous separator;
- operate at high currents when dissolved in ACN;
- retain more capacity when charging at lower rates;
- maintain high coulombic efficiency throughout the experiments;

Flow was introduced, showing that:

- recirculation of the solution improved the material conversion rate to more than 30% from less than 1% in previous flow experiments;
- charging and discharging electrochemical kinetics have different reaction rates;
- a variable flow rate could improve coulombic efficiency and charge capacity;
- increasing the charging voltage above 2.4 V resulted in poor coulombic efficiency.

CHAPTER 4

IDENTIFYING AND QUANTIFYING LOSSES IN A MEMBRANELESS, NONAQUEOUS, ORGANIC REDOX FLOW BATTERY USING ELECTROCHEMICAL IMPEDANCE SPECTROSCOPY

4.1 Introduction

When developing an RFB, each component selection and the system design process impacts its electrochemical performance. Analysis of these impacts, within a nonaqueous organic redox flow battery, is discussed. Electrochemical impedance spectroscopy is used to determining an exact overpotential necessary to overcome internal losses within the cell. Specifically comparing the impact that replacing the ion-selective membrane with a microporous separator has on the losses within an RFB. Other design considerations associated with redox couple synthesis, solvents, supporting electrolyte, flow field geometry, reaction chamber design, porous electrode, and current collectors are reviewed.

Experimental results support the hypothesis that internal resistance decreases in a redox flow battery when a microporous separator replaces an ion-selective membrane as a medium for ion transport. When compared, lumped cell resistance decreased by a factor of three. The experimental procedure, data analysis techniques, and results described could direct future studies. Understanding how specific components, materials, geometry, and flow phenomena affect performance is critical to develop an inexpensive yet efficient redox flow battery.

RFBs are under consideration as a deployable, safe, and efficient electrochemical energy storage device. One of the most significant challenges facing long-duration, grid-scale energy storage technology is cost(31). Ion-selective membranes are a crucial component because they prevent crossover and act as a medium for the transport of charge balancing ions; however, they are expensive, require maintenance, and decrease the efficiency of the system over time. If the threat of crossover induced capacity fade is mitigated, internal resistance could be reduced by replacing the ion-selective membrane with a microporous separator. High resistance is prevalent across the

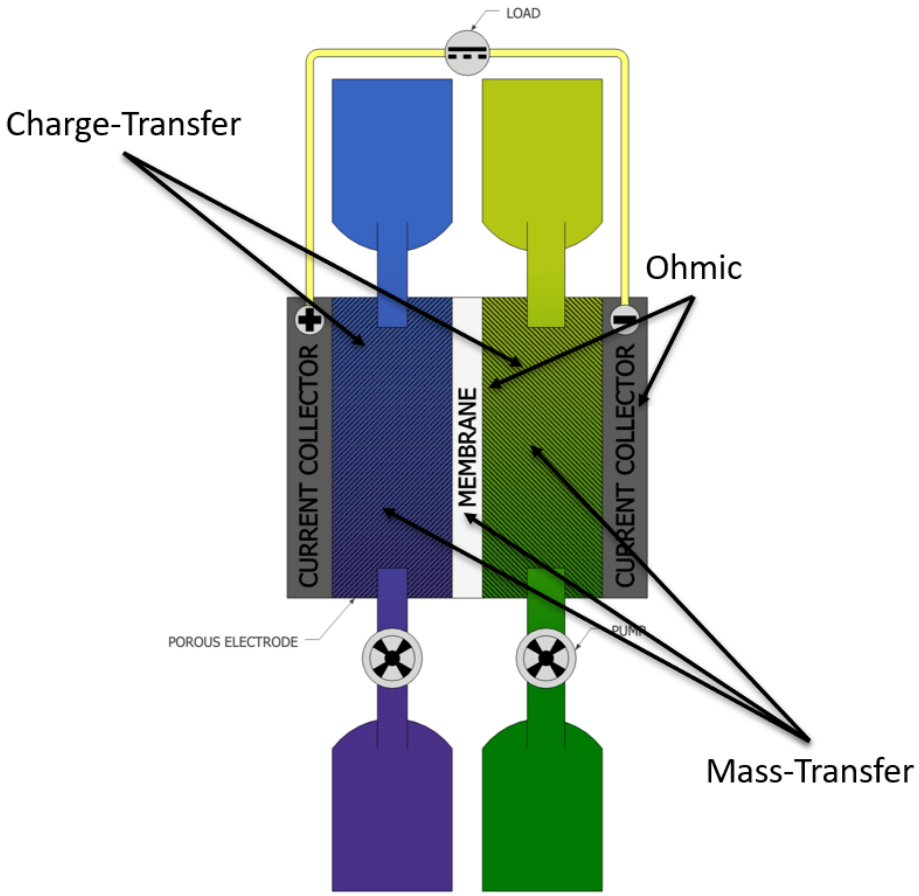

Figure 4.1: Diagram of an RFB that includes the current collector, porous electrode, membrane (separator for proposed linked chemistry), pumps, and the tanks. Several types of losses exist within an RFB and can be associated with different components including ohmic, mass-transfer, and charge-transfer losses.

interface between the membrane and the porous electrode. Figure 4.1 shows where specific types of losses, specifically charge-transfer, and mass-transfer, exist within an RFB(69).

Contrary to typical secondary rechargeable cells, the reactants of a flow battery are dissolved within a solution also containing charge-balancing supporting electrolyte. For example, typical rechargeable li-ion batteries consist of a solid anode and cathode separated by a liquid solvent containing supporting electrolyte. RFBs differ because they operate similarly to a combination of a fuel cell and an electrolyzer(7). The design and size of the cell, electrode, storage reservoirs and other components must reflect any change in the power or energy capacity. RFBs offer greater flexibility when designing a system that mitigates internal losses because components related to

power production can be altered independently of energy capacity components.

Equivalent series resistance in a li-ion cell can be categorized into three segments including interfacial resistance in the electrode or current collector, ionic resistance in the solution, and impedance in in the electrode's structural design. RFBs share these but also include losses from the supply of electroactive species to the electrode surface, crossover of unwanted species, and ohmic resistance associated with an increased ionic path length from RFBs' requiring larger overall cell size is required to house components(70; 71; 72; 73; 48). Advection, in partnership with diffusion and migration, is a key transport mechanism in RFBs. Due to this, performance is dependent on the fluid dynamics within the cell. Altering the flow field geometry and pumping parameters adds flexibility while developing an RFB that other forms of energy storage do not have.

Permanent capacity fade caused by crossover of electroactive species is a major challenge facing researchers(73; 74; 46; 75; 76). A solution circulates through a reaction chamber that enables energy to be stored or released as it flows across a membrane. The membrane mediates the electrochemical reaction by allowing charge balancing ions to pass through while preventing oppositely charged species from crossing over. Unless recovered, the presence of unwanted species causes the capacity to fade over time and chemical decomposition of the redox couples.

This study aims to investigate impedance techniques as a method which could be used to improve RFBs performance and longevity. This was carried out by performing a literature review of how RFB components impact losses, discussing how EIS has been used to study RFBs, determining how to interpret results from EIS studies, and specifically comparing the internal resistance associated with an ion-selective membrane to that of a microporous separator.

4.2 Redox Flow Battery Components' Impact on Internal Losses

Design considerations impact ohmic, charge-transfer, and mass-transfer losses within an RFB. Ohmic resistance (sometimes referred to as surface resistance) is associated with the physical distance charged species have to travel(77; 78). Charge-transfer limitations are the result of sluggish kinetics at the electrode(79). Kinetics are directly affected by characteristics of the electroactive

species, solvent, and supporting electrolyte. Ohmic losses are associated with the current collector, cell architecture, porous electrode, and membrane. Mass-transfer losses stem from an inadequate delivery of species to the electrode surface. Flow field design, species concentration, diffusion coefficients, and electrolyte velocity are characteristics that affect mass-transfer losses.

The linked redox couple that was previously discussed has the potential to increase energy density and coulombic efficiency, while decreasing system cost and internal resistance. This could allow RFBs to become a cost-competitive form of grid-scale energy storage. Trade-offs may have to be made while developing the most cost-effective, yet efficient, system possible. Tables 4.1, 4.2, and 4.3 categorize losses associated with specific components of an RFB as ohmic, charge-transfer, mass-transfer losses(80).

Table 4.1: Components associated with ohmic resistance within an RFB.

Ohmic (R_{oh})
Reaction Chamber
Current Collector
Porous Electrode Surface Area
Membrane

Table 4.2: Components associated with charge-transfer resistance within an RFB.

Charge-Transfer (R_{CT})
Sluggish Kinetics at the Electrode's Surface
Redox Couple
Solvent
Supporting Electrolyte

Table 4.3: Components associated with mass-transfer resistance within an RFB.

Mass-Transfer (R_{MT})
Flow Field Geometry
Inadequate delivery of Active Species to the Electrode Surface
Concentration of Ionic Species

4.2.1 Chemistry Considerations

While developing an RFB, several chemical characteristics must be considered: solubility, viscosity, energy density, cyclability, stability, and safety. These can be addressed through redox couple, solvent, or supporting electrolyte selection. Several redox couples have been proposed, generally containing inorganic materials(81). Examples are shown in Table 2.1. The most widely accepted is the all-vanadium RFB. Organic redox couples have been proposed and offer advantages over their inorganic counterparts(74; 30; 32). Organic molecules offer some advantages over their inorganic counterparts. They can be produced virtually anywhere, tend to be less expensive, and allow improvement of their molecular structure. Their structure can be changed to alter specific properties such as stability, solubility, and energy density.

Losses in an RFB, associated with charge and mass-transfer, are affected by the chemical characteristics of the redox species. To mitigate these losses, development of an organic compound that promotes fast kinetics at the electrode is crucial. Active species concentration and electrolyte properties influence the mass-transfer losses(60). Increasing solubility of the active species could decrease mass-transfer losses by enabling a higher concentration of active species in solution. With a solubility of 2 M, the proposed chemistry is an ideal RFB redox couple.

Previously reported results have shown that various carbazole, phenothiazine, and phenothiazine 5,5-dioxide derivatives can be prepared as electron donating groups which possess high oxidation potentials, robust electrochemical stability, and suitable solubilities in nonaqueous solvents(36). Reciprocally, modified pyridinium and extended viologen systems have been evaluated as electron accepting anolyte materials capable of undergoing highly reversible reductions at low potentials. Linkage of these two moieties can occur after satisfactory independent optimization of the redox properties, solubility, or synthetic procedure of the solitary donor or acceptor species. Implementation of this synthetic approach has produced $C - L - A$ active materials capable of a net one electron operation as well as $C - L - A - L - C$ multielectron systems capable of a net two electron operation(57). In the aforementioned multi-electron system, the donor moieties undergo a one electron oxidation whereas the acceptor moiety undergoes a two-electron reduction. The RFB

chemistry proposed at MSU has been developed using nonaqueous solvents that enable voltages in excess of 3.0 V. The primary advantage of the proposed system is that the donor and acceptor compounds are linked, producing a symmetric flow battery which mitigates the deleterious effects of crossover of active material across the membrane, allows for continuous improvement, and the use of a nonaqueous solvent(82).

Supporting electrolyte are crucial as they maintain a balanced charge. We have studied Tetraethylammonium tetrafluoroborate ($TEABF_4$) and Lithium hexafluorophosphate ($LiPF_6$). Others include that were initially considered include: sodium tetrafluoroborate ($NaBF_4$), potassium tetrafluoroborate (KBF_4), potassium hexafluorophosphate (KPF_6), sodium perchlorate ($NaClO_4$), and potassium trifluoromethanesulfonate CF_3KO_3S.Viscosity and solubility measurements, summarized in Tables A.2 and A.1, aided in system development.

The supporting electrolyte and redox compounds must be dissolved into a solvent. Choosing a solvent with high ionic conductivity and low viscosity helps mitigate mass-transfer losses. The solvent acts as a media for the redox reactions to occur. Using an aqueous solvent in an RFB prevents the cell voltage from reaching any value higher than 1.2 V(82). Nonaqueous solvents can reach cell voltages much higher than 2 V. While higher voltages can be achieved, there are several drawbacks. Nonaqueous solvents are more expensive and more reactive with dissolved components in the system when compared to an aqueous solvent. Propylene carbonate (PC), acetonitrile (ACN), ethylene carbonate, acetone, ethylene glycol, sulfuric acid (H_2SO_4) and hydrogen peroxide (KOH) are examples of nonaqueous solvents used in flow batteries(50; 83; 84; 85). Solvent choice can affect a range of a characteristics of the system, from material compatibility to the solubility of the active species. Acetonitrile is commonly used as a solvent for nonaqueous RFBs(86). This is primarily due to its high ionic conductivity and cell potential window(87).

4.2.2 System Design and Manufacturing Considerations

RFBs are typically composed of several parts including the flow cell, plumbing, current collector, porous electrode, an ion-selective membrane, storage tanks, a battery management system,

heat exchangers, and pumps. When the active species reaches the end of its usable life, it can be easily be replaced by draining the tanks without replacing all the components. The anode, cathode, and electrolyte are sealed within the cell. RFBs enable the reuse of cell components because the anolyte, catholyte, and supporting electrolyte can be drained from the system and refilled with fresh solution. This decouples the energy storage from the power producing components. A new perspective can be used when developing these electrochemical systems. An RFB's performance and durability are influenced by engineering decisions related to system components including: the flow field geometry, reaction chamber, porous electrode, current collector, and membrane.

4.2.2.1 Flow Field Geometry

Electrochemical performance is impacted by alterations to the geometry of the flow cell. Natural transport mechanisms such as diffusion, advection and capillarity can be enhanced by the flow field and current collector design(7). The flow rate can be optimized to minimize losses within a flow cell and stack(88). To maximize the conversion of active species the the cell must be designed with a flow field that improves mixing of the active species containing solution. This is to maintain the rate of the reaction by supplying fresh active species to the surface of the electrode as fast as they can be converted. This can increase the charge capacity by improving the conversion rate. The ideal cell geometry is not immediately obvious. Figure 2.6 shows several designs of the flow field that contain ridges and channels that could potentially decrease mass-transfer losses by enhancing through advective (also referred to as convective) transport(7). Flow field geometry design considerations can be separated into three categories: sizing, shape, and topology optimization(89). Understanding the effect of fluid dynamics and electrochemical kinetics on performance is critical. This configuration is commonly referred to as an interdigitated flow field geometry(90; 91; 92; 47). Ridges, channels and, other geometric features change the velocity of the fluid. Fluid velocity is advections' primary driving force. Ridges, channels, and other flow impeders force fresh solution into the porous electrode, there-by increasing supply of active species to the electrode surface.

Previous studies, which focused on RFB flow field optimization, applied theories related to the design of thermal-fluid flow systems(89). Flow phenomena was modeled as a forced convection problem. The concentration of vanadium species was treated as passive scalars governed by forced advection. Fluid flow of the active species, through the RFB, impacts the electrochemical kinetics. This is defined through fundamental equations that describe ion and mass transport.

Equation 4.1, the Nernst-Planck equation, describes the mass and ion transport of a species by relating the flux of ions (N_i) to the concentration (c_i) and potential (ϕ) gradients . The flux of ions is determined through migration, diffusion, and convection terms. Other parameters include the charge of the species (z_i), Faraday's constant (F), mobility of the ion (u_i), diffusion coefficient (D_i), and the molar average velocity of the fluid (u). The subscript i denotes the species of interest. Equation 4.2, the Butler-Volmer equation, describes the electrochemical kinetics at the electrodes by relating the average current density (i) and the surface overpotential (η_s). Other parameters include the exchange current density (i_o), universal gas constant (R), temperature (T), and anodic or cathodic transfer coefficients ($\alpha_{a,c}$)(7).

$$N_i = -z_i\, u_i\, F c_i\, \nabla\phi - D_i \nabla c_i + c_i u \tag{4.1}$$

$$i = i_o\, [exp((\alpha_a \eta_s)/RT)) - exp((\alpha_c \eta_s)/RT)] \tag{4.2}$$

Mass-transfer resistance within the cell can be mitigated by delivering fresh species to the electrode surface. This will be significantly impacted by the flow field geometry. The impact that fluid dynamics has on transport is captured by the last term in Equation 4.1 involving the flow velocity. Replacing the activated species with fresh solution through mixing is crucial to ensure the highest charge-discharge efficiency and to maximize usage of active species. Turbulent flow is characterized as a flow that has variances in speed and direction of the fluid. Laminar flow is characterized as a sheet-like flow with uniform velocity. Turbulent flow is defined as having a Reynolds number greater than 2900, while laminar flow is defined as having a Reynolds number less than 2300. The fluid velocity (u), characteristic length (l), density (ρ), and dynamic viscosity (μ_{Re}) are used to calculate the Reynolds number with the formula: $Re = u\rho l/\mu_{Re}$.Turbulent flow will

ensure mixing and requires a high fluid velocity (v). A higher value of v will increase convective transport.

Promoting turbulent flow within the cell will increase the amount that the solution is mixed. The length of a path that the fluid is forced through and the velocity, are variables that can be modified to generate turbulent flow within the cell. Fins, channels, and other turbulent promoting structures can be added to the flow field in order to replace the active species at the electrode surface through mixing that occurs with turbulence. This can increase mass-transfer rates through mixing and a higher electrolyte velocity. The novel chemistry minimizes the issue of crossover but requires a system design that is unique. The chemical reaction kinetics have not been studied in detail. The use of fins to distribute flow, determining the geometry of the reaction chamber and flow field, and material choices will be explored.

4.2.2.2 Reaction Chamber

The flow cell cavity should be entirely filled with solution during operation. Any unused space can be considered a waste. The inlet and outlet of the chamber should promote even distribution across the whole flow field. The distribution of solution across the flow cell was discussed in Chapter 2. To maximize conversion rates, the flow through the cell should be distributed uniformly to increase active species conversion and contact with the electrode surface area. The electrochemistry was not considered when the CFD model was developed. Future modeling may couple fluid dynamics with electrochemical kinetics within an RFB.

The reaction chamber encompasses the porous electrode, flow field, and current collector. To reduce ohmic losses, the depth of the chamber must be as small as possible. This is because ohmic resistance increases with path length. A zero-gap architecture can decrease ohmic losses in the current collector and the porous electrode(60; 2). This means that the current collector, membrane, and electrodes are in direct contact with one another to reduce ohmic losses. Since the reaction chamber houses these components, it must be designed with the shortest distance between each electrode, while still housing the critical components in a way that allows efficient operation.

To improve the capacity, it is critical to maximize the conversion of active species from one oxidation state to another through the reaction chamber, in a single pass. Many RFBs recirculate the anolyte and catholyte through the cell many times in order to increase the overall conversion rate. Reactant conversion rate is an issue that is present with all types of flowing reactors. If the electrode near the outlet of the chamber is starved, parasitic reactions can occur. This can cause parasitic reactions such as gas evolution or electrode corrosion can occur(2). There is not a clear solution as to how to fix this issue.

4.2.2.3 Porous Electrode

Flow batteries typically include a porous electrode that allows the active species to flow through it to maximize the conductive surface area, which decreases charge-transfer resistance. A porous electrode's internal surface area is referred to as its brunauer-emmet-teller or (BET) surface area(93). This is measured as a materials' ability to adsorb gas molecules on its surface. A thicker porous electrode increases the surface area for the electrochemical reactions to occur; however, ohmic losses will increase due to an increased ionic path length and a denser structure will increase hydro-static losses associated with energy required to drive the flow(45). It has been shown that a higher local velocity in the porous electrode was observed when an electrode with higher porosity was used(89). This means that number and size of pores will alter the fluid flow and affect the electrochemical performance. The generation rate of active species, at the electrode surface, directly correlated to the local fluid velocity. Less porous electrodes restrict the flow of the solution, which increases the energy required for pumps. This was previously discussed in Chapter 2.

Graphite felt is commonly used in RFBs as a porous electrode. Although widely accepted for use in flow batteries, there are limitations to be considered. Xing et al. investigated the effects different solvents have on the graphite electrode in li-ion batteries(94). The use of propylene carbonate instead of ethylene carbonate caused catastrophic exfoliation of the graphite structure. As literature has revealed, standalone graphite felt can be improved using various techniques. Electrode materials must have high electrical conductivity, good mechanical properties, strong chemical resistance, and

offer a long lifecycle to prevent maintenance costs. Carbon based materials are optimal because they do not generally undergo dissolution or permanent oxidation while chemical oxidation is occurring. Skyllas-Kazacos et al. summarized the various porous electrode designs that have been proposed for different RFB chemistries(95; 96). The reaction kinetics of the system must be evaluated when considering an electrode material. For example, carbon felt, with traces of gold and lead, was found suitable for iron-chromium RFBs. Another method of improving the characteristics of the felt is to thermally treat the felt or use sulfuric acid as well as heat to improve its chemical properties. Rather than using graphite felt, carbon fiber has been proposed as an electrode material due to its high conductivity and strong mechanical properties. Carbon or graphite can be heat bonded onto conductive plastic sheets to increase the chemical properties and electrical conductivity. Electrode materials must be resistant to overcharge to prevent degradation. Carbon-based electrodes allow for current density ranges up to 100 mA/cm^2, but with novel composite electrode materials being developed, higher current densities can be achieved(95).

4.2.2.4 Current Collector

Flow in an RFB is necessary to replace reactants at the electrode surface. The two basic types of flow configurations can be categorized as either flow-through or flow-by. In a flow-by configuration, fluid flow is perpendicular to current flow. In a flow-through configuration, current flow is parallel to fluid flow(7). Determining which configuration is best suited for the RFB comes down to how each configuration affects the performance of the battery and cost. Studies including, one dating back to 1979, found through numerical analysis that the flow-by configuration was superior from an economic and functional standpoint(97). Choosing a current collector material is dependent upon the material cost and electronic conductivity, meaning the current collector must be highly conductive yet inexpensive. Inert metals are a common choice as current collectors. An inert metal, such as a noble metal, is characterized by its resistance to corrosion and oxidation. Metals such as this are relatively expensive and include silver, platinum, gold, iridium, osmium palladium, rhodium and ruthenium. For this reason, stainless-steel has also been considered as a conductive

electrode material due to its inert qualities; however, trace amounts of iron still exist in stainless steel alloys. Ferrous ions at a concentration of several $\mu m/L$ have been observed to be released when an electric pulse is applied to a stainless-steel electrode and can lead to oxidation(98).

4.2.2.5 Membrane

There are several types of membranes or separators used in batteries including nonwovens, supported liquid membranes, polymer electrolyte, solid ion conductors, microporous separators, and ion-selective membranes(99). Typical RFBs require an ion-selective membrane to separate the redox active species, act as a transport medium for charge balancing supporting electrolyte, and prevent a short circuit. If the active species mix, the RFB will self-discharge and permanently lose charge capacity if not rebalanced. The membrane selectively permits the conduction of charge balancing ions while also preventing the mixing of the redox couples. There are three mechanisms involved in active species crossover through the membrane: diffusion driven by the concentration of active species, migration driven by a potential gradient, and advection driven by a pressure gradient(100; 101).

An ion-selective membrane acts as a medium for charge balancing ions to travel from one electrode to the other along a concentration gradient. It is a negatively charged material that repels anions and allows the migration of cations. An ideal membrane must have pores that are large enough for cations to pass through, while small enough to prevent the active species from crossing over. Nafion extrusion cast membranes are a common choice for RFBs, fuel cells, and electrolysis applications. Their chemical stability and proton selectivity make them ideal separators for typical RFBs. Zhou et al. found current efficiencies greater than 90% with Nafion 112 and 115 membranes when testing a vanadium RFB(100). It is common to pretreat Nafion membranes to alter its performance(52; 53). Celgard 2400 has previously been used as a microporous separator in nonaqueous RFBs(53; 51). Bang et al. found that using a modified electrospun Nafion/PVA fibrous membrane resulted in a higher coulombic efficiency than a Nafion 212 or Celgard 2400 membrane(51). Using the Celgard 2400 separator decreased the coulombic efficiency due to its

non-selectivity resulting in an increase in crossover of unwanted species.

A significant difference between an ion-selective membrane and a simple microporous separator is its porosity. A microporous separator has a pore size of 5-10 nm while ion-selective membranes' pores are less than 2 nm(99). By increasing the size of the pore that the cations pass through, the ohmic resistance within the cell is decreased. In a symmetric RFB, the active species may still crossover as they do with a typical membrane; however, it will return to its proper state during normal operation. In a typical RFB, the anolyte and catholyte molecules are different. Once improperly mixed, they can't easily be separated and reused.

4.3 Experimental

EIS was used to investigate how much influence the separator or ion-selective membrane has on internal resistance. Several methods have been used to investigate electrochemical phenomena in RFBs using EIS(102; 80). Experimental procedures and data analysis techniques were compared to quantify the benefit of using a linked chemistry and a microporous separator rather than an unlinked chemistry paired with an ion-selective membrane. Losses associated with the transport of charge balancing ions across the separator medium were evaluated. A Scribner RFB test fixture was assembled with an electrode area of 5 cm^2. A solution was synthesized to act as a medium for ion transport. $TEABF_4$ was chosen as a supporting electrolyte and had a concentration of 1 M while the novel molecule had a concentration of 0.1 M. Both species were dissolved in PC. EIS was run using a Gamry reference 3000 potentiostat. The hypothesis that using a simple separator, rather than an ion-selective membrane, will greatly reduce internal cell resistance was tested. One experiment included using an untreated Nafion 117 membrane and a Celgard 2400 microporous separator. During EIS, an alternating current or potential is applied to an electrochemical cell while measuring the resistance(69). Gamry offers a basic tutorial on running EIS with their devices(103; 104; 105). EIS was run in a two-electrode configuration which includes the working and working sense electrodes attached to the current collector on one side of the cell and the reference and counter electrodes attached to the other floating ground and counter sense electrodes

were not used. A porous electrode, manufactured by Sigracell, with a BET surface area of 750 cm^2 was used. Electrochemical measurements were performed with a starting frequency of 100 kHz to a final frequency of 0.01 Hz. A sinusoidal AC voltage of 10 mV rms was applied to the cell.

4.3.1 Results and Discussion

Figures 4.2 and 4.3 show the resulting bode and nyquist plots produced from the experiment studying the nafion ion-selective membrane. These plots were fit using a theoretical equivalent model shown in Figure 4.5. Individual components are grouped together to represent phenomena observed in the physical world. Figure 4.4 shows the results and the experimental parameters. The lumped cell resistance was the only parameter that was significantly affected when the separator was altered. It was shown that an ion-selective membrane increased this value by a factor of three.

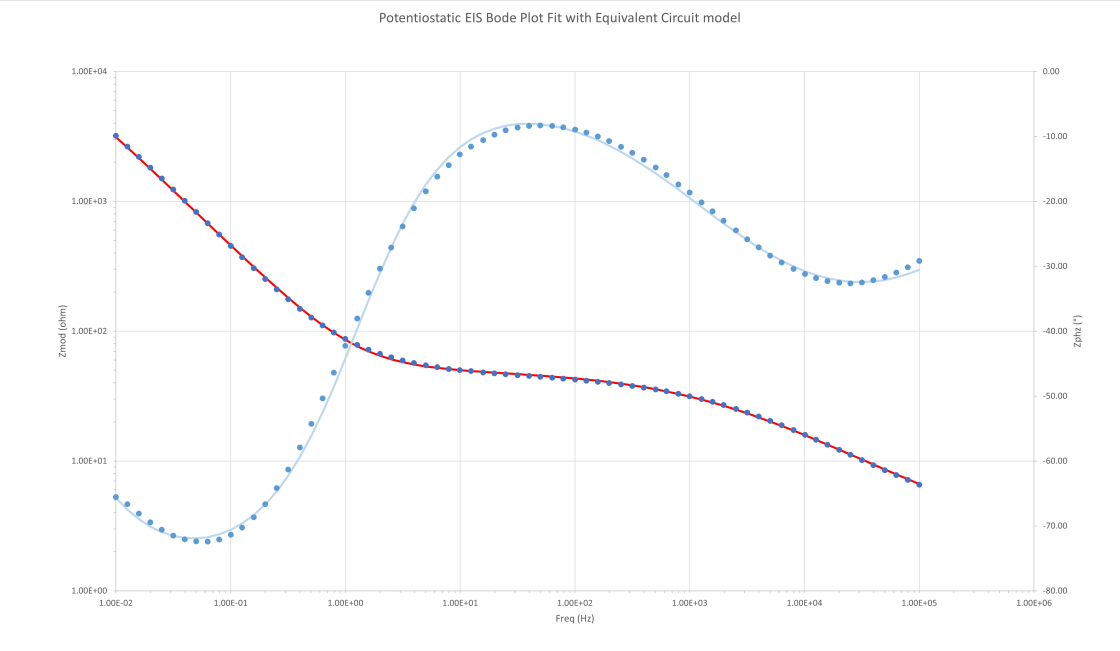

Figure 4.2: Resulting bode plot fit with a theoretical equivalent circuit model. The dots are the experiment points measuring impedance at various frequencies and the solid line is the equivalent circuit model's fit.

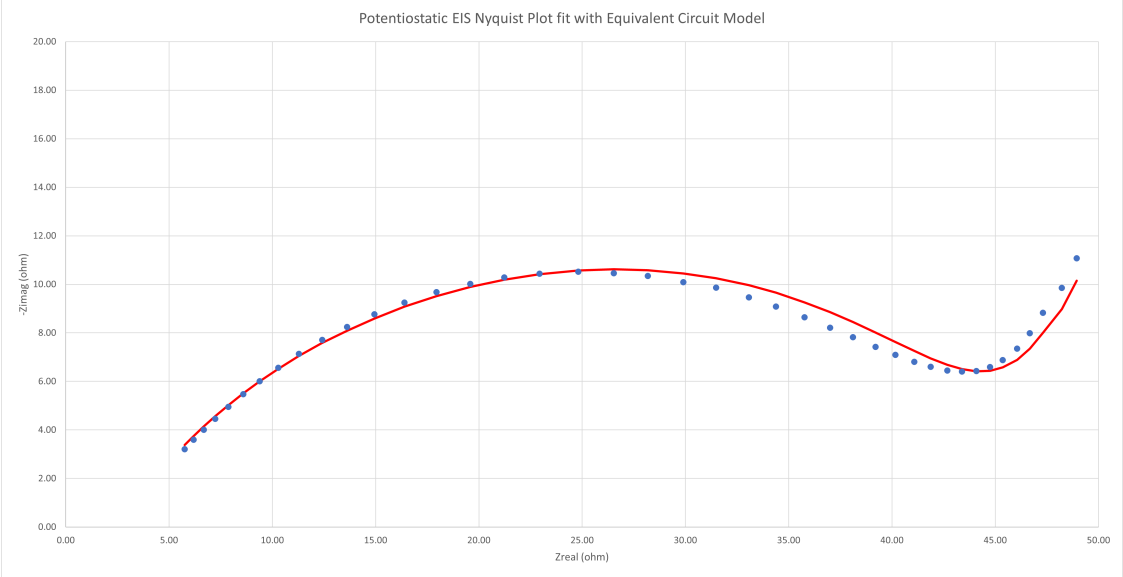

Figure 4.3: Resulting nyquist plot fit with a theoretical equivalent circuit model. The dots are the experiment points measuring impedance at various frequencies and the solid line is the equivalent circuit model's fit.

Redox Pair	0.1 M D2A2
Electrolyte	1 M $TEABF_4$
Frequency Range	100 kHz-0.01 Hz
AC Voltage	10 mV rms
Solvent	Propylene Carbonate
Flow Cell	Scribner Redox Flow Cell

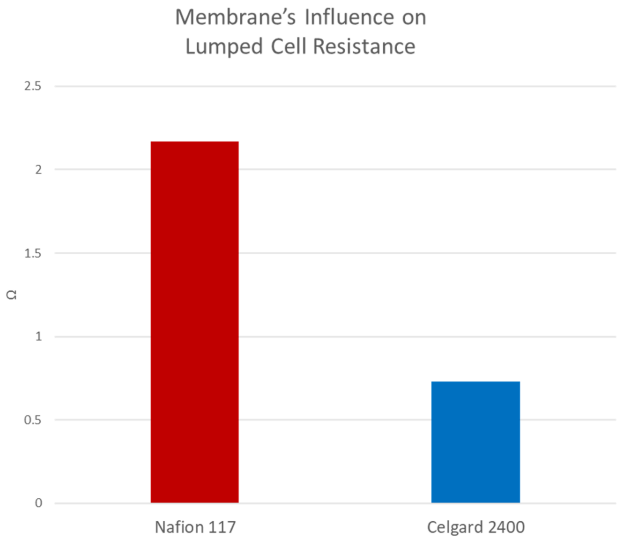

Figure 4.4: Experimental parameters and lumped cell resistance comparing an ion-selective membrane (Nafion 117) and a simple microporous separator (Celgard 2400).

4.3.2 EIS Equivalent Circuit

After performing an EIS scan, the resulting data can be fit to a theoretical model network of components(80; 102). The next step is to determine how many components are required.

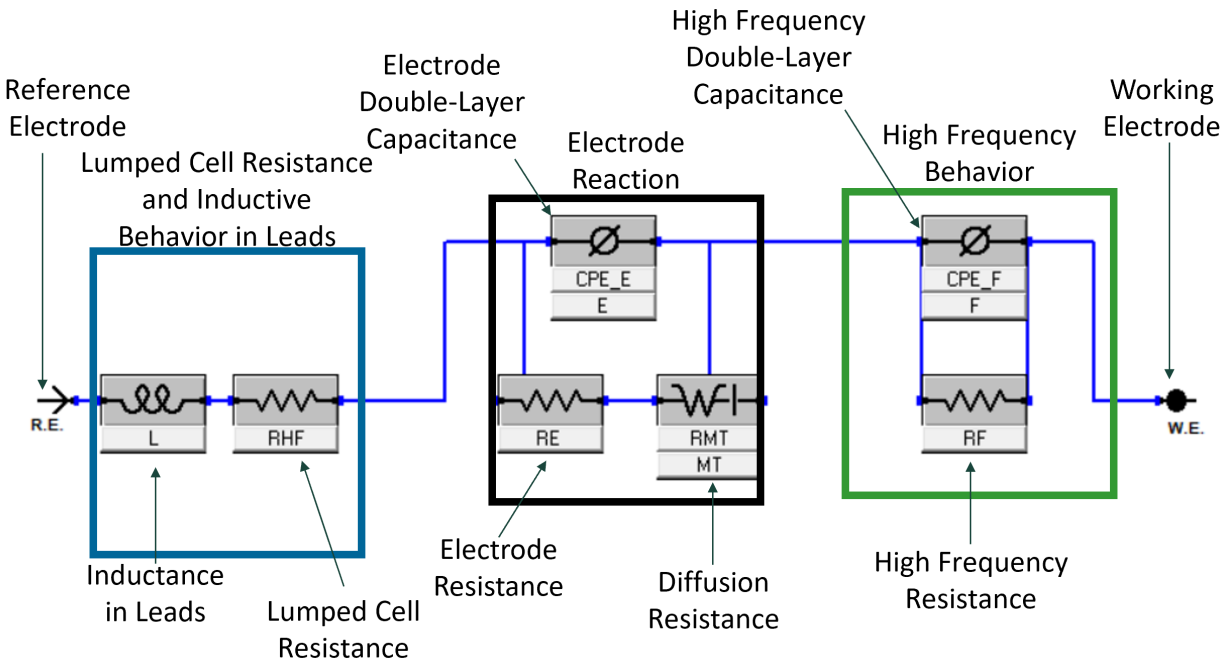

Figure 4.5: Equivalent circuit developed to evaluate RFBs using EIS.

Generally, simplifying a system by using the least number of components possible is better to enable development of a realistic comparison. The network should correspond to a relatable and physically intuitive model. Once a realistic model is developed, the next step is to evaluate the accuracy by fitting it to experimental data from an EIS scan. The error bar corresponding to each of the values, calculated during the fitting process, must be smaller than the component's value. The third metric that can be assessed is the "goodness of fit" or X^2 value(103). This value can indicate increases in accuracy from specific modifications once the first two metrics are evaluated. For example, if the value decreases by a factor of 10 or 100, when a component is added or removed from the model, it is an indication of increased accuracy of the model network's representation of the experimental system and resulting data.

Existing literature was used to analyze results from the EIS experiments(102; 80; 103; 78; 106). An equivalent circuit can be used to fit the resulting nyquist and bode plots to a series of theoretical components. These components may include a combination of resistors, capacitors, inductors, and other theoretical components that have been deemed useful for the analysis. Gamry's analysis

software, echem analyst, was used to fit a theoretical model to the results. As previously summarized in Tables 4.1, 4.2, and 4.3, losses can be categorized into three primary types including ohmic resistance (R_{oh}), charge-transfer resistance (R_{CT}), and mass-transfer resistance (R_{MT}).

Literature revealed that there are different approaches to circuit modeling. Escalante et al. proposed a comprehensive model used to evaluate how separators affect the performance of a Vanadium RFB(102). Mazur el al. proposed a four-point evaluation method to study the distribution of ohmic and faradaic losses within a Vanadium RFB with the goal of the model(80). The proposed equivalent circuits were used to fit experimental data. The viability and quality of fit were compared.

The equivalent circuit, shown in Figure 4.5, was used to evaluate the results. Each equivalent circuit component that is used will impact the analysis differently and can be paired to study lumped cell resistance, inductive behavior in the leads, the reaction at the electrode, and high frequency behavior(102). An inductor (L) can be added to represent inductive behavior from the formation of a surface layer, like fouling or a passive layer, or from errors in the measurement. It can also be used to measure inductive in the leads. A series of resistors can be used to measure lumped cell resistance (R_{HF}), electrode resistance (R_E), and high frequency resistance (R_F). A warburg element (ω) accounts for diffusion resistance associated with the electrode reaction(77). Constant-phase-elements describe the electrochemical double layer capacitance from mass transport limited diffusion from the electrode reaction (CPE_E) and high frequency behavior (CPE_F).

4.4 Conclusions

Proper application of the techniques and theories described will allow the development of highly efficient RFBs, enabling the modernization of the electrical grid and the integration of low-cost renewable energy sources on a large scale. Literature review has led to a better understanding of synthesizing redox couples, manufacturing flow cells, and performing electrochemical experiments. EIS was performed to study the resistance associated with the membrane. The hypothesis that replacing an ion-selective membrane with a microporous separator would decrease resistance in the cell was confirmed. Although this was expected, quantifying it helps when developing a

complex RFB. These results, a validated experimental procedure, and analysis method could be used to evaluate previously mentioned design considerations quantitatively. For this reason, EIS has proven to be a valuable tool to:

- demonstrate that internal resistance decreases when a microporous separator replaces an ion-selective membrane;
- compare components which impact electrochemical performance;
- develop a procedure to analyze individual components of RFBs.

Future work will compare experimental results that employ theories and techniques that were described in this study. Incorporation of the procedures described can be used to investigate the effect that each unique design consideration has on internal resistance. RFB performance could be iteratively studied and improved at a component level.

CHAPTER 5

INTERRELATIONSHIP BETWEEN EXTENDED TRANSPORT PATHWAYS OF MIXED CONDUCTING ELECTRODES AND DELAMINATION IN SOLID OXIDE ELECTROLYZER CELLS

5.1 Introduction

A microscale model was developed to investigate the delamination of the oxygen electrode in a Solid Oxide Electrolyzer Cell (SOEC). A cell consists of a solid-state electrolyte of Yttrium-Stabilized Zirconia (YSZ), a Mixed Ionic and Electronic Conducting (MIEC) buffer layer of Gadolinium-Doped Ceria (GDC), and a Lanthanum Strontium Cobalt Ferrite (LSCF) MIEC electrode. YSZ is a pure ionic conductor, with oxygen vacancies being the only mobile species; GDC is a mixed oxygen vacancy (high) and electron (low) conductor whose transference number depends on the gas composition and temperature; LSCF is also a mixed conductor, but with much higher electron hole conductivity than that of oxygen vacancy. The dopant is immobile and maintains charge neutrality together with other charged species. It has been hypothesized that competition between the two-phase boundaries (2PBs) and three-phase boundaries (3PBs) leads to an unbalanced lattice structure, which causes expansion, and results in delamination. To counter the delamination mechanism, a thin and highly electronically conductive bilayer of tantalum doped Strontium Cobalt oxide (SCT) was added. It was found both experimentally and through modeling that using a bilayer electrode enhanced the 2PB oxygen evolution reaction could be enhanced, thereby decreasing the imbalance and preventing delamination.

Hydrogen (H_2) gas generation, storage, and consumption is being considered as a viable form of long duration, grid-scale energy storage(107; 108; 109; 110; 111). The combination of efficient electrolyzers and inexpensive renewable energy have great potential for decarbonizing the electrical grid and transportation. H_2 can be produced and used in fuel cells through electrolysis and electrochemical recombination reactions. Swiss scientist Christian Friedrich introduced the concept of fuel cells in 1839 as a device capable of combining H_2 with oxygen(112; 8). Shortly

after, English scientist William R. Grove confirmed the technical feasibility of fuel cells as a power generation technology(113). From there, many fuel cell configurations and materials have been proposed and implemented as an efficient form of power generation(8; 114; 9; 115). Fuel cell operation can also be reversed by supplying power to the cell and producing hydrogen and oxygen through electrolysis reactions. Electrolysis cells, sometimes referred to as water electrolyzers, can provide energy storage in the form of the gaseous H_2 and oxygen they produce. Electrolyzers can be classified by their operating temperatures and associated components. Low temperature systems operate below $100^{\circ}C$, use ion exchange membranes and expensive catalysts, and have energy efficiencies of about 75%(116).

A primary disadvantage of low temperature electrolysis is that it requires a large amount of electricity. High temperature electrolyzers are energetically favorable in the sense that electrolysis of water is increasingly endothermic as the temperature rises(9). Operating at temperatures between $100^{\circ}C$ and $850^{\circ}C$ reduces the electrical power required due to the thermal enhancement of the H_2O splitting process, potentially achieving 100% efficiencies(10). Since the thermal energy required for the electrolysis reaction can be obtained from waste heat produced within the cell, the electrical energy demand is reduced which decreases the H_2 production price. The price can be decreased further if the heat required is supplied by an external source such as nuclear power, renewable energy, or waste heat from another process.

This study focuses on high temperature electrolysis cells, specifically Solid Oxide Electrolysis Cells. SOECs are an appealing electrolysis technology because of key differences, when compared to typical low temperature electrolysis cells, including a significant power increase and higher efficiencies(9). It is well known that SOECs suffer from oxygen electrode-electrolyte interface delamination during operation, but the physics involved are not fully understood(114). A clearer understanding of the electrochemical processes involved in porous or composite electrodes is needed(117). It is crucial to determine the primary delamination mechanism within the composite electrodes to increase the durability of SOECs, aiding the adoption of H_2 as a form of utility-scale long duration energy storage.

We describe the primary reaction pathways of interest, namely the 2PBs and 3PBs through which the oxygen desorption and evolution reactions occur. Treatment of each of these boundaries has been discussed in the literature(8; 12; 118; 119; 120; 121). Specifically, for the interface between 2PBs at gas/MIEC electrode interface, there have been debates whether the reaction of interest is chemical or electrochemical in nature(8; 12; 122). Adler et al. described this as a purely chemical process governed by the neutral combination of species; however, Huang and Goodenough described this process as an electrochemical reaction(8; 12). Experimental studies have indicated that the gas/MIEC electrode interface reaction is a multiple-step process that involves charged species and could be electrochemically driven(123; 124; 125). Inspired by prior work, in this model, we treat the overall reaction as a combination of oxygen desorption and oxygen evolution reactions. The former is a chemical reaction (i.e., it does not consume or generate any net charge), whereas the latter is an electrochemical reaction driven by surface overpotential. We hypothesize that competition between the 2PBs and 3PBs results in a species transport imbalance. This imbalance strains the lattice structure and is thought to be the primary mechanism responsible for delamination. Microscale model theory, parameter selection, experimental validation, and results are discussed. The results of the model support our hypothesis, which is that at high overpotentials the reaction at the 3PB dominates the overall current over the 2PB. The 2PBs' surface area is several orders of magnitude larger than the 3PBs', which leads to a large imbalance of current and delamination of the electrode. Further experimental analysis and numerical results demonstrate that the 2PB reaction can be enhanced by adding a thin bilayer of Tantalum doped Strontium Cobalt oxide SCT. This reduces the imbalance and could prevent delamination.

5.2 Microscale Model Theory

Figure 5.1 depicts the idealized model domain and boundary conditions used to describe transport phenomena within a SOEC. The governing equations for each domain are summarized in Table 5.1. The boundary conditions for each interface are shown in Table 5.2. To investigate the delamination mechanism, a microscale model was developed. The numerical model was built in

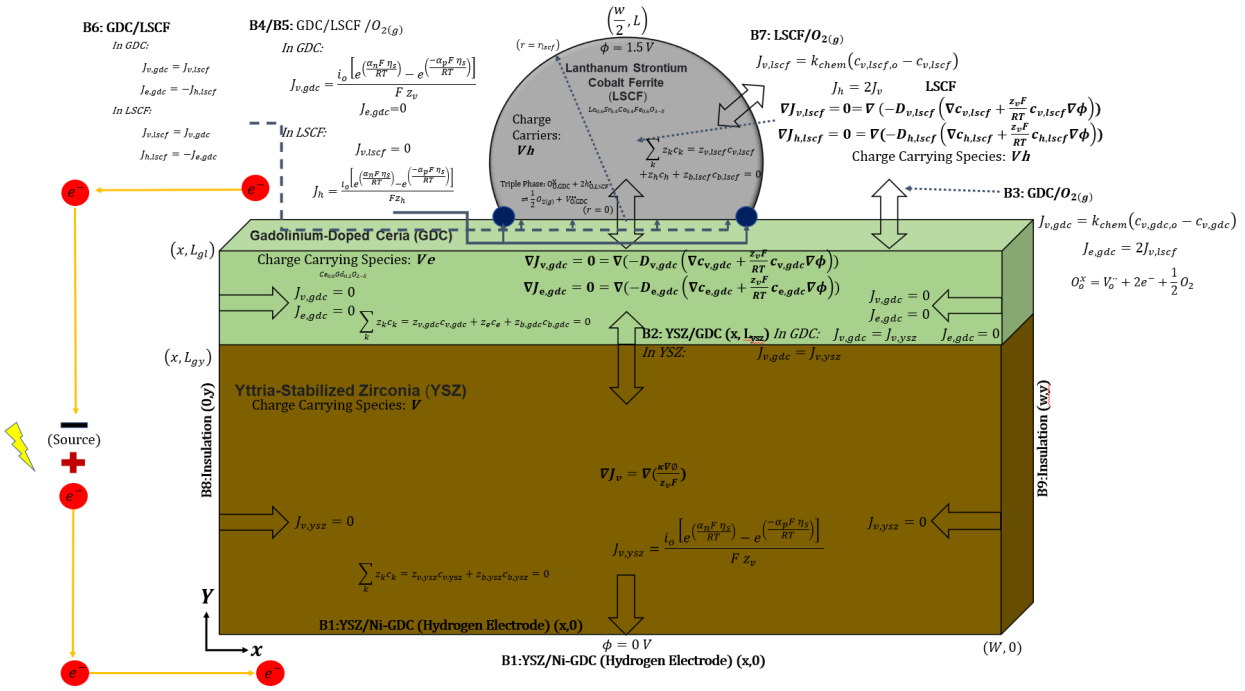

Figure 5.1: An SOEC's oxygen electrode and electrolyte layers shown with the boundary conditions and governing equations. These describe the flux J of each of the species in the electrode and electrolyte layers. The model domain includes a small section of YSZ and GDC layers a single particle of LSCF particle having Width (W) and length (l) of 20 μm.

Table 5.1: Charge carriers, dependent variables, and governing equations describing the transport phenomena within each layer shown in Figure 5.1.

Domain	**Charge Carriers**	**Dependent Variables**	**Governing Equations**
YSZ	V	ϕ	$\nabla J_{v,ysz} = 0$ $J_{v,ysz} = \left(\frac{\sigma_i \nabla \phi}{F z_v}\right)$
GDC	V,e	c_v, ϕ	$\nabla J_{e,gdc} = 0$ $J_{e,gdc} = -D_{e,gdc}\left(\nabla c_{e,gdc} + \frac{Z_e F}{RT} c_{e,gdc} \nabla \phi\right)$
LSCF	V,h	c_v, ϕ	$\nabla J_{v,lscf} = 0$ $J_{v,lscf} = -D_{v,lscf}\left(\nabla c_{v,lscf}\right)$

COMSOL v5.4, using the coefficient form partial differential equation module. Figure 5.2 shows the geometry and domain of interest. Ion transport proceeds from bottom up, starting from the H_2 electrode, through the electrolyte (YSZ) which is only conductive to oxygen ions, through buffer layer of a MIEC (GDC), and finally through a mostly electronically conductive electrode (LSCF).

Table 5.2: Boundary conditions used to describe 2PBs and 3PBs within an SOEC consisting of a solid-state,multilayer electrolyte-electrode structure shown in Figure 5.1.

Interface	**Boundary Condition**
YSZ/Ni-GDC (In YSZ) (2PB)	$J_{v,ysz} = \frac{i_o}{Fz_v}\left[e^{\left(\frac{\alpha_n F\eta_{s,ygn}}{RT}\right)} - e^{\left(\frac{-\alpha_c F\eta_{s,ygn}}{RT}\right)}\right]$ $\phi_{eq} = 0$
YSZ/GDC (In YSZ) (2PB)	$J_{v,ysz} = J_{v,gdc}, \phi_{ysz} = \phi_{gdc}$
YSZ/GDC (In GDC) (2PB)	$J_{v,ysz} = J_{v,gdc}, \phi_{ysz} = \phi_{gdc}, J_{e,gdc} = 0$
GDC/$O_{2(g)}$ (2PB)	$J_{v,gdc} = k_{chem,gdc}(c_{v,gdc,o} - c_{v,gdc})$ $J_{e,gdc} = 2k_{chem,gdc}(c_{e,gdc,o} - c_{e,gdc})$
GDC/LSCF/$O_{2(g)}$ (3PB)	$J_{e,g3pb} = \frac{i_o}{z_e F}\left[e^{\left(\frac{\alpha_n F\eta_{s,g3pb}}{RT}\right)} - e^{\left(\frac{-\alpha_c F\eta_{s,g3pb}}{RT}\right)}\right]$ $J_{h,l3pb} = \frac{i_o}{z_h F}\left[e^{\left(\frac{\alpha_n F\eta_{s,l3pb}}{RT}\right)} - e^{\left(\frac{-\alpha_c F\eta_{s,l3pb}}{RT}\right)}\right]$ $\eta_{s,g3pb} = V_{cell} - \phi_{gdc} - E_{eq}, J_{e,gdc} = 0$
	$\eta_{s,l3pb} = V_{cell} - \phi_{lscf} - E_{eq}, J_{h,lscf} = 0$
GDC/LSCF (2PB)	$J_{v,gl} = \frac{i_o}{Fz_v}\left[e^{\left(\frac{\alpha_n F\eta_{s,glv}}{RT}\right)} - e^{\left(\frac{-\alpha_c F\eta_{s,glv}}{RT}\right)}\right]$ $\eta_{s,glv} = \frac{\mu_{v,lscf} - \mu_{v,gdc}}{2F} - E_eq$ $J_{e,gl} = \frac{i_o}{Fz_e}\left[e^{\left(\frac{\alpha_n F\eta_{s,gle}}{RT}\right)} - e^{\left(\frac{-\alpha_c F\eta_{s,gle}}{RT}\right)}\right]$ $\eta_{s,gle} = \frac{\mu_{e,gdc} - \mu_{h,lscf}}{F} - E_eq$
LSCF/$O_{2(g)}$ (2PB)	$J_{v,lscf} = k_{chem,lscf}(c_{v,lscf,o} - c_{v,lscf})$
LSCF/GDC (In LSCF) (2PB)	$J_{v,lscf} = J_{v,gl}$

A gas/solid interface reaction occurs at the surface of both the GDC and LSCF layers where oxygen ions (O'_s) may become oxygen gas($O_{2(g)}$). Electrons move from LSCF to an external circuit. A cylindrical geometry was chosen to represent the porous electrode with LSCF particles stacking together to form the solid matrix, following the work of Lu et al.(117). This approach allows us to qualitatively represent the electrode structure and observe the fundamental transport processes. Direct simulation of the porous microstructure would require advanced imaging techniques, which

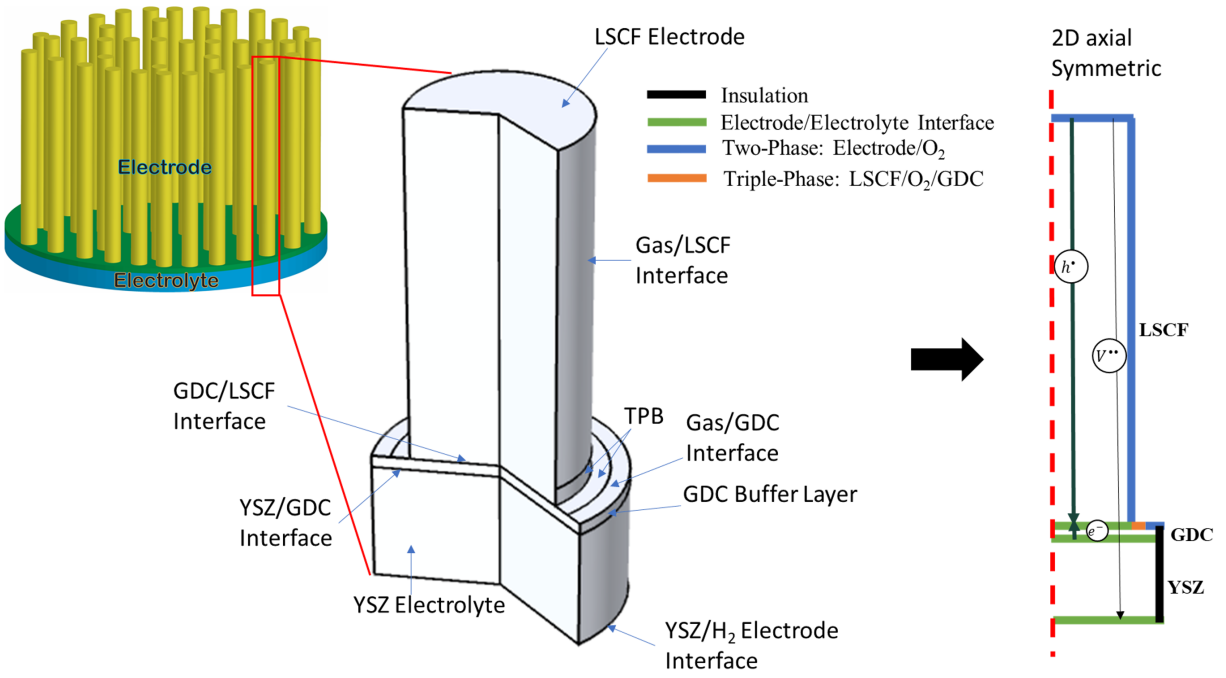

Figure 5.2: Diagram of idealized model domain which represents the complex electrode structure with cylindrical geometry.

was not undertaken here. It is believed that the 2D cylinder representation can be a valuable analysis tool, and direct microstructural simulation remains an interesting avenue for future work.

The transport pathways involve several charged species, including electrons (e'), electron holes ($h^{\cdot}$), and oxygen vacancies ($V_O^{\cdot\cdot}$), which are expressed using Kröger-Vink notation(126). The principal defect-forming could arise either from doping or from reduction/ oxidation reactions at solid-gas interface. Several categories of boundaries exist within the model including insulation, 2PBs, and 3PBs. Treatment of each of these boundaries and considerations while developing a multi-phase microscale model are discussed. The structure of the mixed-conducting LSCF sub-phase was represented as a cylindrical rod. This structure is related to the porosity and surface area. The rod was assumed to be highly conductive and electrically interconnected. These assumptions imply that the rod has a uniform electrochemical potential and is representative of the electrode as a whole(117).

Three types of material interfaces exist in a SOEC including:$O_{2(g)}$/ MIEC 2PB, $O_{2(g)}$/ elec-

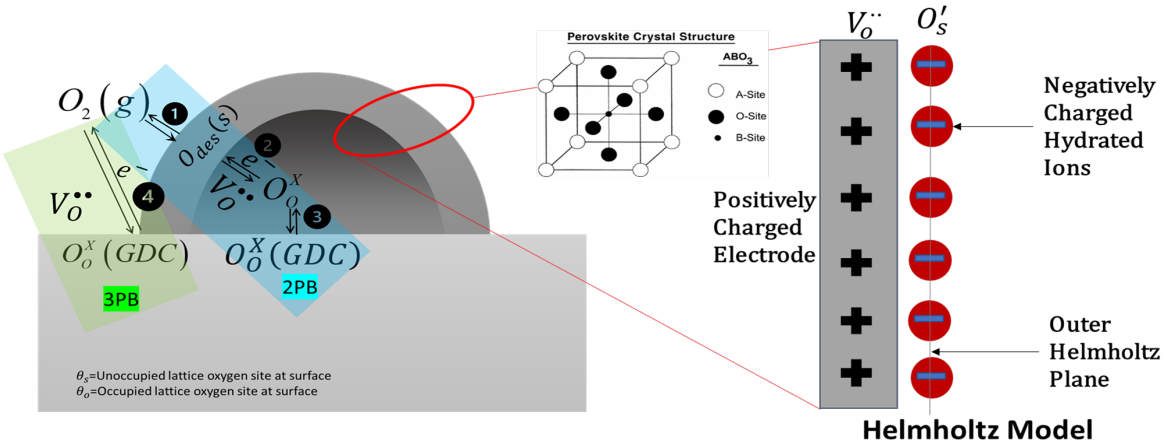

Figure 5.3: Diagram of transport pathways and equations and diagram of Helmholtz Model used to demonstrate the separation of charge at an electrode-electrolyte interface. Note that (s_{ad}) represents adsorption sites on the surface of the electrode.

Table 5.3: Elementary reactions shown in Figure 5.3.

No.	Reaction
1	$O_s' + h^{\cdot} \Leftrightarrow \frac{1}{2}O_{2(g)} + (s_{ad})$
2	$O_O^X + h^{\cdot} + (s_{ad}) \Leftrightarrow O_{ad}' + V_O^{\cdot\cdot}$
3	$O_{O,gdc}^X + V_{O,lscf}^{\cdot\cdot} \Leftrightarrow O_{O,lscf}^X + V_{O,gdc}^{\cdot\cdot}$
4	$O_{O,gdc}^X + h_{lscf}^{\cdot} \Leftrightarrow V_{O,gdc}^{\cdot\cdot} + \frac{1}{2}O_{2(g)}$

Table 5.4: Source term expressions derived to describe oxygen desorption and oxygen evolution reactions in the SOEC's multilayer electrodes shown in Figure 5.3.

No.	Source Term Expression
1	$r_1 = [k_f\theta_o^2 - k_b P_{O_2}\theta_s^2]$
2	$r_2 = k_{inc,0}\left[\left(\frac{(1-\theta_o)c_{h,lscf}}{(1-\theta_{o,0})c_{h0,lscf}}\right)exp\left(\frac{\alpha_2 F\Delta\chi}{RT}\right) - \left(\frac{\theta_o c_{v,lscf}}{\theta_{o,0}c_{v0,lscf}}\right)exp\left(\frac{(1-\alpha_2)F\Delta\chi}{RT}\right)\right]$
3	$r_3 = i_{03}\left[\left(\frac{c_{v,lscf}}{c_{v0,lscf}}\right)exp\left(\frac{\alpha_3 F\eta_3}{RT}\right) - \left(\frac{c_{v,gdc}}{c_{v0,gdc}}\right)exp\left(-\frac{(1-\alpha_3)F\eta_3}{RT}\right)\right]$
4	$r_4 = i_{04}\left[\left(\frac{c_{h,lscf}}{c_{h0,lscf}}\right)exp\left(\frac{\alpha_4 F\eta_4}{RT}\right) - \left(\frac{c_{h,gdc}}{c_{h0,gdc}}\right)exp\left(-\frac{(1-\alpha_4)F\eta_4}{RT}\right)\right]$

trode/ electrolyte 3PB, and electrode/ electrolyte interfaces. Gas/electrode 2PBs are present at the GDC/ $O_{2(g)}$ and LSCF/ $O_{2(g)}$ interfaces; 3PBs are present at the LSCF/ $O_{2(g)}$/ GDC interface; continuous charge transport occurs across the YSZ/ GDC and GDC/ LSCF interfaces. Treatment of each of these boundaries has been discussed in the literature(8; 12; 118; 119; 120; 121). There

are two major transport pathways. A representation of this is shown in Figure 5.3. The primary reactions are listed in Table 5.3 and the source term expressions are shown in Table 5.4. In the 2PB pathway, lattice oxygen in the GDC phase must first jump to the LSCF phase. Next, lattice oxygen in LSCF can become an adsorbed oxygen atom on the electrode surface, leaving an electron and an oxygen vacancy. Lastly, the surface oxygen can desorb from the surface and become a free oxygen molecule in the gas phase. The first two reactions are electrochemical in nature and are modeled by Butler-Volmer type expressions; the last reaction is purely chemical, which is dependent on the LSCF oxygen site coverage and the oxygen partial pressure in the gas phase. In the triple-phase boundary (3PB) pathway, only one electrochemical reaction occurs, in which lattice oxygen in the GDC phase can combine with an electron hole from the LSCF phase and produce gaseous oxygen.

The double layer at the electrode (GDC/LSCF)-electrolyte (YSZ) interface was modeled based on the theory described by the Helmholtz double layer model(127). LSCF is a highly electronically conductive MIEC electrode. It is assumed that the Fermi level electrochemical potential is uniform across its entire thickness. As previously described, the charge transport model within this domain can be reduced to a modified form of Ohm's law(11). Nernst-Planck theory is still needed to describe transport across the GDC electrolyte as it does not have a uniform fermi level potential, with a relatively low electronic conductivity but a very high ionic conductivity.

5.3 Experimental Validation and Model Parameters

According to the Kroger-Vink notation, the principal defect-forming reactions could arise either from doping or from reduction at a solid/gas interface. Here, as shown in Table 5.2, we listed boundary conditions that describe the reactions and the dominating charged species in the materials of interest, including YSZ, GDC and LSCF. The concentration of the charged species will affect the properties of the associated materials, such as conductivity. In this paper, all the parameters are from experimental measurements published in the open literature(118; 128; 129; 130; 131). They were adjusted in accordance with experiments performed by our team at the University of South Carolina and are listed in Figure 5.5. The specific material formulas are: 8%

Y_2O_3 fully stabilized ZrO_2 (8YSZ), lanthanum strontium cobalt ferrite ($La_{0.6}Sr_{0.4}Co_{0.4}Fe_{0.6}O_3$ (LSCF)), gadolinium-doped ceria ($Ce_{1-x}Gd_xO_{2-\delta}$(GDC)), Tantalum doped Strontium Cobalt Oxide ($SrCo_0.9Ta_0.1O_{3-\delta}$(SCT)). The electron hole mobility in LSCF is assumed to be the same as that of electrons in GDC.

Table 5.5: Reaction kinetic parameters included while developing the model from literature, some were adjusted using experimental data (denoted by *).

Material Interface	**Parameters (Units)**	**Single Layer /Bilayer**	**Reference**
YSZ/GDC	Exchange current density ($\frac{A}{m^2}$)	4000	(128)
GDC/LSCF	Exchange current density ($\frac{A}{m^2}$)	3600/11000	(128)
GDC/$O_{2(g)}$	Exchange current density($\frac{A}{m^2}$)	7200/22000	(128)
	Reaction rate constant ($\frac{mol}{m^2 s}$)	0.02	(118; 130)
LSCF/$O_{2(g)}$	Equilibrium surface oxygen coverage	0.07	(118; 129)
	Reaction rate constant oxygen absorption*. ($\frac{mol}{m^2 s}$)	0.7/2.2	(118; 130; 128)
	Reaction rate constant oxygen desorption*. ($\frac{mol}{m^2 s}$)	29/88	(118; 130; 128)
	Reaction rate constant oxygen evolution*. ($\frac{mol}{m^2 s}$)	70.01/0.04	(118; 130; 128)
	Surface overpotential (V)	1.07	(131)

There are two oxygen electrode designs to be simulated: single layer (with LSCF) and bilayer (with LSCF/SCT), as shown in Figure 5.4a. The SCT layer is on the order of a few nm, and its dimension is almost negligible compared to LSCF layer, therefore, we assumed that SCT will only change the oxygen electrode surface oxygen desorption and evolution reaction kinetics and does not change the bulk transport of vacancy and holes in the LSCF phase. Oxygen electrode overpotential vs current density measurement from University of South Carolina for both designs have been used to validate the parameters for each configuration. By adjusting parameters listed in Table 5.5, the model predictions (solid lines) agree well with the experimental data (solid symbols), as shown in

Figure 5.4b. Therefore, we are confident that the model can produce meaningful results for the analysis.

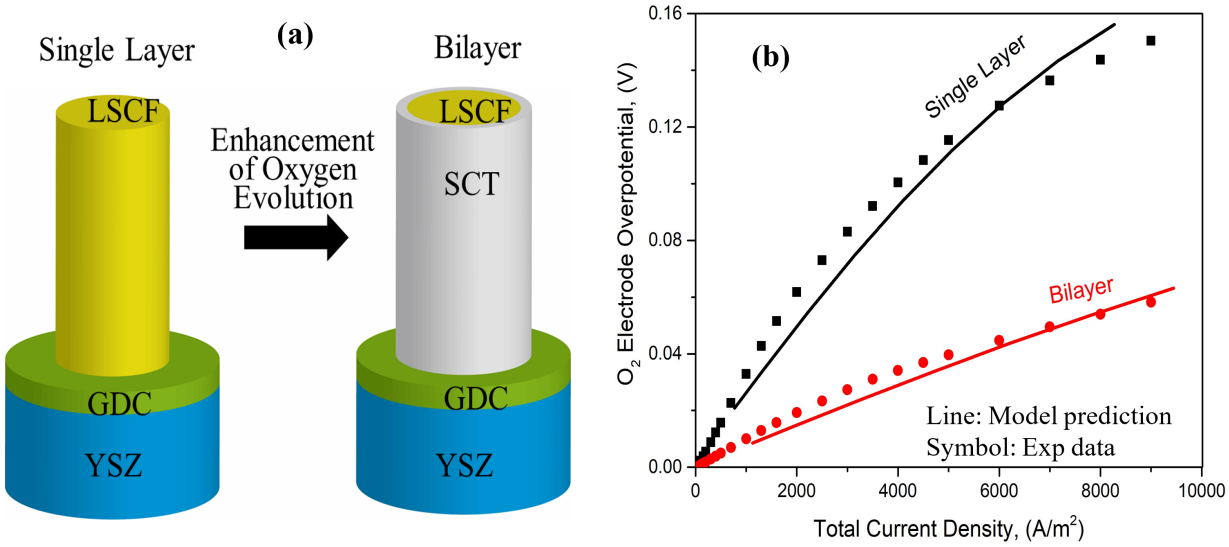

Figure 5.4: Comparison of oxygen electrode overpotential as a function of current density in both the single and bilayer configurations.

According to Mebane et al. and Kilner et al. the reactions at the air-exposed surface in those MIECs are rate limited by the oxygen evolution (oxygen incorporation under SOFC mode) step, therefore, the reaction rate constant for oxygen desorption is much higher than that of oxygen evolution, so the former reaches equilibrium(130; 132). The oxygen evolution reaction rate constant and equilibrium surface oxygen coverage obtained here is around the similar order of magnitude reported by Gong et al.(118). However, Mebane et al. reported an oxygen incorporation (evolution) rate several orders of magnitude lower than ours(130). Considering the inconsistency of parameters in the open literature, we think a direct comparison of absolute values is not meaningful. Our microscale model excluded the impact brought by the microstructure properties of the material, such as tortuosity and specific surface area. Similar limitations are shown for the exchange current density values. For the parameters obtained for single layer design and bilayer design, it is more meaningful to study its relative comparison.

5.4 Results

After experimental validation was complete, two SOEC MIEC oxygen electrode configurations (single layer LSCF and bilayer LSCF/SCT electrode) were considered. A parametric study of operating potential was conducted for both the oxygen desorption and evolution reactions. Electrolysis occurs at a potential value higher than its equilibrium(1.2 V) to overcome activation barriers and internal losses. Several key metrics were examined while comparing the reactions at the 2PBs and 3PBs. Transport pathway competition was measured primarily by calculating the ratio of current through each pathway at increasing voltages. Surface oxygen site coverage was calculated while varying the reaction rates voltage. The reaction rate was increased incrementally (0.1,1,10) versus equilibrium. The reference parameters are listed in Table 5.5, which were validated by experimental data. Variations in the lattice oxygen stoichiometry across the 2PBs and 3PBs were studied. As an indication of the overall electrochemical performance the current density was calculated over the operating voltages.

5.4.1 Transport Pathway Competition

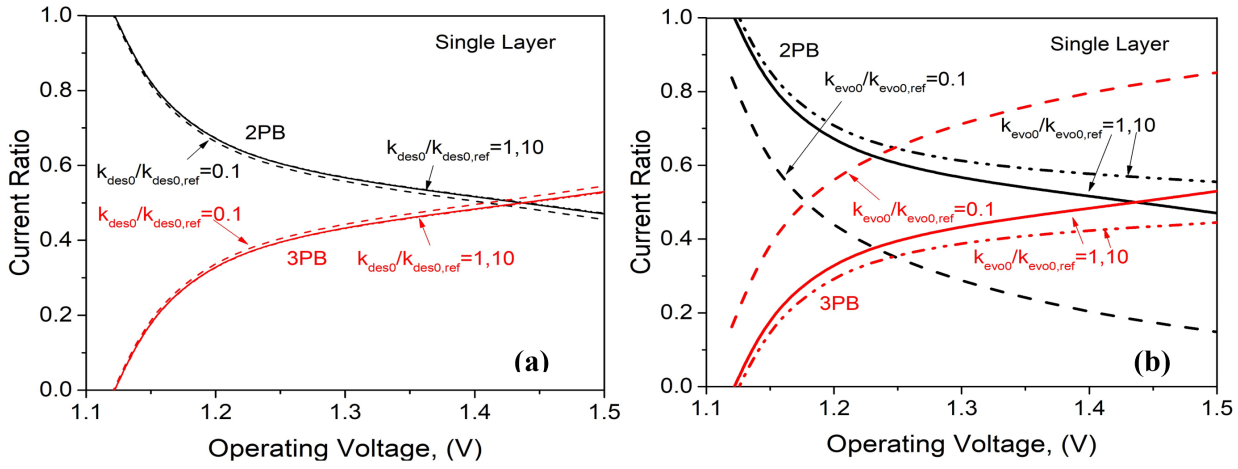

Figure 5.5: Operating voltage vs. current ratio with different oxygen desorption (a) and oxygen evolution (b) reaction kinetics for single LSCF layer configuration.

Figures 5.5 and 5.6 show the current ratio of parametric studies at various voltages. Analyses

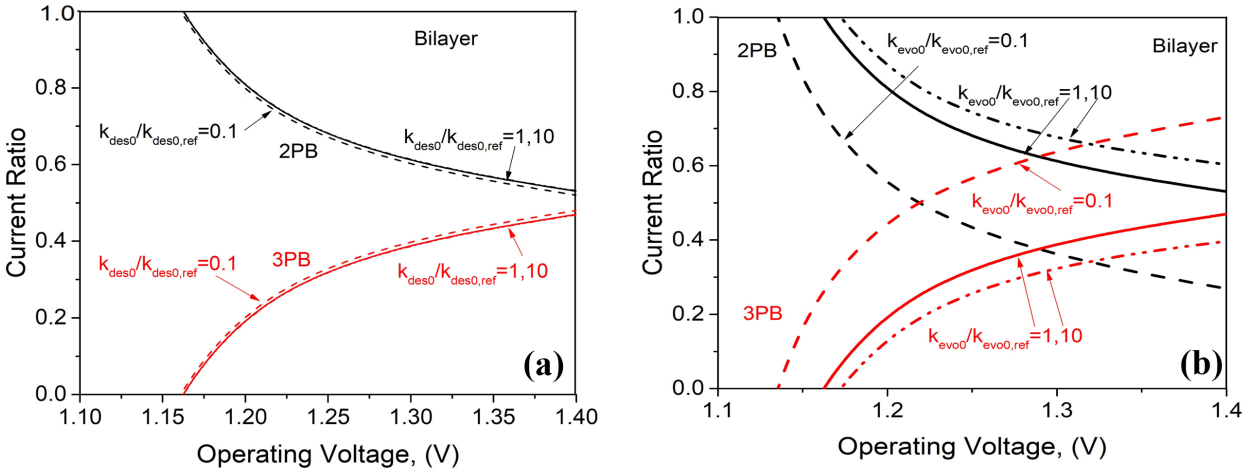

Figure 5.6: Operating voltage vs. current ratio with different oxygen desorption (a) and oxygen evolution (b) reaction kinetics for LSCF/SCT bilayer layer configuration.

were performed while varying the rate of the oxygen desorption and evolution reactions by 0.1 to 10 folds. The ratio of current through each type of boundary was studied for both the single and bilayer electrode configurations. The resulting current ratio in the single layer configuration demonstrates that the reactions at the 3PB dominate the 2PB reaction when operating at high voltages. At lower voltages, such as 1.2 V, the 2PB contributes to a higher percentage of the overall current. Varying the reaction rate constants (k_{des} and k_{evo}) had different effects on the current ratio. As shown in Figure 5.5a, the oxygen desorption reaction will not influence the current ratio heavily, but the effect brought by the evolution reaction was greater. Figure 5.5b shows that the enhanced k_{evo}, which was 10 times its equilibrium value, could potentially extend the 2PB transport pathway, which will dominate the overall current in the whole operating range.

A second layer of SCT, on the scale of a few *nm*, was added in both the numerical model and experiments. This layer is highly electronically conductive which decreases the overpotential necessary to overcome activation barriers. Since its thickness is on the scale of *nm*, which is much smaller compared to the size of the LSCF backbone, the SCT layer is assumed to only alter the electrode surface reaction properties while the bulk transport properties of the material stay unchanged. Figure 5.6 shows the results with the bilayer design. In the whole operating range, a higher ratio of current travels through the 2PB compared to its 3PB counterpart. This indicates that

with an added layer of SCT, the gas/electrode interface reaction has been greatly enhanced. Figure 5.6a and b show similar results when the reaction rate was modified. As the oxygen desorption reaction varies, the current ratio was not influenced heavily; whereas the oxygen evolution reaction rate will significantly affect the current ratio and potentially change the transport pathway.

5.4.2 Surface Oxygen Site Coverage

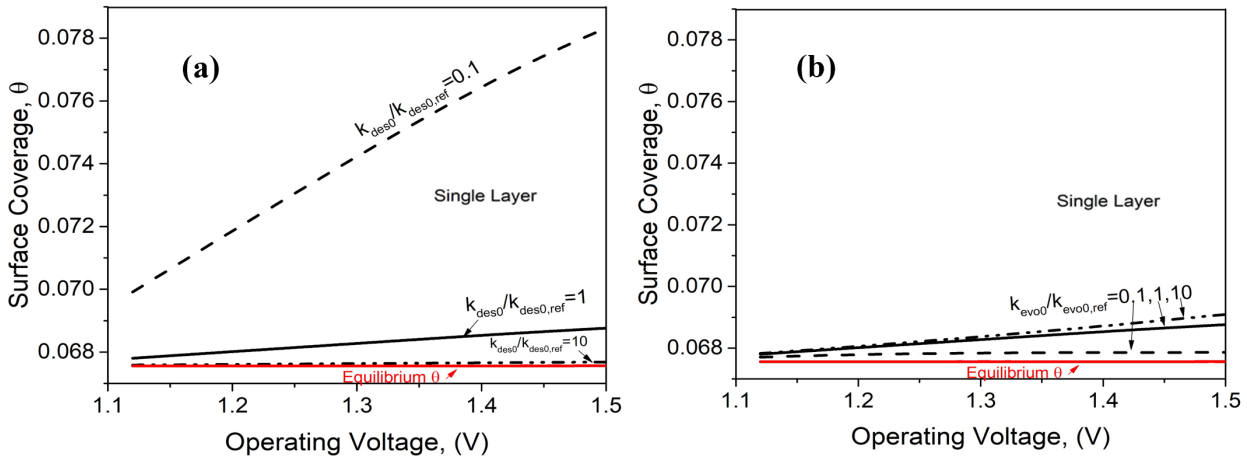

Figure 5.7: Operating voltage vs. surface coverage with different oxygen desorption (a) and oxygen evolution (b) reaction kinetics for single LSCF layer configuration.

The lattice oxygen coverage (θ) at the surface can be estimated using the Helmholtz model. Both the single and bilayer configurations, shown in Figures 5.7 and 5.8, had very similar results while increasing potential and altering the reaction rates. For the desorption reaction, a k_{des} 10 times smaller than a reference value at high potential yielded the greatest (θ). While a k_{des} equal to or greater than a reference value did not deviate θ far from equilibrium. The oxygen evolution reaction rate (k_{evo}) will not affect the surface coverage much, which is caused by the fact that oxygen desorption reaction is not the rate limiting step and it is very close to its equilibrium.

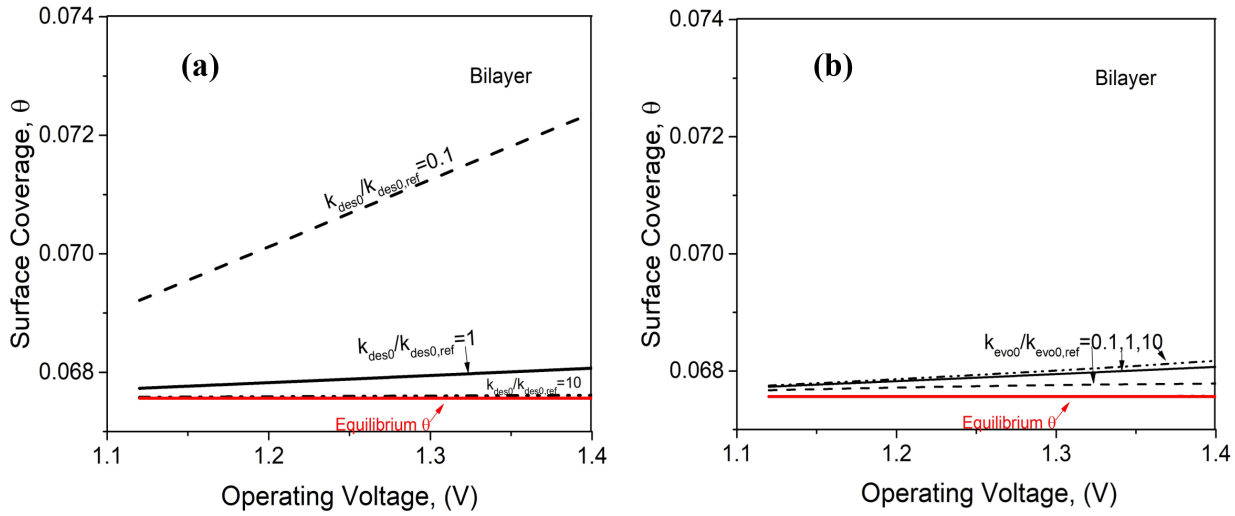

Figure 5.8: Operating voltage vs. surface coverage with different oxygen desorption (a) and oxygen evolution (b) reaction kinetics for LSCF/SCT bilayer layer configuration.

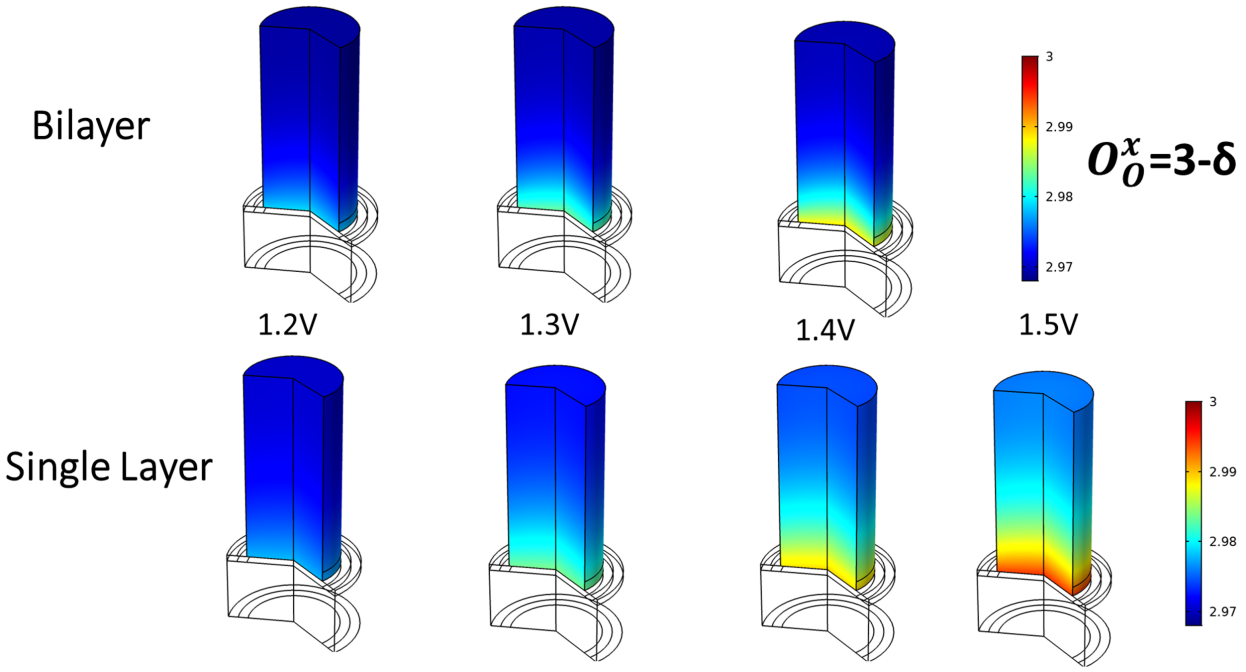

Figure 5.9: Lattice oxygen stoichiometry profile as a function voltage for both the single and bilayer configurations.

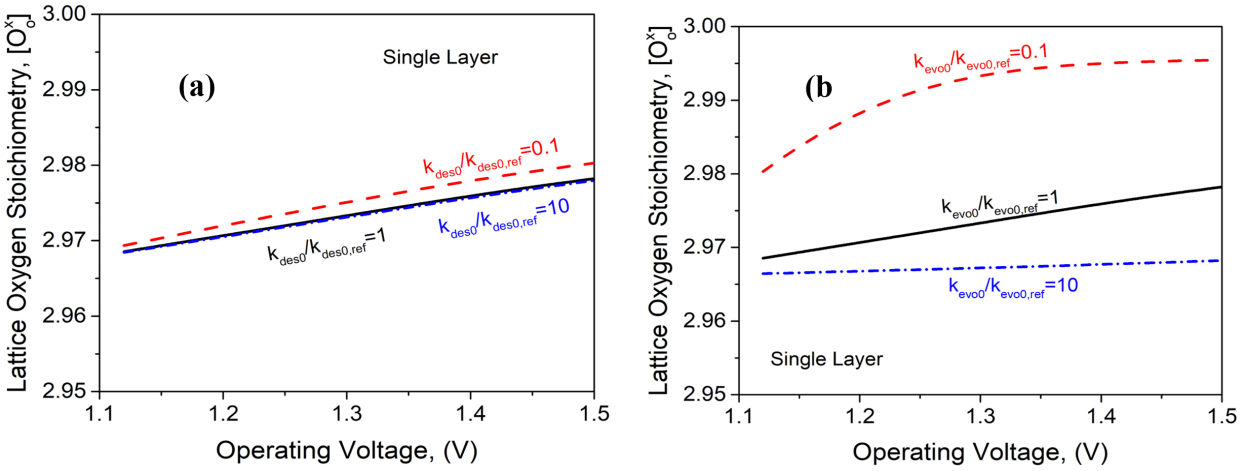

Figure 5.10: Operating voltage vs. lattice oxygen stoichiometry with different oxygen desorption (a) and oxygen evolution (b) reaction kinetics for single LSCF layer configuration.

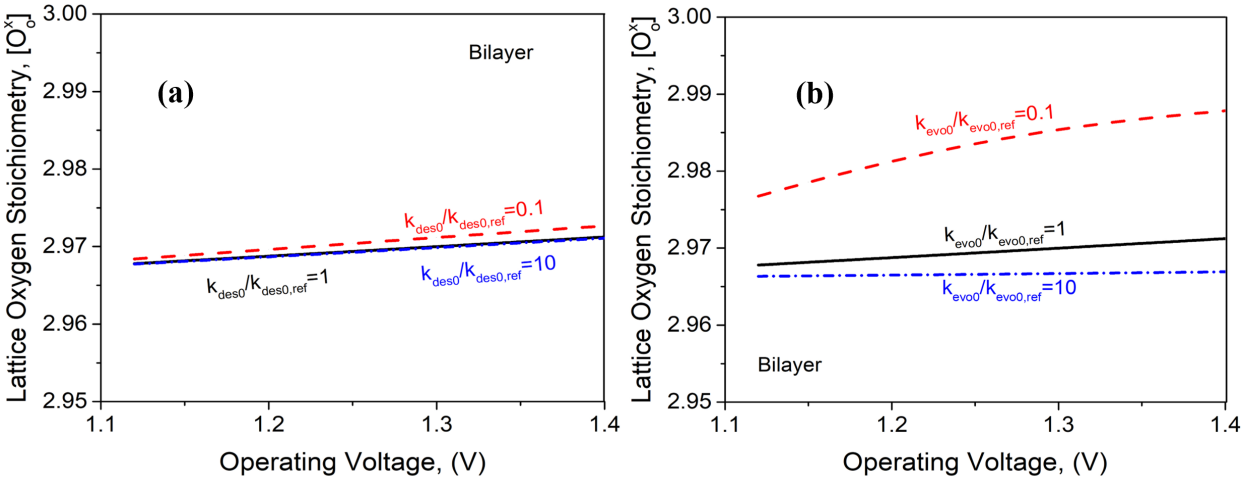

Figure 5.11: Operating voltage vs. lattice oxygen stoichiometry with different oxygen desorption (a) and oxygen evolution (b) reaction kinetics for LSCF/SCT bilayer layer configuration.

5.4.3 Lattice Oxygen Stoichiometry Profile

Using an axisymmetric modeling method, shown in Figure 5.9, the lattice oxygen stoichiometry profile was visualized while varying the operating voltage. The equilibrium is 2.97 under 1073 K and 0.21 atm for LSCF(133). Both electrode configurations are shown. The concentration deviated less from equilibrium in the bilayer under the same voltage. Under the electrolysis mode, with increasing operating voltage, more and more oxygen vacancy will be filled up by lattice oxygen,

especially at the interface as indicated by the red color. It will cause chemical expansion of the electrode, also significant degradation of transport properties of the material. We assume that the material lattice oxygen will not exceed 3 to maintain its ABO_3 crystal structure. Figures 5.10 and 5.11 show the operating voltage vs. the lattice oxygen stoichiometry at the gas/electrode interface. k_{des} and k_{evo} were varied between 0.1 and 10 folds. The desorption reaction rate has very limited impact on the lattice oxygen stoichiometry. However, lattice oxygen reaches equilibrium when the oxygen evolution reaction rate reaches a critical value and plateaus regardless of a further increase of operating voltage.

5.4.4 Overall Electrochemical Performance

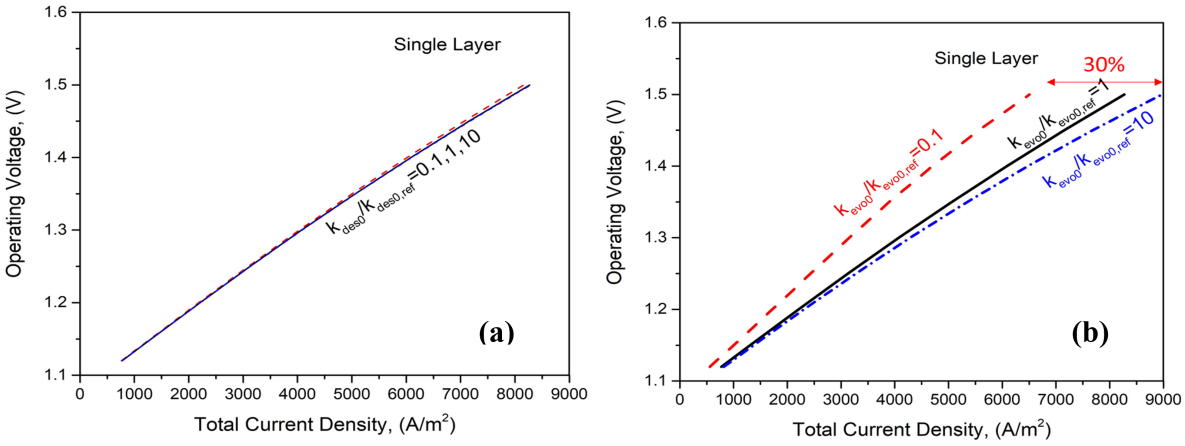

Figure 5.12: Total current density vs. operating voltage with different oxygen desorption (a) oxygen evolution (b) reaction kinetics for single LSCF layer configuration.

To gauge overall performance, total current density versus operating voltage was plotted. The results are shown in Figures 5.12 and 5.13. For both electrode configurations, the current density is hardly affected by the oxygen desorption reaction k_{des} (Figures 5.12a and 5.13a). The current density under the same voltage is higher for the bilayer. The oxygen evolution reactions effect on the current has also been studied and presented in Figures 5.12b and 5.13b. Enhancement of k_{evo} could improve the overall cell performance by elevating the current density. With single layer and bilayer configuration, 30% to 20% improvement could be achieved by varying k_{evo}.

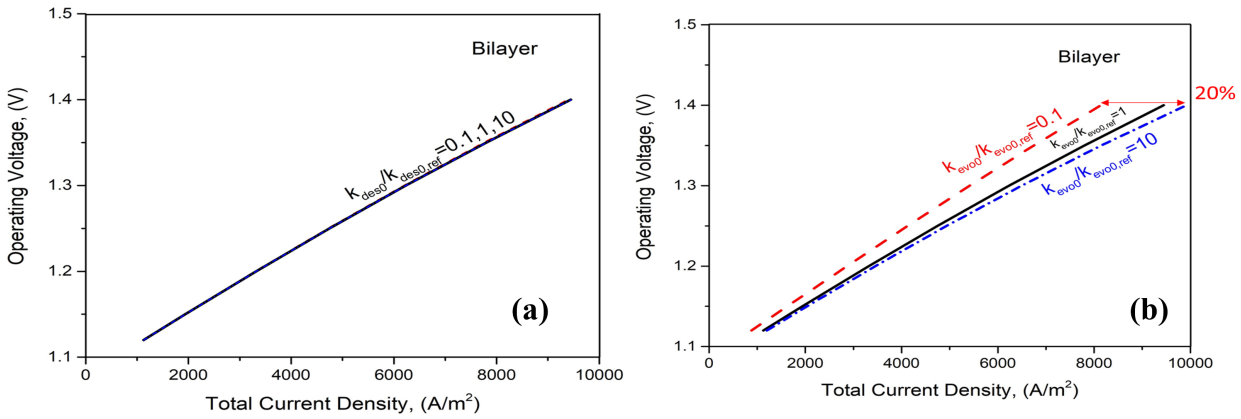

Figure 5.13: Total current density vs. operating voltage with different oxygen desorption (a) oxygen evolution (b) reaction kinetics for LSCF/SCT bilayer layer configuration.

5.5 Discussion

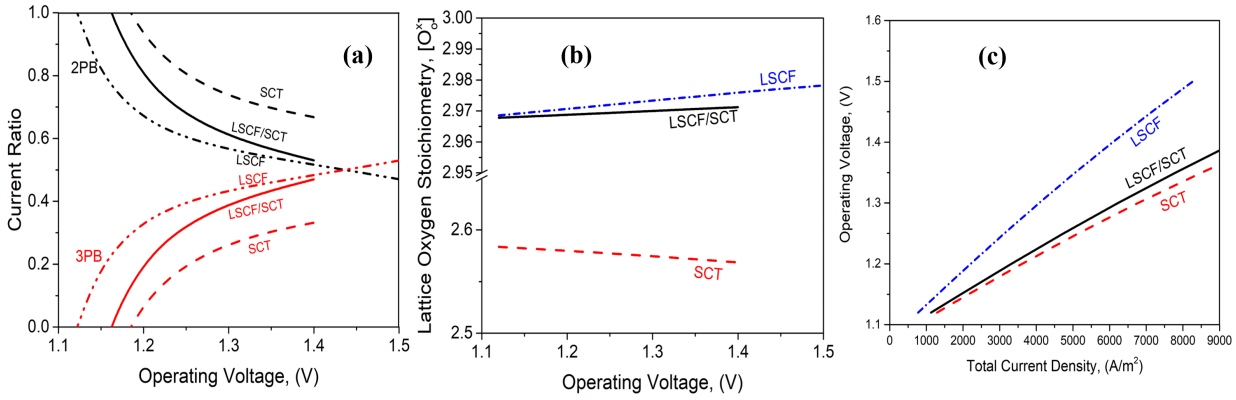

Figure 5.14: Performance comparison among single SCT layer, LSCF/SCT bilayer, and LSCF single layer configuration: (a) current ratio vs voltage (b) lattice oxygen stoichiometry vs voltage (c) voltage-current curve.

The results described in the previous text support the original hypothesis that there is competition between the 3PBs and 2PBs while the SOEC is operating at higher voltages. As a result, a nonuniform lattice oxygen stoichiometry profile forms in the MIEC electrode. It can be concluded that surface oxygen evolution plays a key role in the overall performance. There is a transition from the 2PB transport pathway to the 3PB transport pathway as operating voltage increases. A correlation between these pathways was drawn and can be associated with the delamination.

The addition of the SCT bilayer was shown to enhance the oxygen evolution reaction at the electrode/$O_{2(g)}$, 3PB, and electrode/electrolyte interfaces. Therefore, we also explored the addition of a single layer of SCT as an alternative electrode configuration. The results among all three scenarios are compared in Figure 5.14. Figure 5.14a shows that the current from the 2PBs has a higher percentage in a single SCT layer electrode when compared to the other two electrode designs; in Figure 5.14b, the lattice oxygen stoichiometry of the SCT layer is much lower than LSCF single layer or LSCF/SCT bilayer, which resulted from different extrinsic doping of SCT and LSCF; in Figure 5.14c, a higher current density has been demonstrated under the same voltage for the SCT single layer. Overall, the single SCT layer seems to be a much more promising electrode configuration in terms of improved current density and lower lattice oxygen stoichiometry, however, SCT is not as stable as LSCF and it could degrade very quickly during long-term operation according to experimental observations. In conclusion, the LSCF/SCT bilayer is a better compromise in terms of performance and durability of the cell.

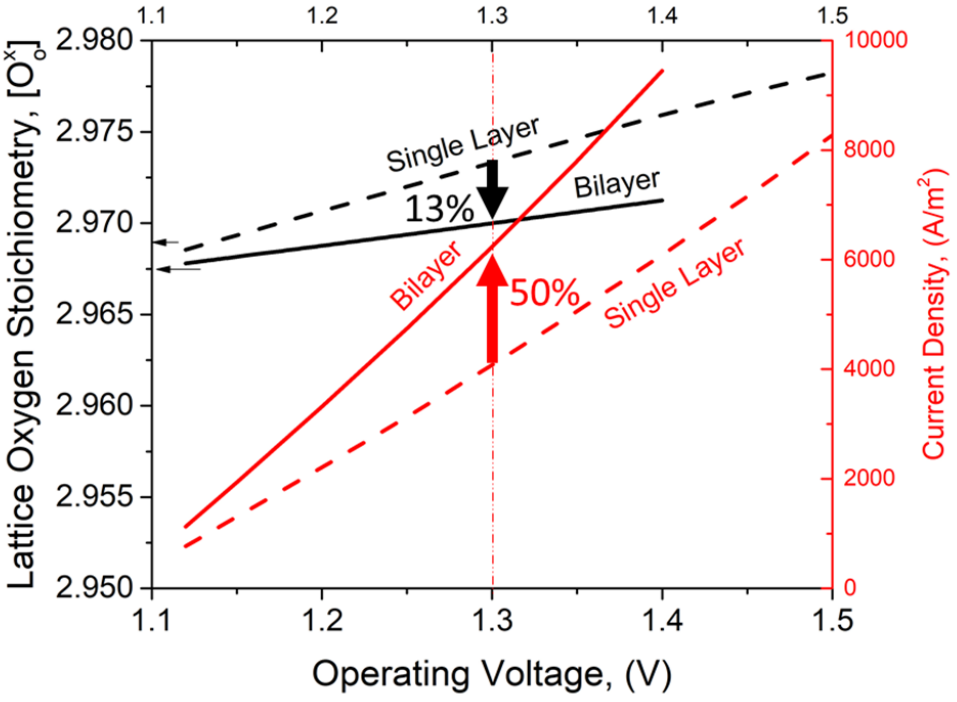

Figure 5.15: Comparison of lattice oxygen stoichiometry and current density under different operating voltage for single LSCF layer and LSCF/SCT bilayer design.

Figure 5.15 shows the comparison of operating voltages' influence on the current density and lattice oxygen stoichiometry for a conventional single LSCF layer and the newly proposed LSCF/SCT bilayer designs. For the bilayer configuration, under the thermoneutral voltage of 1.3 V, the current density has been increased by 50%; whereas lattice oxygen deviation has been reduced by 13% from equilibrium. Overall, the LSCF/SCT bilayer design could achieve greater electrochemical performance and lower the risk of delamination.

Although the results from this study are promising, there are still some limitations associated with the model. The simplified model might underestimate the microstructure effects on the 3PB and 2PB reaction sites' current ratio. Further studies may be necessary to expand the model to represent the results from experimental work more accurately. This could be done using Secondary Ion Mass Spectrometry (SIMS) to generate a detailed 3D domain. SOEC electrodes are designed to be porous, mixed conducting, multiphase materials capable of transporting gases to and from reaction sites on the solid surface. The resulting microstructure is a tortuous network with spatially varying properties for each individual phase. In many electrochemical models, this microstructure is homogenized using certain morphological parameters such as porosity, tortuosity, and specific surface area, to represent the electrode as an idealized geometry (e.g., a line, rectangle, disk, rectangular prism, or cylinder). While the homogenized approach is straightforward and can offer improved computational efficiency, it necessarily overlooks some localized, and possibly crucial, transport phenomena. For example, narrow strut-like passages may act like "choke points" and significantly limit transport, effectively shutting down entire regions of the electrode network. These thin sections also concentrate stresses and are likely to experience mechanical failure before thicker sections. Inhibited transport leads to steeper concentration gradients in these regions, thereby leading to increased chemical stresses and further compounding the local stress issue. Similarly, accurate modeling of interfacial delamination relies on the accurate consideration of the interfacial contact area; homogenized shear approaches likely underestimate the interfacial stresses in key areas.

5.6 Conclusions

To summarize, we have built a finite element microscale model to investigate the mechanism responsible for transport pathway transition and lattice oxygen stoichiometry variation of the oxygen electrode in SOECs. The key take-home messages from the study are that:

- there are two primary transport pathways within the electrode;
- the reaction at the 3PB dominates the 2PB under high operating voltage and is suspected to be the cause of delamination;
- adding a conductive layer of SCT enhances the 2PB reaction;
- to better represent the electrode structure, high-fidelity geometries can be reconstructed from 3D images obtained using advanced imaging techniques that will enable visualization the local phenomena and more accurately predict performance, limitations, and failure modes.

CHAPTER 6

CONCLUSIONS

This dissertation summarizes work toward the development of two unique forms of grid-scale energy storage technology. For the RFB, a series of studies were performed that included initial testing and experimental method development using inexpensive material and fabrication techniques, extensive static and flow charge-discharge cycling, and impedance studies. A microscale model was developed to investigate delamination of the electrode from the electrolyte in SOECs. The key questions posed in the introductory chapter are answered and recommendations for future work to continuously improve these technologies are included.

6.1 Conclusions Drawn from Flow Battery and Electrolyzer Studies

6.1.1 Redox Flow Battery

Chapters 2,3, and 4, summarized work studying RFBs and demonstrated:

- a benchtop 3D printer's ability to produce flow cells and an inexpensive test station was built;
- the monetary advantage of operating without an ion-selective membrane;
- a functional symmetric RFB using a microporous separator rather than an ion-selective membrane;
- *PDO-L-AP* as an example of a covalently linked redox couple;
- the impact that operational parameters (flow rate, charging voltage, current density, etc.) have on performance;
- that a variable flow rate can improve coulombic efficiency and charging capacity;
- the potential that EIS has as a tool to improve RFB performance by altering individual components and quantifying their impact on internal losses;

- that using a microporous separator decreases internal losses.

6.1.2 Solid Oxide Electrolyzer Cell

Chapter 5 details the development and deployment of a microscale model of a SOEC which:

- investigated the primary mechanism responsible for delamination of the electrode from the electrolyte;
- tested the hypothesis that an overabundance of lattice oxygen at the 3PBs leads to lattice structure expansion and eventually delamination;
- treated the primary reactions as a combination as chemical and electrochemical phenomena;
- developed an axisymmetric multi-physics model that was periodically validated with experimental measurements;
- confirmed the hypothesis and found that at high operating voltages the 3PB reactions dominate the 2PB reactions;
- proposed a delamination prevention method enhancing the 2PB reaction which reduced lattice oxygen and current density at 3PBs;
- investigated the use of a bilayer LSCF/SCT electrode both experimentally and computationally.

6.2 Recommendations for Future Work

6.2.1 Novel Linked Redox Couple Performance Improvement and Development of a Stack Model for Commercial Scale System

Development of covalently linked redox couples is ongoing at $MSUBI$. As discussed in this dissertation, *PDO-L-AP* (also referred to as D_2A_2) proved to be relatively unstable when cycled over for a long duration and would not be suitable for commercialization. This was expected, but

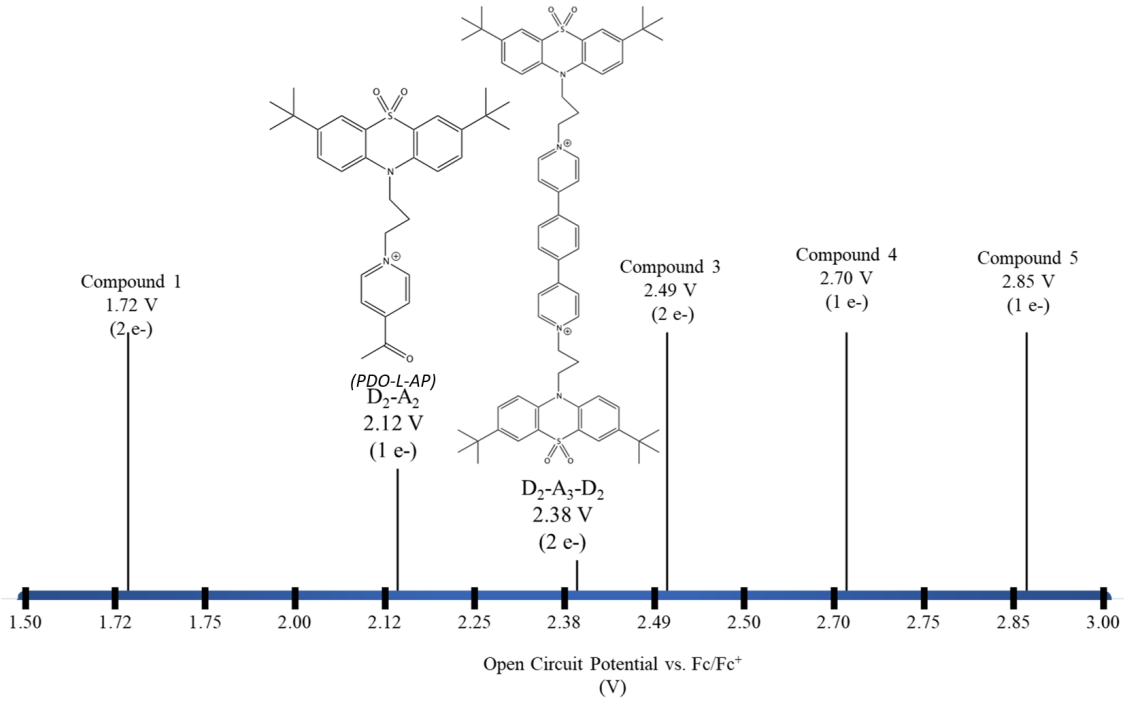

Figure 6.1: Open circuit potential of 1 e^- and 2 e^- novel redox couples developed at MSUBI.

its synthesis and cost made it an appealing candidate to perform initial studies on. New molecules are being synthesized and initial studies are being carried out. Covalently linking different e^- donating and accepting species can alter characteristics such as the open circuit potential, stability, and solubility. Several donor, acceptor, and linking species are shown in Figure 6.1. 1 e^- and 2 e^- redox couples, shown in Figure 6.2, are being investigated and considered for further study.

The logical next step is to use the procedures described to improve the stability of the novel redox couple while simultaneously preparing to scale the RFB to investigate its practicality. A high level model must be developed to guide the scaling process and to understand full cell stack operation. Barton and Brushett developed a one-dimmensional RFB stack model(45). Before scaling efforts begin, a viable linked redox couple must be synthesized and thoroughly investigated in a single cell. This can be accomplished using the analysis techniques discussed in this dissertation.

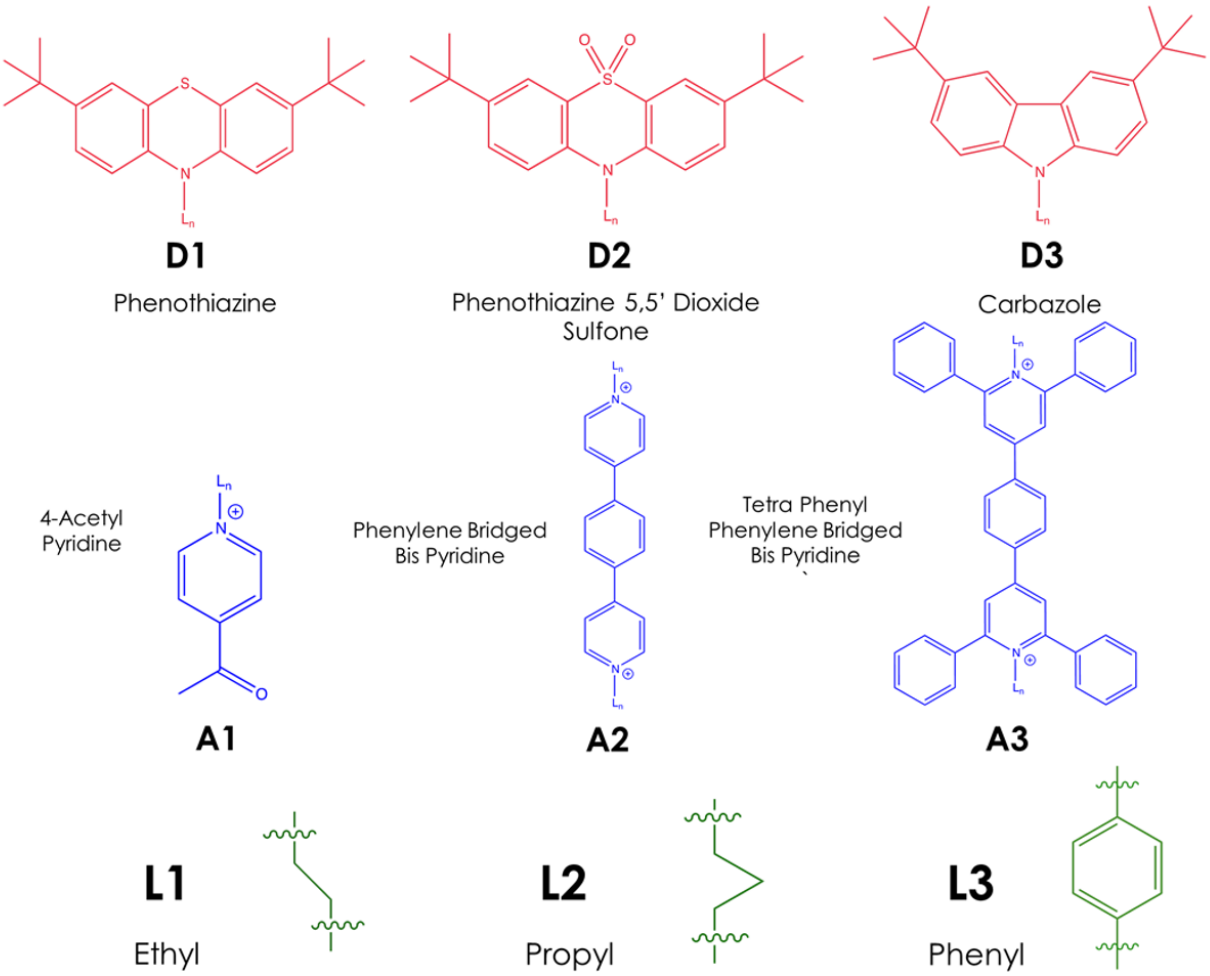

Figure 6.2: Various e^- donating, accepting, and linking species. Different combinations are under development leading to improvement in performance and practicality.

6.2.2 Incorporation of Thermomechanical Stress Analysis and the Use of Advanced Imaging Techniques to Generate Complex 3D Electrode Geometries

To improve the model's accuracy, thermal and mechanical stress components will be integrated into the existing validated model. These components coupled with electrochemical analyses will improve the model's accuracy and guide experimental work. An idealized geometry was used to represent the electrode's microstructure. Advanced imaging techniques such as SIMS can be useful for extracting a model geometry from the actual structure of the porous electrode. Figure 6.3 shows how the model's complexity can continuously be increased to study transport with greater detail,

leading to improvements in performance and durability of the SOEC. These methods will increase the complexity of the microscale model while simultaneously improving its ability to accurately represent the phenomena within an SOEC.

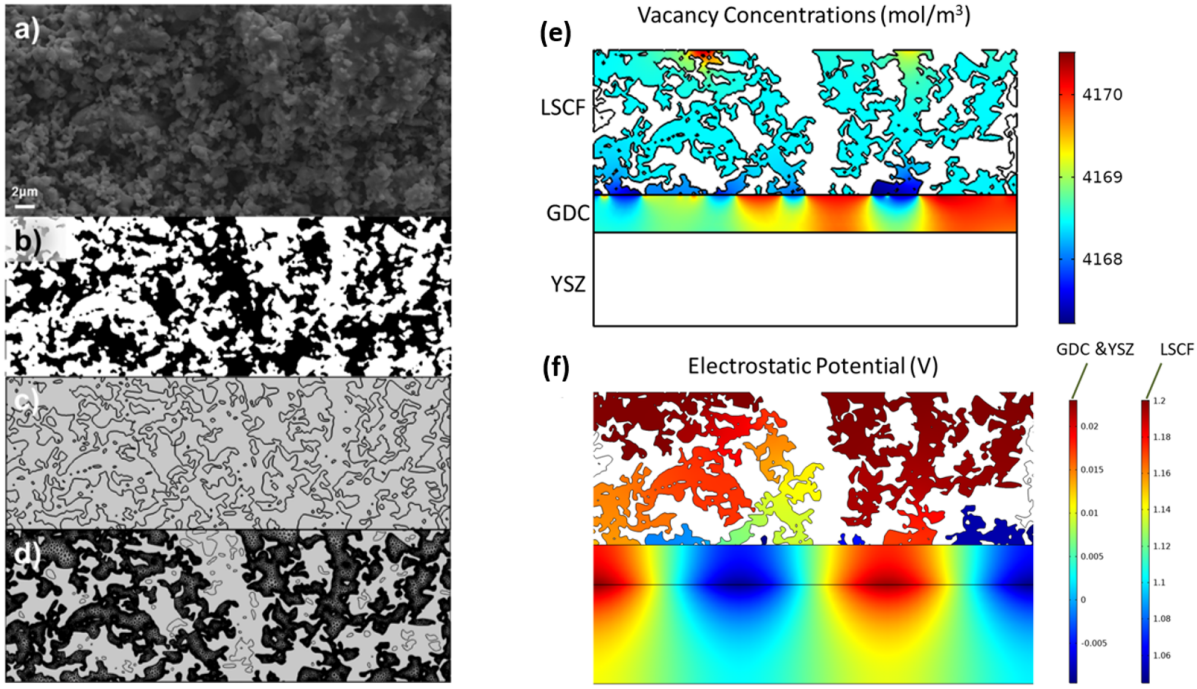

Figure 6.3: Detailed images of the microstructure of the electrode can be integrated into the model domain as complex, high fidelity geometries. This improves the accuracy of the model by gaining the ability to accurately represent the tortuous electrode structure.

APPENDIX

A.1 Initial Stability and Electrochemical Performance Studies

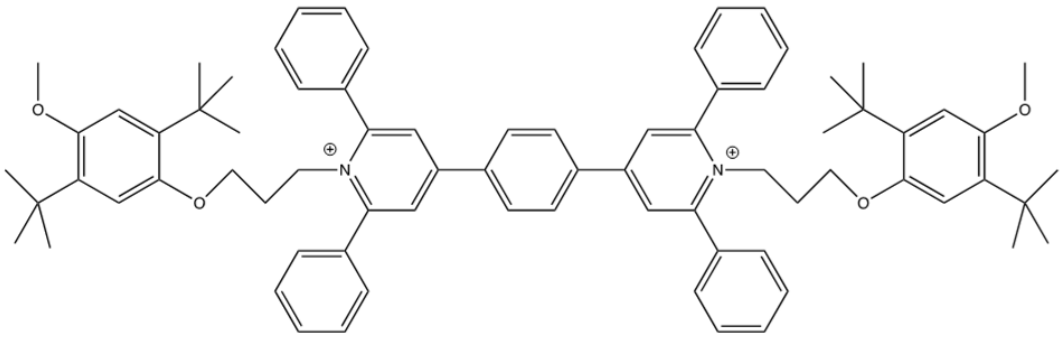

Figure A.1: Image of the molecular structure of Link-2B.

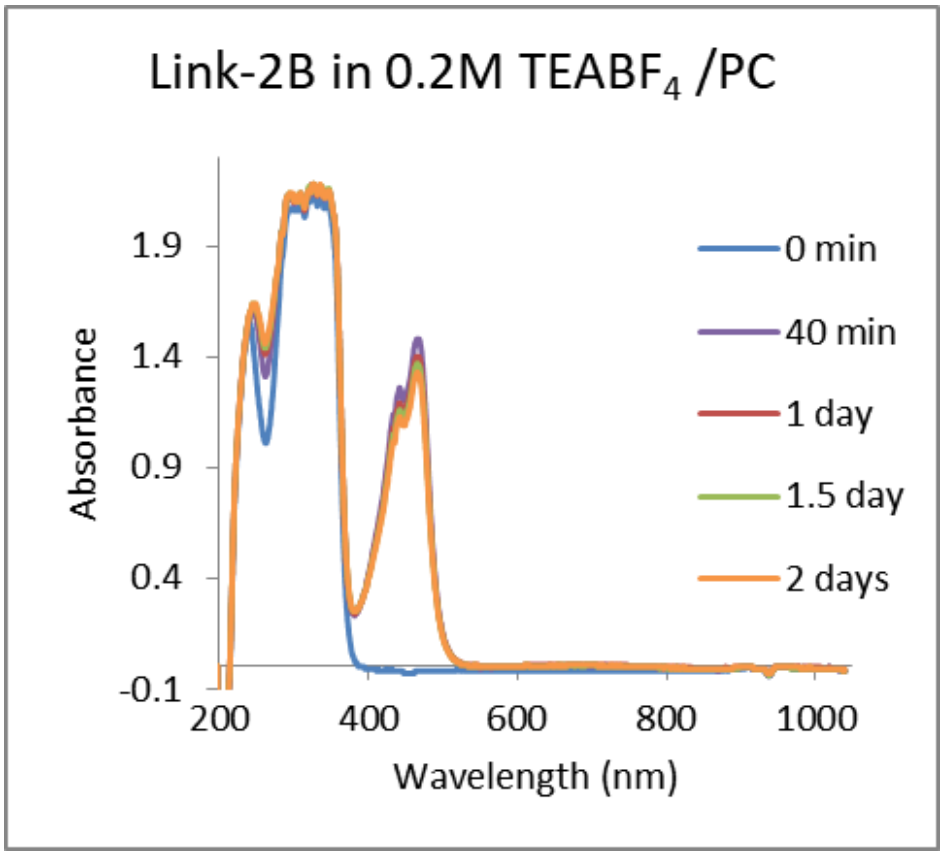

Figure A.2: Monitoring persistence of oxidized Link-2B using optical spectroscopy.

The following experiments were performed before and during the studies described in this text. The compounds were synthesized and the data was provided by researchers at *MSUBI*.

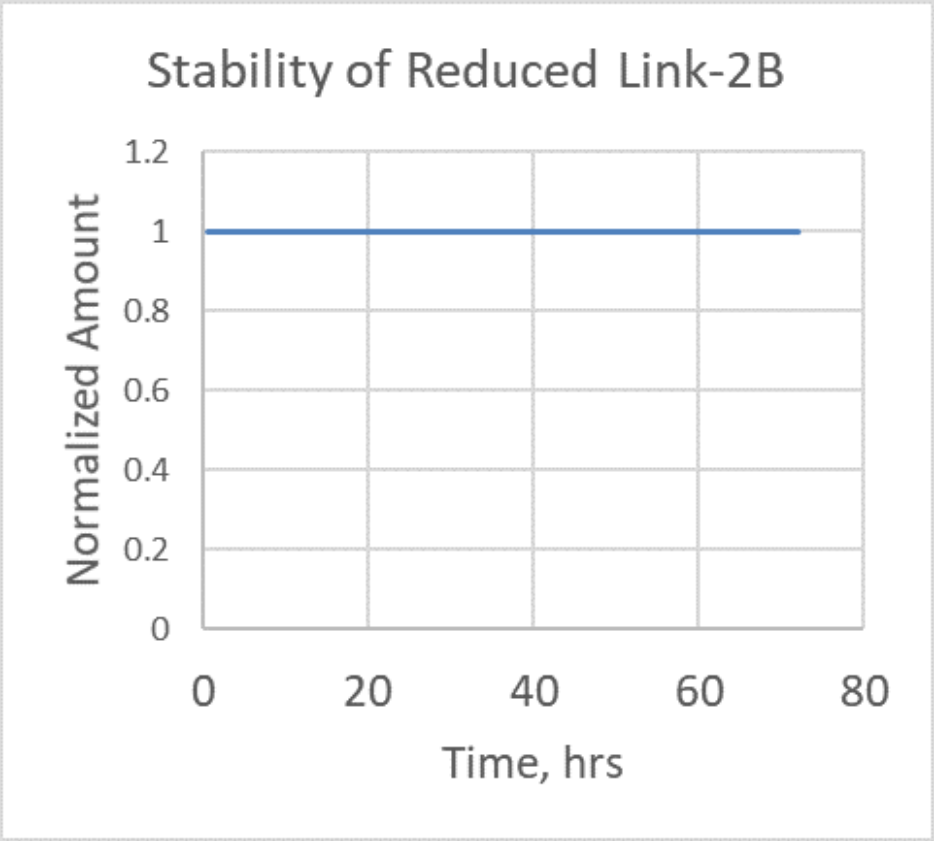

Figure A.3: The persistence of the reduced form of Link-2B as a function of time, as measured by UV-visible spectroscopy. No degradation was observed over 3 days.

The linked anolyte-catholyte materials were first screened using cyclic voltammetry, followed by repetitive bulk electrolysis. Persistence of the oxidized and reduced forms was evaluated with optical spectroscopy techniques. Although significant advances in stability were realized during the course of this project, most experiments were performed with the most available, least expensive material which was $PDO - L - AP$.

A $2e^-$ system (referred to as Link-2B) was also explored late in this project, but testing was limited to repetitive bulk electrolysis and zero-flow RFB runs due to limited material availability. Still, it was shown that Link-2B exhibited rapid electrode kinetics and excellent stability in the charged state. Spectroelectrochemical techniques were used to probe the calendar life of the charged states. In these tests, the oxidized (or reduced) form of the active material was generated at a gold honeycomb electrode in an optical cell, and the persistence of this "charged" state was

monitored by UV-Visible spectroscopy for several days. Although there is a slight degradation of the oxidized form (approximately 5%) over two days, it was sufficiently stable to allow completion of this project (as a side note, very recent concepts for new formulations promise even greater stability). The reduced form of $PDO-L-AP$ was moderately persistent (sufficiently so for this project), while those of Link-2B were quite robust, showing negligible loss of signal over 3 days shown in Figure A.2 and Figure A.3.

A.1.1 Viscosity and Solubility Studies

Viscosity and solubility measurements, along with electrochemical screening, helped to inform the choice of solvent/electrolyte. Solubility and viscosity measurements were taken of various electrolyte salts in two leading solvent candidates, acetonitrile (ACN) and propylene carbonate (PC). The solubility of the active material was then examined in the presence of the electrolyte salt with measurement summarized in Table A.1. Based on an evaluation of physical and electrochemical properties (such as liquid range, viscosity, electrochemical window, solubilities, etc.), as well as considerations of cost, toxicity, and safety (I.e., flash point), propylene carbonate was chosen as the solvent for subsequent work. The solubilities of numerous electrolyte salts were measured in PC, and tetraethylammonium tetrafluoroborate ($TEABF_4$) was chosen, primarily on the basis of its high solubility ($>$ 1M at 25 °C) and low resistivity. While the cost of $TEABF_4$ is still a concern for purposes of commercialization, that should not impact the present technical investigation and other electrolyte options will be explored separately. Additional viscosity measurements were taken using a Ubbelohde viscometer at several temperatures within the predicted operating range and are summarized in Table A.2.

Electrolyte viscosity was measured at four different temperatures in order to understand pump and fluid transfer characteristics (see Table A.2). As expected, the measured viscosity of the acetonitrile (ACN) electrolyte was much lower than that of propylene carbonate (PC) electrolyte. However, the addition of $TEABF_4$ led to significant viscosity increases in both ACN (0.436 cSt without salt at 25° C) and PC (2.11 cSt without salt at 25° C).

Table A.1: Solubility of various supporting electrolyte and active species in Acetonitrile (ACN) and Propylene Carbonate (PC). Note that immeasurable values are denoted by –.

Active Species and Supporting Electrolyte	**Concentration (M) ACN and PC**	
$TEABF_4$	1.79	1.08
$NaBF_4$	<0.1	<0.1
KBF_4	<0.1	<0.1
KPF_6	<0.1	-
$NaClO_4$	-	1
$PDO-L-AP+TEABF_4$	0.1, 1	0.1, 1
FC	-	0.08
MV	-	0.25
FC + $TEABF_4$	-	0.05, 0.5
MV + $TEABF_4$	-	0.05, 0.5
CF_3KO_3S	<0.1	-

Table A.2: Kinematic viscosity of PC/$TEABF_4$ and ACN/$TEABF_4$ electrolytes at various temperatures (entries in centistokes, cSt). Note that immeasurable values are denoted by –.

Composition	**Temperature (°C)**			
(Solvent/Supporting Species)	-25 ± 1.5	0 ± 1.5	25 ± 1.5	40 ± 1.5
PC/0.5 M $TEABF_4$	4.7	3.58	2.99	2
ACN/0.5 M $TEABF_4$	-	-	0.72	-

One key advantage of the proposed redox couple is its ability to deliver one or more electrons at the same cell voltage (depending on molecular structure). Both $1e^-$ and $2e^-$ compounds have been identified, and the most energetic chemical system to date displays a nominal cell voltage of about 2.4 V in a $2e^-$ process, but it is somewhat less robust than other systems. Solubilities greater than 2 M have also been observed, but these vary significantly with the nature of the electrolyte salt and its concentration. Final versions of the $1e^-$ and $2e^-$ candidates will likely incorporate solubilizing groups for further improvement in energy density, but the "base" materials were fully suitable for this development effort.

BIBLIOGRAPHY

BIBLIOGRAPHY

[1] "Levelized cost of energy and levelized cost of storage – 2020," *Lazard Ltd.*, 2020. https://www.lazard.com/perspective/levelized-cost-of-energy-and-levelized-cost-of-storage-2020/?nav=t.

[2] A. Z. Weber, M. M. Mench, J. P. Meyers, P. N. Ross, J. T. Gostick, and Q. Liu, "Redox flow batteries: a review," *Journal of Applied Electrochemistry*, vol. 41, no. 10, p. 1137, 2011.

[3] N. Kittner, O. Schmidt, I. Staffell, and D. M. Kammen, *Technological Learning in the Transition to a Low-Carbon Energy System*, ch. 8. Academic Press, 2020.

[4] "Net zero by 2050 – analysis," *International Energy Agency*, 2021. https://www.iea.org/reports/net-zero-by-2050.

[5] "Plan for climate change and environmental justice," *Biden Administration*, 2021. https://joebiden.com/climate-plan/.

[6] E. Larson, "Net-zero america project," *Princeton University*, 2021. https://acee.princeton.edu/rapidswitch/projects/net-zero-america-project/.

[7] T. F. Fuller and J. N. Harb, *Electrochemical Engineering*. John Wiley & Sons, 2018.

[8] K. Huang and J. B. Goodenough, *Solid Oxide Fuel Cell Technology: Principles, Performance and Operations*. Fuel Cell Technology, Elsevier, 2009.

[9] M. A. Laguna-Bercero, "Recent advances in high temperature electrolysis using solid oxide fuel cells: A review," *Journal of Power Sources*, vol. 203, pp. 4–16, 2012.

[10] S. P. Badwal, S. Giddey, and C. Munnings, "Hydrogen production via solid electrolytic routes," *Wiley Interdisciplinary Reviews: Energy and Environment*, vol. 2, pp. 473–487, 2013.

[11] X. Jin, R. E. White, and K. Huang, "Simulating charge transport in solid oxide mixed ionic and electronic conductors: Nernst-planck theory vs modified fick's law," *Journal of The Electrochemical Society*, vol. 163, pp. A2702–A2719, 2016.

[12] S. B. Adler, J. A. Lane, and B. C. H. Steele, "Electrode kinetics of porous mixed-conducting oxygen electrodes," *Journal of The Electrochemical Society*, vol. 143, p. 3554, 1996.

[13] A. V. Virkar, "Mechanism of oxygen electrode delamination in solid oxide electrolyzer cells," *Hydrogen Systems and Materials For Sustainability*, vol. 35, pp. 9527–9543, 2010.

[14] Q. Xu and T. S. Zhao, "Fundamental models for flow batteries," *Progress in Energy and Combustion Science*, vol. 49, pp. 50–58, 2015.

[15] A. Tang, J. Bao, and M. Skyllas-Kazacos, "Studies on pressure losses and flow rate optimization in vanadium redox flow battery," *Journal of Power Sources*, vol. 248, pp. 154–162, 2014.

[16] D. P. Scamman, G. W. Reade, and E. P. L. Roberts, "Numerical modelling of a bromide–polysulphide redox flow battery: Part 1: Modelling approach and validation for a pilot-scale system," *Journal of Power Sources*, vol. 189, pp. 1220–1230, 2009.

[17] P. K. Leung, C. Ponce de León, and F. C. Walsh, "An undivided zinc–cerium redox flow battery operating at room temperature (295 k)," *Electrochemistry Communications*, vol. 13, pp. 770–773, 2011.

[18] A. A. Shah, X. Li, R. G. A. Wills, and F. C. Walsh, "A mathematical model for the soluble lead-acid flow battery," *Journal of The Electrochemical Society*, vol. 157, p. A589, 2010.

[19] Q. Liu, A. A. Shinkle, Y. Li, C. W. Monroe, L. T. Thompson, and A. E. S. Sleightholme, "Non-aqueous chromium acetylacetonate electrolyte for redox flow batteries," *Electrochemistry Communications*, vol. 12, pp. 1634–1637, 2010.

[20] W. A. Braff, M. Z. Bazant, and C. R. Buie, "Membrane-less hydrogen bromine flow battery," *Nature Communications*, vol. 4, p. 2346, 2013.

[21] M. Bartolozzi, "Development of redox flow batteries. a historical bibliography," *Journal of Power Sources*, vol. 27, no. 3, pp. 219–234, 1989.

[22] S. Selverston, E. Nagelli, J. S. Wainright, and R. F. Savinell, "All-iron hybrid flow batteries with in-tank rebalancing," *Journal of The Electrochemical Society*, vol. 166, no. 10, p. A1725, 2019.

[23] C.-Y. Sun, H. Zhang, X.-D. Luo, and N. Chen, "A comparative study of nafion and sulfonated poly(ether ether ketone) membrane performance for iron-chromium redox flow battery," *Ionics*, vol. 25, no. 9, pp. 4219–4229, 2019.

[24] H. Zhang, Y. Tan, X.-D. Luo, C.-Y. Sun, and N. Chen, "Polarization effects of a rayon and polyacrylonitrile based graphite felt for iron-chromium redox flow batteries," *ChemElectroChem*, vol. 6, pp. 3175–3188, 2019.

[25] H. Zhang, N. Chen, C. Sun, and X. Luo, "Investigations on physicochemical properties and electrochemical performance of graphite felt and carbon felt for iron-chromium redox flow battery," *International Journal of Energy Research*, vol. 44, no. 5, pp. 3839–3853, 2020.

[26] N. Chen, H. Zhang, X.-D. Luo, and C.-Y. Sun, "SiO2-decorated graphite felt electrode by silicic acid etching for iron-chromium redox flow battery," *Electrochimica Acta*, vol. 336, p. 135646, 2020.

[27] A. Shrestha, K. H. Hendriks, M. S. Sigman, S. D. Minteer, and M. S. Sanford, "Realization of an asymmetric non-aqueous redox flow battery through molecular design to minimize active species crossover and decomposition," *ChemElectroChem*, vol. 26, no. 24, pp. 5369–5373, 2020.

[28] M. Li, J. Case, and S. D. Minteer, "Bipolar redox-active molecules in non-aqueous organic redox flow batteries: Status and challenges," *ChemElectroChem*, vol. 8, 2021.

[29] R. F. Gahn, N. H. Hagedorn, and J. S. Ling, "Single cell performance studies on the FE/CR Redox Energy Storage System using mixed reactant solutions at elevated temperature," in *IECEC '83; Proceedings of the Eighteenth Intersociety Energy Conversion Engineering Conference, Volume 1*, pp. 1647–1652, 1983.

[30] J. Winsberg, T. Hagemann, T. Janoschka, M. D. Hager, and U. S. Schubert, "Redox-flow batteries: From metals to organic redox-active materials," *Angewandte Chemie International Edition*, vol. 56, no. 3, pp. 686–711, 2017.

[31] B. Li and J. Liu, "Progress and directions in low-cost redox-flow batteries for large-scale energy storage," *National Science Review*, vol. 4, no. 1, pp. 91–105, 2017.

[32] T. B. Schon, B. T. McAllister, P.-F. Li, and D. S. Seferos, "The rise of organic electrode materials for energy storage," *Chemical Society Reviews*, vol. 45, no. 22, pp. 6345–6404, 2016.

[33] C. Li, L. Zhu, and T. Fleiter, "Energy efficiency potentials in the chlor-alkali sector — a case study of shandong province in china," *Energy & Environment*, vol. 25, no. 3, pp. 661–686, 2014.

[34] B. Schwenzer, J. Zhang, S. Kim, L. Li, J. Liu, and Z. Yang, "Membrane development for vanadium redox flow batteries," *ChemSusChem*, vol. 4, no. 10, pp. 1388–1406, 2011.

[35] M. Ulaganathan, V. Aravindan, Q. Yan, S. Madhavi, M. Skyllas-Kazacos, and T. M. Lim, "Recent advancements in all-vanadium redox flow batteries," *Advanced Materials Interfaces*, vol. 3, no. 1, p. 1500309, 2016.

[36] A. J. Prins, A. Dumitrascu, N. J. Mortimer, D. R. Henton, and T. F. Guarr, "High potential organic materials for battery applications," *ECS Transactions*, vol. 80, no. 10, p. 97, 2017.

[37] C. S. Sevov, R. E. M. Brooner, E. Chénard, R. S. Assary, J. S. Moore, J. Rodríguez-López, and M. S. Sanford, "Evolutionary design of low molecular weight organic anolyte materials for applications in nonaqueous redox flow batteries," *Journal of The American Chemical Society*, vol. 137, no. 45, pp. 14465–14472, 2015.

[38] X. Wei, W. Duan, J. Huang, L. Zhang, B. Li, D. Reed, W. Xu, V. Sprenkle, and W. Wang, "A high-current, stable nonaqueous organic redox flow battery," *ACS Energy Letters*, vol. 1, no. 4, pp. 705–711, 2016.

[39] R. M. Darling, K. G. Gallagher, J. A. Kowalski, S. Ha, and F. R. Brushett, "Pathways to low-cost electrochemical energy storage: a comparison of aqueous and nonaqueous flow batteries," *Energy and Environmental Science*, vol. 7, pp. 3459–3477, 2014.

[40] J. F. Wendt and J. D. Anderson, *Computational fluid dynamics: an introduction*. 3rd, Springer, 2008.

[41] T. Jyothi Latha and S. Jayanti, "Hydrodynamic analysis of flow fields for redox flow battery applications," *Journal of Applied Electrochemistry*, vol. 44, no. 9, pp. 995–1006, 2014.

[42] A. Tang, J. Bao, and M. Skyllas-Kazacos, "Studies on pressure losses and flow rate optimization in vanadium redox flow battery," *Journal of Power Sources*, vol. 248, pp. 154–162, 2014.

[43] C. S. Sevov, D. P. Hickey, M. E. Cook, S. G. Robinson, S. Barnett, S. D. Minteer, M. S. Sigman, and M. S. Sanford, "Physical organic approach to persistent, cyclable, low-potential electrolytes for flow battery applications," *J. Am. Chem. Soc.*, vol. 139, no. 8, pp. 2924–2927, 2017.

[44] W. Wang, Q. Luo, B. Li, X. Wei, L. Li, and Z. Yang, "Recent progress in redox flow battery research and development," *Advanced Functional Materials*, vol. 23, no. 8, pp. 970–986, 2013.

[45] J. L. Barton and F. R. Brushett, "A one-dimensional stack model for redox flow battery analysis and operation," *Batteries*, vol. 5, no. 1, p. 25, 2019.

[46] Y. Lei, B. W. Zhang, B. F. Bai, and T. S. Zhao, "A transient electrochemical model incorporating the donnan effect for all-vanadium redox flow batteries," *Journal of Power Sources*, vol. 299, pp. 202–211, 2015.

[47] V. P. Nemani and K. C. Smith, "Uncovering the role of flow rate in redox-active polymer flow batteries: simulation of reaction distributions with simultaneous mixing in tanks," *Electrochimica Acta*, vol. 247, pp. 475–485, 2017.

[48] V. P. Nemani and K. C. Smith, "Analysis of crossover-induced capacity fade in redox flow batteries with non-selective separators," *Journal of The Electrochemical Society*, vol. 165, no. 13, p. A3144, 2018.

[49] S. Jeong, L.-H. Kim, Y. Kwon, and S. Kim, "Effect of nafion membrane thickness on performance of vanadium redox flow battery," *Korean Journal of Chemical Engineering*, vol. 31, no. 11, pp. 2081–2087, 2014.

[50] A. S. Aricò, S. Siracusano, N. Briguglio, V. Baglio, A. Di Blasi, and V. Antonucci, "Polymer electrolyte membrane water electrolysis: status of technologies and potential applications in combination with renewable power sources," *Journal of Applied Electrochemistry*, vol. 43, no. 2, pp. 107–118, 2013.

[51] H. S. Bang, D. Kim, S. S. Hwang, and J. Won, "Surface-modified porous membranes with electrospun nafion/PVA fibres for non-aqueous redox flow battery," *Journal of Membrane Science*, vol. 514, pp. 186–194, 2016.

[52] B. Jiang, L. Yu, L. Wu, D. Mu, L. Liu, J. Xi, and X. Qiu, "Insights into the impact of the nafion membrane pretreatment process on vanadium flow battery performance," *ACS Applied Materials & Interfaces*, vol. 8, no. 19, pp. 12228–12238, 2016.

[53] N. S. Hudak, L. J. Small, H. D. Pratt, and T. M. Anderson, "Through-plane conductivities of membranes for nonaqueous redox flow batteries," *Journal of The Electrochemical Society*, vol. 162, no. 10, pp. A2188–A2194, 2015.

[54] B. Schwenzer, J. Zhang, S. Kim, L. Li, J. Liu, and Z. Yang, "Membrane development for vanadium redox flow batteries," *ChemSusChem*, vol. 4, no. 10, pp. 1388–1406, 2011.

[55] W. Xie, R. M. Darling, and M. L. Perry, "Processing and pretreatment effects on vanadium transport in nafion membranes," *Journal of The Electrochemical Society*, vol. 163, no. 1, pp. A5084–A5089, 2016.

[56] T. Janoschka, C. Friebe, M. D. Hager, N. Martin, and U. S. Schubert, "An approach toward replacing vanadium: A single organic molecule for the anode and cathode of an aqueous redox-flow battery," *ChemistryOpen*, vol. 6, no. 2, pp. 216–220, 2017.

[57] A. Petty, S. C. Mann, A. Dumitrascu, K. Olson, and T. F. Guarr, "Multifunctional pyridinium systems for nonaqueous redox flow batteries," *ECS Transactions*, vol. 80, no. 10, pp. 1241–1255, 2017.

[58] K. R. Cook, E. Lau, J. Thayer, S. Mann, T. Guarr, and A. Benard, "Development of a Membraneless Organic Redox Flow Battery," *ASME International Mechanical Engineering Congress and Exposition*, vol. 6A: Energy, 2018. 10.1115/IMECE2018-88024.

[59] K. H. Hendriks, C. S. Sevov, M. E. Cook, and M. S. Sanford, "Multielectron cycling of a low-potential anolyte in alkali metal electrolytes for nonaqueous redox flow batteries," *ACS Energy Letters*, vol. 2, no. 10, pp. 2430–2435, 2017.

[60] J. D. Milshtein, R. M. Darling, J. Drake, M. L. Perry, and F. R. Brushett, "The critical role of supporting electrolyte selection on flow battery cost," *Journal of The Electrochemical Society*, vol. 164, no. 14, pp. A3883–A3895, 2017.

[61] J. A. Kowalski, L. Su, J. D. Milshtein, and F. R. Brushett, "Recent advances in molecular engineering of redox active organic molecules for nonaqueous flow batteries," *Current Opinion in Chemical Engineering*, vol. 13, pp. 45–52, 2016.

[62] N. H. Attanayake, J. A. Kowalski, K. V. Greco, M. D. Casselman, J. D. Milshtein, S. J. Chapman, S. R. Parkin, F. R. Brushett, and S. A. Odom, "Tailoring two-electron-donating phenothiazines to enable high-concentration redox electrolytes for use in nonaqueous redox flow batteries," *Chemistry of Materials*, vol. 31, no. 12, pp. 4353–4363, 2019.

[63] F. R. Brushett, J. T. Vaughey, and A. N. Jansen, "An all-organic non-aqueous lithium-ion redox flow battery," *Advanced Energy Materials*, vol. 2, no. 11, pp. 1390–1396, 2012.

[64] J. D. Milshtein, A. P. Kaur, M. D. Casselman, J. A. Kowalski, S. Modekrutti, P. L. Zhang, N. H. Attanayake, C. F. Elliott, S. R. Parkin, C. Risko, F. R. Brushett, and S. A. Odom, "High current density, long duration cycling of soluble organic active species for non-aqueous redox flow batteries," *Energy & Environmental Science*, vol. 9, no. 11, pp. 3531–3543, 2016.

[65] J. Huang, B. Pan, W. Duan, X. Wei, R. S. Assary, L. Su, F. R. Brushett, L. Cheng, C. Liao, M. S. Ferrandon, W. Wang, Z. Zhang, A. K. Burrell, L. A. Curtiss, I. A. Shkrob, J. S. Moore, and L. Zhang, "The lightest organic radical cation for charge storage in redox flow batteries," *Scientific Reports*, vol. 6, no. 1, p. 32102, 2016.

[66] J.-Y. Chen, C.-L. Hsieh, N.-Y. Hsu, Y.-S. Chou, and Y.-S. Chen, "Determining the limiting current density of vanadium redox flow batteries," *Energies*, vol. 7, no. 9, pp. 5863–5873, 2014.

[67] L. F. Arenas, C. P. d. León, and F. C. Walsh, "Engineering aspects of the design, construction and performance of modular redox flow batteries for energy storage," *Journal of Energy Storage*, vol. 11, pp. 119–153, 2017.

[68] M. O. Bamgbopa, S. Almheiri, and H. Sun, "Prospects of recently developed membraneless cell designs for redox flow batteries," *Renewable and Sustainable Energy Reviews*, vol. 70, pp. 506–518, 2017.

[69] PlugVolt, "EIS measurements for energy storage - what, how and why?," 2019. https://www.borneosoft.com/form/bTh95T/0/eis-measurements-for-energy-storage-what-how-and-why.

[70] X. Wu, K. Song, X. Zhang, N. Hu, L. Li, W. Li, L. Zhang, and H. Zhang, "Safety issues in lithium ion batteries: Materials and cell design," *Frontiers in Energy Research*, vol. 7, 2019.

[71] X. Yuan, H. Liu, and J. Zhang, *Lithium-Ion Batteries: Advanced Materials and Technologies*. CRC Press, 2011.

[72] M. Wang, A. V. Le, D. J. Noelle, Y. Shi, Y. S. Meng, and Y. Qiao, "Internal-short-mitigating current collector for lithium-ion battery," *Journal of Power Sources*, vol. 349, pp. 84–93, 2017.

[73] C. Yin, S. Guo, H. Fang, J. Liu, Y. Li, and H. Tang, "Numerical and experimental studies of stack shunt current for vanadium redox flow battery," *Applied Energy*, vol. 151, pp. 237–248, 2015.

[74] K. Lin, R. Gómez-Bombarelli, E. S. Beh, L. Tong, Q. Chen, A. Valle, A. Aspuru-Guzik, M. J. Aziz, and R. G. Gordon, "A redox-flow battery with an alloxazine-based organic electrolyte," *Nature Energy*, vol. 1, no. 9, pp. 1–8, 2016.

[75] J.-D. Jeon, H. S. Yang, J. Shim, H. S. Kim, and J. H. Yang, "Dual function of quaternary ammonium in zn/br redox flow battery: Capturing the bromine and lowering the charge transfer resistance," *Electrochimica Acta*, vol. 127, pp. 397–402, 2014.

[76] M. Pugach, M. Kondratenko, S. Briola, and A. Bischi, "Numerical and experimental study of the flow-by cell for vanadium redox batteries," *Energy Procedia*, vol. 142, pp. 3667–3674, 2017.

[77] M. Dassisti, G. Cozzolino, M. Chimienti, A. Rizzuti, P. Mastrorilli, and P. L'Abbate, "Sustainability of vanadium redox-flow batteries: Benchmarking electrolyte synthesis procedures," *International Journal of Hydrogen Energy*, vol. 41, no. 37, pp. 16477–16488, 2016.

[78] D. Manschke, T. Seipp, S. Berthold, and K. A. Friedrich, "Verification of redox flow batteries' functionality by electrochemical impedance spectroscopy tests," *Batteries*, vol. 4, no. 4, p. 58, 2018.

[79] B. A. Braz, C. S. Moreira, V. B. Oliveira, and A. M. F. R. Pinto, "Effect of the current collector design on the performance of a passive direct methanol fuel cell," *Electrochimica Acta*, vol. 300, pp. 306–315, 2019.

[80] P. Mazur, J. Mrlik, J. Charvat, J. Pocedic, J. Vrana, J. Dundalek, and J. Kosek, "A complex four-point method for the evaluation of ohmic and faradaic losses within a redox flow battery single-cell," *MethodsX*, vol. 6, pp. 534–539, 2019.

[81] W. Wang, J. P. Kizewski, W. Duan, J. P. Kizewski, and W. Duan, *Introduction to Redox Flow Batteries*. 1st, Taylor & Francis Group, 2017.

[82] V. V. Sentyurin, O. A. Levitskiy, and T. V. Magdesieva, "Molecular design of ambipolar redox-active molecules II: Closed-shell systems," *Current Opinion in Electrochemistry*, 2020.

[83] L. Zhang, S. Dong, and L. Zhu, "Fluorescent dyes of the esculetin and alizarin families respond to zinc ions ratiometrically," *Chemical Communications*, vol. 1, no. 19, pp. 1891–1893, 2007.

[84] J. D. Milshtein, K. M. Tenny, J. L. Barton, J. Drake, R. M. Darling, and F. R. Brushett, "Quantifying mass transfer rates in redox flow batteries," *Journal of The Electrochemical Society*, vol. 164, no. 11, pp. E3265–E3275, 2017.

[85] M. A. Miller, J. S. Wainright, and R. F. Savinell, "Iron ionic liquid electrolytes for redox flow battery applications," *Journal of The Electrochemical Society*, vol. 163, no. 3, pp. A578–A579, 2016.

[86] A. A. Shinkle, T. J. Pomaville, A. E. S. Sleightholme, L. T. Thompson, and C. W. Monroe, "Solvents and supporting electrolytes for vanadium acetylacetonate flow batteries," *Journal of Power Sources*, vol. 248, pp. 1299–1305, 2014.

[87] R. Malik, "Flow battery solvents: Looking deeper," *Joule*, vol. 1, no. 3, pp. 425–427, 2017.

[88] T. L. S. Konig, M.R. Suriyah, "Innovative model-based flow rate optimization for vanadium redox flow batteries," *Journal of Power Sources*, vol. 333, pp. 134–144, 2016.

[89] K. Yaji, S. Yamasaki, S. Tsushima, T. Suzuki, and K. Fujita, "Topology optimization for the design of flow fields in a redox flow battery," *Structural and Multidisciplinary Optimization*, vol. 57, no. 2, pp. 535–546, 2018.

[90] A. M. Pezeshki, R. L. Sacci, F. M. Delnick, D. S. Aaron, and M. M. Mench, "Elucidating effects of cell architecture, electrode material, and solution composition on overpotentials in redox flow batteries," *Electrochimica Acta*, vol. 229, pp. 261–270, 2017.

[91] K. M. Lisboa, J. Marschewski, N. Ebejer, P. Ruch, R. M. Cotta, B. Michel, and D. Poulikakos, "Mass transport enhancement in redox flow batteries with corrugated fluidic networks," *Journal of Power Sources*, vol. 359, pp. 322–331, 2017.

[92] K. Ward and Z. H. Fan, "Mixing in microfluidic devices and enhancement methods," *Journal of Micromechanics and Microengineering*, vol. 25, no. 9, p. 094001, 2015.

[93] S. Brunauer, P. H. Emmett, and E. Teller, "Adsorption of gases in multimolecular layers," *Journal of the American Chemical Society*, vol. 60, no. 2, pp. 309–319, 1938.

[94] L. Xing, X. Zheng, M. Schroeder, J. Alvarado, A. von Wald Cresce, K. Xu, Q. Li, and W. Li, "Deciphering the ethylene carbonate–propylene carbonate mystery in li-ion batteries," *Accounts of Chemical Research*, vol. 51, no. 2, pp. 282–289, 2018.

[95] M. Skyllas-Kazacos, M. H. Chakrabarti, S. A. Hajimolana, F. S. Mjalli, and M. Saleem, "Progress in flow battery research and development," *Journal of The Electrochemical Society*, vol. 158, no. 8, pp. R55–R79, 2011.

[96] M. Skyllas-Kazacos, "Novel vanadium chloride/polyhalide redox flow battery," *Journal of Power Sources*, vol. 124, no. 1, pp. 299–302, 2003.

[97] J. A. Trainham and J. Newman, "A comparison between flow-through and flow-by porous electrodes for redox energy storage," *Electrochimica Acta*, vol. 26, no. 4, pp. 455–469, 1981.

[98] T. Tomov and I. Tsoneva, "Are the stainless steel electrodes inert?," *Bioelectrochemistry*, vol. 51, no. 2, pp. 207–209, 2000.

[99] P. Arora and Z. J. Zhang, "Battery separators," *Chemical Reviews*, vol. 104, no. 10, pp. 4419–4462, 2004.

[100] X. L. Zhou, T. S. Zhao, L. An, Y. K. Zeng, and L. Wei, "Critical transport issues for improving the performance of aqueous redox flow batteries," *Journal of Power Sources*, vol. 339, pp. 1–12, 2017.

[101] M. Zhou, Q. Huang, T. N. Pham Truong, J. Ghilane, Y. G. Zhu, C. Jia, R. Yan, L. Fan, H. Randriamahazaka, and Q. Wang, "Nernstian-potential-driven redox-targeting reactions of battery materials," *Chem*, vol. 3, no. 6, pp. 1036–1049, 2017.

[102] I. L. Escalante-García, J. S. Wainright, L. T. Thompson, and R. F. Savinell, "Performance of a non-aqueous vanadium acetylacetonate prototype redox flow battery: Examination of separators and capacity decay," *Journal of The Electrochemical Society*, vol. 162, no. 3, p. A363, 2014.

[103] "Quality of your fit in electrochemical impedance spectroscopy," *Gamry Instruments*, 2020. https://www.gamry.com/application-notes/EIS/fit-in-eis/.

[104] "EIS - potentiostatic or galvanostatic mode," *Gamry Instruments*, 2019. https://www.gamry.com/application-notes/EIS/eis-potentiostatic-galvanostatic-mode/.

[105] "Basics of EIS: Electrochemical research-impedance," *Gamry Instruments*, 2019. https://www.gamry.com/application-notes/EIS/basics-of-electrochemical-impedance-spectroscopy/.

[106] M. E. Orazem and B. Tribollet, *Equivalent Circuit Analogs*, ch. 9, pp. 153–162. John Wiley Sons, Ltd, 2008.

[107] A. Mayyas, M. Wei, and G. Levis, "Hydrogen as a long-term, large-scale energy storage solution when coupled with renewable energy sources or grids with dynamic electricity pricing schemes," *International Journal of Hydrogen Energy*, vol. 45, no. 33, pp. 16311–16325, 2020.

[108] K. O'Malley, G. Ordaz, J. Adams, K. Randolph, C. C. Ahn, and N. T. Stetson, "Applied hydrogen storage research and development: A perspective from the u.s. department of energy," *Journal of Alloys and Compounds*, vol. 645, pp. S419–S422, 2015.

[109] P. P. Edwards, V. L. Kuznetsov, W. I. F. David, and N. P. Brandon, "Hydrogen and fuel cells: Towards a sustainable energy future," *Energy Policy*, vol. 36, no. 12, pp. 4356–4362, 2008.

[110] S. Satyapal, J. Petrovic, C. Read, G. Thomas, and G. Ordaz, "The u.s. department of energy's national hydrogen storage project: Progress towards meeting hydrogen-powered vehicle requirements," *Catalysis Today*, vol. 120, no. 3, pp. 246–256, 2007.

[111] N. L. Garland, D. C. Papageorgopoulos, and J. M. Stanford, "Hydrogen and fuel cell technology: Progress, challenges, and future directions," *Energy Procedia*, vol. 28, pp. 2–11, 2012.

[112] P. C. F. Schœnbein, "On the voltaic polarization of certain solid and fluid substances," *The London, Edinburgh, and Dublin Philosophical Magazine and Journal of Science*, vol. 14, no. 85, pp. 43–45, 1839.

[113] W. R. Grove, "On the gas voltaic battery. voltaic action of phosphorus, sulphur and hydrocarbons," *Philosophical Transactions of the Royal Society of London*, vol. 135, pp. 351–361, 1845.

[114] Q. Zhang, B.-K. Park, S. A. Barnett, and P. W. Voorhees, "Distribution of oxygen partial pressure in multilayer electrolytes: Explaining degradation of solid oxide electrolyzer cells," *ECS Meeting Abstracts*, vol. MA2019-02, no. 40, p. 1886, 2019.

[115] W. Ostwald, "Die wissenschaftliche elektrochemie der gegenwart und die technische der zukunft," *Zeitschrift für Physikalische Chemie*, vol. 15U, no. 1, pp. 409–421, 1894.

[116] W. Dönitz and R. Streicher, "Hochtemperatur-elektrolyse von wasserdampf – entwicklungsstand einer neuen technologie zur wasserstoff-erzeugung," *Chemie Ingenieur Technik*, vol. 52, no. 5, pp. 436–438, 1980.

[117] Y. Lu, C. Kreller, and S. B. Adler, "Measurement and modeling of the impedance characteristics of porous la1 x sr x CoO3 electrodes," *Journal of The Electrochemical Society*, vol. 156, no. 4, p. B513, 2009.

[118] M. Gong, R. S. Gemmen, and X. Liu, "Modeling of oxygen reduction mechanism for 3pb and 2pb pathways at solid oxide fuel cell cathode from multi-step charge transfer," *Journal of Power Sources*, vol. 201, pp. 204–218, 2012.

[119] Y. Li, R. Gemmen, and X. Liu, "Oxygen reduction and transportation mechanisms in solid oxide fuel cell cathodes," *Journal of Power Sources*, vol. 195, no. 11, pp. 3345 – 3358, 2010.

[120] S. Liu, J. Suo, and J. Xiao, "Effects of surface overpotential at the lanthanum strontium cobalt ferrite yttria stabilized zirconia interface in a model solid oxide fuel cell cathode," *International Journal of Hydrogen Energy*, vol. 33, no. 21, pp. 6322–6326, 2008.

[121] T.-J. Huang and C.-L. Chou, "Oxygen dissociation and interfacial transfer rate on performance of SOFCs with metal-added (LaSr)(CoFe)o3-(ce,gd)o2 – cathodes," *Fuel Cells*, vol. 10, no. 4, pp. 718–725, 2010.

[122] M. B. Mogensen, E. Ivers-Tiffée, T. Kawada, and S. Adler, *Solid-Gas Electrochemical Interfaces – SGEI 1*. The Electrochemical Society, 2015.

[123] F. H. v. Heuveln and H. J. M. Bouwmeester, "Electrode properties of sr-doped LaMnO3 on yttria-stabilized zirconia: II. electrode kinetics," *Journal of The Electrochemical Society*, vol. 144, no. 1, p. 134, 1997.

[124] X. J. Chen, K. A. Khor, and S. H. Chan, "Identification of o_2 reduction processes at yttria stabilized zirconia|doped lanthanum manganite interface," *Journal of Power Sources*, vol. 123, no. 1, pp. 17–25, 2003.

[125] J.-D. Kim, G.-D. Kim, J.-W. Moon, Y.-i. Park, H.-W. Lee, K. Kobayashi, M. Nagai, and C.-E. Kim, "Corrigendum to "characterization of lsm-ysz composite electrode by ac impedance spectroscopy" [1) 379-389]," *Solid State Ionics*, vol. 144, no. 3-4, pp. 379–389, 2001.

[126] A. Hammou and S. Georges, *Solid-State Electrochemistry*. Essential Course Notes and Solved Exercises, Springer, 2020.

[127] H. Helmholtz, "Studien über electrische grenzschichten," *Annalen der Physik*, vol. 243, no. 7, pp. 337–382, 1879.

[128] X. Jin, "Modeling of chemical-mechanical couplings in solid oxide cells and reliability analysis," *University of South Carolina Archives*, 2014.

[129] A. M. Svensson, S. Sunde, and K. Nisşancioğlu, "Mathematical modeling of oxygen exchange and transport in air-perovskite-YSZ interface regions: I. reduction of intermediately adsorbed oxygen," *Journal of The Electrochemical Society*, vol. 144, no. 8, p. 2719, 1997.

[130] D. S. Mebane, Y. Liu, and M. Liu, "A two-dimensional model and numerical treatment for mixed conducting thin films: The effect of sheet resistance," *Journal of The Electrochemical Society*, vol. 154, no. 5, p. A421, 2007.

[131] D. S. Mebane and M. Liu, "Classical, phenomenological analysis of the kinetics of reactions at the gas-exposed surface of mixed ionic electronic conductors," *Journal of Solid State Electrochemistry*, vol. 10, no. 8, pp. 575–580, 2006.

[132] J. A. Kilner, R. A. De Souza, and I. C. Fullarton, "Surface exchange of oxygen in mixed conducting perovskite oxides," *Solid State Ionics*, vol. 86-88, pp. 703–709, 1996.

[133] S. Hashimoto, Y. Fukuda, M. Kuhn, K. Sato, K. Yashiro, and J. Mizusaki, "Oxygen nonstoichiometry and thermo-chemical stability of lanthanum strontium cobalt ferrite (lscf)," *Solid State Ionics*, vol. 181, no. 37, pp. 1713–1719, 2010.